



UNIVERSIDADE FEDERAL DO RIO DE JANEIRO
INSTITUTO DE FÍSICA

Amplitude Analysis of $D^+ \rightarrow K^- K^+ \pi^+$ Decay
with LHCb 2012 Data and RF-foil Simulations for
the LHCb Upgrade

Ph. D. Thesis

Daniel Evangelho Vieira

Thesis presented to the Ph. D. program in physics
of Instituto de Física, Universidade Federal do Rio
de Janeiro, as part of the necessary requirements
to obtain the title Dr. in Physics.

Advisor: Sandra Amato

Co-Advisor: Alberto Reis

Rio de Janeiro

Dec/2015.



**Amplitude Analysis of the $D^+ \rightarrow K^- K^+ \pi^+$ Decay with LHCb 2012
Data and RF foil Simulations for the LHCb Upgrade**

Daniel Evangelho Vieira

Sandra Filippa Amato
Alberto Correa dos Reis

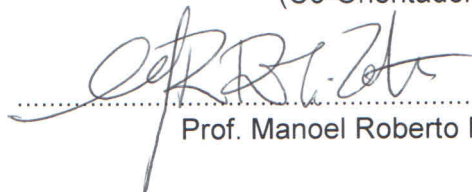
Tese de Doutorado submetida ao Programa de Pós-Graduação em Física, Instituto de Física, da Universidade Federal do Rio de Janeiro – UFRJ, como parte dos requisitos necessários à obtenção do título de Doutor em Ciências (Física).
Aprovada por:



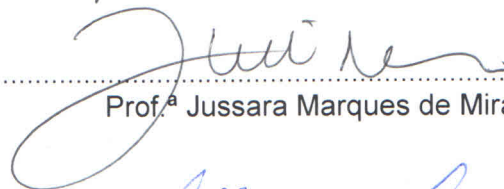
Prof.a Sandra Filippa Amato
(Presidente e Orientadora)



Prof. Alberto Correa dos Reis
(Co-Orientador)



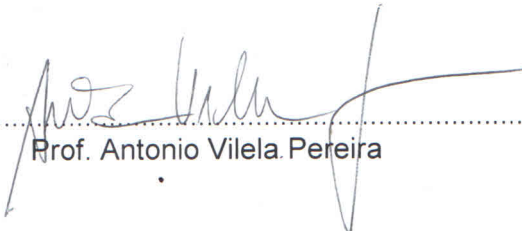
Prof. Manoel Roberto Robilotta



Prof.^a Jussara Marques de Miranda



Prof. Arthur Kós Antunes Maciel



Prof. Antonio Vilela Pereira



Prof. Daniel de Miranda Silveira

CIP - Catalogação na Publicação

V657a Vieira, Daniel Evangelho
 Amplitude Analysis of $D^+ \rightarrow K^- K^+ \pi^+$ Decay with
LHCb 2012 Data and RF-foil Simulations for the
LHCb Upgrade / Daniel Evangelho Vieira. -- Rio de
Janeiro, 2015.
 181 f.

 Orientadora: Sandra Amato.
 Coorientador: Alberto Reis.
 Tese (doutorado) - Universidade Federal do Rio
de Janeiro, Instituto de Física, Programa de Pós
Graduação em Física, 2015.

 1. LHCb. 2. Dalitz plot. 3. Análise de
amplitudes. 4. Física de altas energias. 5.
Charme. I. Amato, Sandra, orient. II. Reis,
Alberto, coorient. III. Título.

RESUMO

Análise de Amplitudes do Decaimento $D^+ \rightarrow K^- K^+ \pi^+$ com Dados do LHCb de 2012 e Simulações da Folha de Radioproteção para a Atualização do LHCb.

Daniel Evangelho Vieira

Advisor: Sandra Amato Co-Advisor: Alberto Reis

Resumo da Tese de Doutorado submetida ao Programa de Pós-graduação em Física, da Universidade Federal do Rio de Janeiro - UFRJ, como parte dos requisitos necessários à obtenção do título de Doutor em Ciências (Física).

O decaimento $D^+ \rightarrow K^- K^+ \pi^+$ é um processo hadrônico dominado por estados intermediários ressonantes. Para podermos compreender a natureza e quantificar cada uma dessas contribuições, uma análise de amplitudes deve ser realizada. A abordagem mais comum para esta questão é o chamado modelo isobárico, onde cada contribuição é descrita por uma combinação de funções Breit-Wigner, fatores de forma e funções de distribuição angular. Alcançar uma descrição precisa da distribuição dos dados utilizando o modelo isobárico é, porém, uma tarefa desafiadora uma vez que ele não contempla adequadamente ressonâncias largas e que se sobrepõem, típicas nas amplitudes de onda-S. Além disso, a altíssima estatística fornecida pelo LHCb potencialmente revela efeitos sutis relevantes para o nosso modelo. O LHCb vai passar por um processo de atualização para o próximo período de tomada de dados. O LHC fornecerá uma luminosidade muito superior a atual e todos os subsistemas serão atualizados visando aprimorar o desempenho do experimento e possibilitar o melhor uso possível dos dados. O detector de vértices do LHCb (*Vertex Locator* ou VELO) será atualizado, adotando sensores híbridos de pixel, e um novo modelo da folha de radioproteção será necessário para isso. Nesta tese,

apresentamos os primeiros resultados de ajustes de amostras de $D^+ \rightarrow K^- K^+ \pi^+$ do LHCb de 2012 utilizando o modelo isobárico e estudos de simulações da folha de radioproteção para a atualização do VELO.

Palavras-chave: Charme, Dalitz plot, Análise de amplitudes, LHCb, VELO, Upgrade, RF foil

Rio de Janeiro

Dec/2015

ABSTRACT

Amplitude Analysis of $D^+ \rightarrow K^- K^+ \pi^+$ Decay with LHCb 2012 Data and RF-foil
Simulations for the LHCb Upgrade

Daniel Evangelho Vieira

Advisor: Sandra Amato Co-Advisor: Alberto Reis

Abstract of the thesis presented to the Ph. D. program in physics of Instituto de Física, Universidade Federal do Rio de Janeiro, as part of the necessary requirements to obtain the title Dr. in Physics.

The $D^+ \rightarrow K^- K^+ \pi^+$ decay is a hadronic process dominated by resonant intermediate states. In order to quantify and understand the nature of each contribution, an amplitude analysis must be performed. The most common approach for this task is the Isobar Model, where each resonant contribution is described by a combination of Breit-Wigner functions, form factors and angular distribution functions. Achieving a precise description using the Isobar model is a challenging task since it does not provide an adequate framework for broad, overlapping structures typical from the S-wave amplitudes. Due to the huge statistics provided by LHCb, subtle effects might become relevant to our model. The LHCb experiment is going through an upgrade process for the next LHC run period. LHC will provide a much higher luminosity and all subsystems are required to upgrade in order to improve the experiment performance and make good use of the available data. The Vertex Locator, in particular, will be upgraded to a hybrid pixel detector and a new RF foil design is required for this. In this thesis, we show the first Isobar fit results for this channel using the 2012 LHCb data sample and simulation studies for the upgrade of the RF foil in order to achieve the best performance as possible.

Keywords: Charm, Dalitz plot, Amplitude Analysis, LHCb, VELO, Upgrade,
RF foil

Rio de Janeiro

Dec/2015

Acknowledgements

I'd like to thank my advisors Sandra Amato and Alberto Reis. They have advised me with incredible dedication and patience for quite some time now. I don't have enough words to thank all the knowledge, support, advice and opportunities they provided me. Working with them has been and will always be a pleasure.

Thanks to Lars and Tim, who advised me during my stay at CERN, always with attention and dedication.

I'd also like to thank my mother, Ione, and my brother, Eduardo. They have supported me through my whole Ph. D., specially when I most needed them. These have not been easy years and without their help I wouldn't be here.

Thanks also to Clarissa, who I love very much. Her support has also been vital for me and I am very lucky to count with it. The many years ahead of us will be awesome.

Many thanks to Oscar, who provided me lots of help with all kinds of problems I found, who has been a great friend and joined me for so many lunches and breaks during the entire Ph. D. Thank you to Leonardo too, for the friendship, support, and playing with me when possible. Thank you to Danielle too, who has always been one of the kindest and most generous people I know. Thank you also to all my friends from LAPE and aggregates, Ana Bárbara, Mariana, Márcio, Lucas, Saullo and Luis Gustavo.

I'd also like to thank the professors in the LHCb Rio Charm group, Érica and Carla, who always contributed with knowledge and experience. I'm grateful to Josué and Rafael, who worked long hours with me and provided me so many code lines. Thank you to the LAPE professors, Leandro, Miriam, Murilo, Hélder, Bruno, Juan, Irina and Kazu. Thanks to CBPF professors as well, Ignácio, Jussara and André.

Thanks to my colleagues at CERN, which were always dedicated and helped me so much, Tom Bird, Tom Latham, Rafael Coutinho, Daniel Craik, Sebastian Neubert, Tjeerd Kettel, Paula Collins, Heinrich Schindler and Pawel Jalocho.

Thanks to my friends from PUFA, who I can always count on. Thank you to my friends from Fanfarra, which I enormously cherish.

Thanks to my family for all the support.

Thanks to the Ph. D. program staff in Instituto de física, who always provided help and information with unique efficiency.

Most specially right now, I'd like to thank my father, who taught me so much, who was my professional reference and, even though he's not around anymore, who will always be with me.

To my father, Marco Antonio Vieira

Contents

Contents	xi
List of Figures	xiii
List of Tables	xxiv
1 Introduction	1
2 The LHCb Experiment	4
2.1 LHC	4
2.2 LHCb General Aspects	7
2.3 Beam pipe and Vacuum Chamber	9
2.4 Magnet	11
2.5 VELO	11
2.6 Tracking Stations	16
2.7 RICH	19
2.8 Calorimeters	22
2.9 Muon Chambers	23
2.10 Trigger	25
2.11 Stripping	26
2.12 LHCb Software Framework	27
3 LHCb Upgrade, VeloPix and RF foil studies	29

3.1	Tracker	30
3.2	Particle Identification System	31
3.3	Trigger	33
3.4	VELO Upgrade - VeloPix	34
4	The $D^+ \rightarrow K^- K^+ \pi^+$ Decay	40
5	Amplitude Analysis Formalism	45
5.1	Dalitz Plot	45
5.2	Isobar Model	50
5.3	Partial Wave Analysis	54
5.4	Fit Fraction	55
6	Rio+ Package for Dalitz Plot Analyses	56
6.1	Features	56
6.2	Toy Monte Carlo Generator	58
6.3	Maximum Likelihood Fitter	59
6.4	Least Squares Fitter	61
6.5	Code Validation	63
7	Data Sample and Selection Criteria	69
7.1	Data and MC samples	69
7.1.1	Data Samples	69
7.1.2	MC Samples	70
7.2	Selection Criteria	71
7.3	Stripping, Trigger and kinematic vetoes	73
7.4	Offline Selection	76
7.4.1	Specific backgrounds	78
7.4.2	Mass Fits	82
7.5	Background Dalitz Distribution	86

7.6	Signal Dalitz Distribution	89
8	Efficiency	91
8.1	Geometrical Acceptance, Reconstruction and Selection Efficiencies . .	92
8.2	PID Efficiency	93
8.3	Final Efficiency	94
9	Fit Model and Results	96
9.1	Fit Models	96
9.2	Fit Results	97
10	Discussion on Systematic Errors	107
11	Conclusion	110
	Bibliografia	113
A	Simulation Studies of the RF foil for the VELO Upgrade	119
A.1	Introduction	119
A.2	RFfoilCreator	121
A.3	Material scans and IP resolution plots	125
A.4	Conclusion	135
B	List of TCKs used in 2012 Data	136
C	Dalitz Distribution in 5 MeV/c^2 Windows	138
D	Rio+ - Usage	142
D.1	ToyMCGenerator	142
D.2	Log_Likelihood_Fitter	145
D.3	Chi2_Fitter	149
E	Ressonant Distribution Summary	155

List of Figures

2.1	Representation of the LHC accelerator with its four main experiments.	5
2.2	CERN accelerator complex.	7
2.3	Side vision of LHCb. Names indicate the position of each subdetector.	8
2.4	Simulation of the B meson production angular distribution, with respect to the beam.	8
2.5	Beam pipe representation.	10
2.6	Magnet representation.	12
2.7	Mapping of the y component of the magnetic field along the z axis. .	12
2.8	Representation of R-type (left) and ϕ -type (right) VELO sensors. . .	13
2.9	At the top, we have the representation of the VELO arrangement on a lateral point of view ((x,z) plane) and, below, the frontal representation of a station, in opened and closed positions.	13
2.10	Open view of VELO mechanical structure, with the roman pots holding one half of the modules and the RF-box.	14
2.11	Modules and RF foil in closed position.	14
2.12	Average material contribution for tracks passing through VELO. . . .	15
2.13	Primary vertex resolution in the transverse plane (left) and along the z axis (right) for events with one PV as a function of track multiplicity.	16
2.14	IP_x resolution as a function of $1/p_T$ for 2012 data and MC samples. IP_y is nearly identical.	16

2.15	Decay time resolution as a function of momentum P of fake prompt $B_s^0 \rightarrow J/\psi\phi$ for events with exactly one PV.	17
2.16	Tracking stations TT, T1, T2 and T3. In purple we see the IT regions, while the OT is seen in blue.	17
2.17	TT station layers.	18
2.18	Frontal view of an IT station.	19
2.19	Side view of an OT module.	19
2.20	Side view of RICH1.	21
2.21	Side view of RICH2.	21
2.22	$\phi \rightarrow K^+K^-$ mass distribution, only with kinematical cuts.	21
2.23	$\phi \rightarrow K^+K^-$ mass distribution, with PID and kinematical cuts.	21
2.24	Module arrangement in SPD, PS and ECAL (left), and in the HCAL (right). Each color indicates a separated region, with distinct module configuration. The inner regions contain greater granularity, in order to deal with the higher occupancy.	22
2.25	Region division in the muon chambers. Each rectangle represents one chamber.	24
2.26	Data flux through the trigger system.	27
3.1	L0 trigger yields for distinct B meson decays.	30
3.2	UT layers geometry.	31
3.3	SFT modules design. Note that the dimensions are not proportional, the dead area is enlarged for a better view.	31
3.4	Schematic view of the TORCH module.	32
3.5	Upgrade trigger scheme.	34
3.6	Front and rear view of the upgraded VELO module. Sensors are shown in red and the microchannel cooling substrate in blue.	36
3.7	Schematic view of the upgraded VELO.	37
3.8	RF foil design for the VELO upgrade.	37

3.9	Material contributions for the upgraded VELO.	37
3.10	IP resolution for the current VELO in black and the upgraded VELO in red. In light gray we see the relative population of b-hadron daugh- ters in each bin.	38
3.11	IP resolution with different foil thickness configurations. In red the nominal thickness of $250 \mu m$ is used, while in orange we have $167 \mu m$, in green, $83 \mu m$ and no foil in blue (0 thickness). In light gray the relative population of b-hadron daughters is shown.	38
3.12	IP resolution for partially thinned RF foil with different thicknesses on the region around the beam, compared to the current VELO. In black, the IP resolution for the current VELO is shown. In red, magenta and blue are shown the upgraded VELO IP resolution for RF foils with inner thickness of $300 \mu m$, $200 \mu m$ and $100 \mu m$, respectively. In green, the configuration without RF foil is shown.	39
4.1	Decay diagram of the type $D^+ \rightarrow R(\rightarrow K^-\pi^+)K^+$	41
4.2	Decay diagram of the type $D^+ \rightarrow R(\rightarrow K^-K^+)\pi^+$	41
4.3	Annihilation decay diagram of the type $D^+ \rightarrow R(\rightarrow K^-\pi^+)\pi^+$	42
4.4	Dalitz plot of the $D^+ \rightarrow K^-K^+\pi^+$ decay with LHCb 2012 data. . . .	44
5.1	Dalitz plot boundary and distinct final state momentum configura- tions that occur in each region of the (s_{12}, s_{31}) plane. In the extremi- ties we have the configuration in which one of the final state particles is at rest, while in the intermediate regions we see the events were one of the particles have maximum momentum.	49
5.2	A non-resonant (left) and a resonant (right) decay.	51
6.1	Simplified fluxogram of the ToyMCGenerator algorithm.	60
6.2	Simplified fluxogram of the Log Likelihood Fitter algorithm.	62
6.3	Simplified fluxogram of the Chi2 Fitter algorithm.	64

6.4	Fit results for the real part of the $K^*(892) + K$ resonant coefficient. On the left we see the distribution of fit results for the parameter itself, while on the right we see the error distribution, both fitted by Gaussians.	65
6.5	Comparison between fitted (grey triangles) and generation (blue squares) values for the real part of the MIPWA S-wave amplitude.	68
6.6	Comparison between fitted (grey triangles) and generation (blue squares) values for the imaginary part of the MIPWA S-wave amplitude.	68
7.1	Impact parameter representation.	72
7.2	Representation of the θ angle, used to calculate the DIRA, shown in red.	73
7.3	$K^-K^+\pi^+$ Mass distributions for MagDown (left) and MagUp (right) as they come out of the Stripping 20.	74
7.4	Fit to Mass distributions of $D^+ \rightarrow K^-K^+\pi^+$ for MagDown (left) and MagUp (right) as they come out of the Stripping 20.	74
7.5	Fit to Mass distributions of $D^+ \rightarrow K^-K^+\pi^+$ for MagDown (left) and MagUp (right) after the trigger requirements.	76
7.6	Distortion given by a cut in $p3_IPCHI2 > 6$. This cut would discriminate candidates reconstructed with a random pion, but it introduces a large distortion. The distributions correspond to the Dalitz plot after applying the cut divided by the one before applying it.	78
7.7	$D^+ \rightarrow K^-K^+\pi^+$ candidates reconstructed as $K^-p\pi^+$ in the MagDown data sample after the stripping and trigger requirements.	79
7.8	$K^-K^+\pi^+$ (right) and $K^-\pi^+K^+$ (left) mass distribution of true MC $D_s^+ \rightarrow$ $\phi\pi^+\pi^0$ after the inclusive stripping.	80
7.9	DIRA distribution for MC true $D^+ \rightarrow K^-K^+\pi^+$ (black) and true $D_s^+ \rightarrow$ $\phi\pi^+\pi^0$ (red) after the stripping selection.	80
7.10	LogIPChi2 distribution for MC true $D^+ \rightarrow K^-K^+\pi^+$ (black) and true $D_s^+ \rightarrow \phi\pi^+\pi^0$ (red) after the stripping selection and DIRA > 0.9999975	80

7.11	KK π mass distribution from true MC $D_s^+ \rightarrow K^-K^+\pi^+$ events after stripping selection (solid black) and after all final cuts (dotted red).	81
7.12	D FD χ^2 for MC $D_s^+ \rightarrow \phi\pi^+\pi^0$ (red), $D_s^+ \rightarrow K^-K^+\pi^+$ (blue) and $D^+ \rightarrow K^-K^+\pi^+$ (black) after the stripping selection, DIRA > 0.9999975 and logIPChi2 > 13.	81
7.13	Dalitz plot of $D^+ \rightarrow K^-K^+\pi^+$ in the mass region 1910–1930 (left) and after applying the D Vertex $\chi^2 < 15$ (right).	82
7.14	KK π Mass distribution of true $D^+ \rightarrow K^-\pi^+\pi^+\pi^0$ MC events without $\Delta \log \mathcal{L}_{K\pi}$ cut (left) and after $\Delta \log \mathcal{L}_{K\pi} > 15$ (right).	82
7.15	Distortion given by each selection criteria. The distributions correspond to the Dalitz plot after applying the cut divided by the one before applying it.	84
7.16	$K^-K^+\pi^+$ mass fit for the data sample after all selection criteria, using both magnet polarities. The D^+ yield is around 8.5×10^6 events.	85
7.17	$K^-K^+\pi^+$ mass fit for the data sample after all selection criteria requiring TOS with respect to the L0 Hadron trigger lines, using both magnet polarities. The D^+ yield is nearly 3×10^6 events.	85
7.18	$K^-K^+\pi^+$ mass fit for the data sample after all selection criteria requiring TIS with respect to the L0 muon, electron, photon and hadron lines using, both magnet polarities. The D^+ yield is over 6×10^6 events.	86
7.19	$K^-K^+\pi^+$ mass fit of the LHCb MC sample for the $D^+ \rightarrow K^-K^+\pi^+$ decay after all selection criteria requiring TOS with respect to L0 hadron line using both magnet polarities.	87
7.20	$K^-K^+\pi^+$ mass fit of the LHCb MC sample for the $D^+ \rightarrow K^-K^+\pi^+$ decay after all selection criteria requiring TIS with respect to the L0 muon, electron, photon and hadron lines using both magnet polarities.	87
7.21	$K^-K^+\pi^+$ mass fit of the LHCb MC sample for the $D^+ \rightarrow K^-K^+\pi^+$ decay after all selection criteria, using both magnet polarities.	88

7.22	Background Dalitz distribution of the left mass sideband ($1820 < M_D < 1840 \text{ MeV}/c^2$).	88
7.23	Background Dalitz distribution of the right mass sideband ($1900 < M_D < 1920 \text{ MeV}/c^2$).	88
7.24	Background Dalitz distribution of the combination of both sidebands ($1820 < M_D < 1840 \text{ MeV}/c^2$ and $1900 < M_D < 1920 \text{ MeV}/c^2$)	89
7.25	High resolution background Dalitz histogram of the combination of both sidebands ($1820 < M_D < 1840 \text{ MeV}/c^2$ and $1900 < M_D < 1920 \text{ MeV}/c^2$), with TOS requirement with respect to the L0 hadron trigger line.	90
7.26	Dalitz plot of the $D^+ \rightarrow K^- K^+ \pi^+$ decay with LHCb 2012 TOS sample within the $2 \sigma_{eff}$ mass window.	90
8.1	Efficiency histogram for our sample, after simulating data acquisition, reconstruction and applying all selection criteria, but without including PID.	92
8.2	Efficiency histogram for our sample, after simulating data acquisition, reconstruction and applying all selection criteria, including the TOS requirement with respect to the L0 hadron trigger line, without including PID efficiency.	93
8.3	Efficiency histogram for our sample, after simulating data acquisition, reconstruction and applying all selection criteria, including the TIS requirement with respect to the L0 muon, electron, photon and hadron trigger lines, without including PID efficiency.	93
8.4	Efficiency histogram for our sample, after simulating data acquisition, reconstruction and applying all selection criteria and PID efficiency, including the TOS requirement with respect to the L0 hadron trigger line.	94

8.5	High resolution histogram of the efficiency for our channel considering data acquisition, reconstruction and selection effects, with PID correction.	95
9.1	Data distribution, PDF and resonant contributions provided in model 1 projected over the $s_{K-\pi^+}$ axis, on the left, and over the s_{K-K^+} axis on the right.	100
9.2	Data distribution, PDF and resonant contributions provided in model 1 projected over the $s_{K+\pi^+}$ axis, on the left, and the corresponding χ_i^2 distribution on the right.	101
9.3	Data distribution, PDF and resonant contributions of the fit with model 2, projected over the $s_{K-\pi^+}$ axis, on the left, and over the s_{K-K^+} axis on the right.	101
9.4	Data distribution, PDF and resonant contributions of the fit with model 2 projected over the $s_{K+\pi^+}$ axis, on the left, and the corresponding χ_i^2 distribution on the right.	102
9.5	Data distribution, PDF and resonant contributions of the fit with model 3 projected over the $s_{K-\pi^+}$ axis, on the left, and over the s_{K-K^+} axis on the right.	103
9.6	Data distribution, PDF and resonant contributions of the fit with model 3 projected over the $s_{K+\pi^+}$ axis, on the left, and the corresponding χ_i^2 distribution on the right.	104
9.7	Data distribution, PDF and resonant contributions of the fit model 4, where resonant contributions with free mass and widths are underlined in the legends, projected over the $s_{K-\pi^+}$ axis, on the left, and over the s_{K-K^+} axis on the right.	105

9.8	Data distribution, PDF and resonant contributions of the fit model 4, where resonant contributions with free mass and widths are underlined in the legends, projected over the $s_{K+\pi^+}$ axis, on the left, and the corresponding χ_i^2 distribution on the right.	106
A.1	Foil corrugation viewed from the VELO top perpendicular to the z-x plane. The inserts show the corrected corner positions to obtain the correct 3D foil thickness. The SlotDepthX parameter size is indicated at the sensor position.	123
A.2	Foil corrugation viewed in the beam direction perpendicular to the y-x plane. with the thin foil area highlighted in red. Left insert shows the 0.3 mm and the 0.1 mm thick foil cross sections. Right insert shows the size of the MillingRadius parameter.	123
A.3	Single foil corrugation with the thin foil area highlighted in red. . . .	124
A.4	Material scans of the RF foil with full 300 μm thickness. Plots (a), (b) and (c) show the percentage of radiation length for the foil before the first hit, before the second hit and total, respectively.	127
A.5	Material scans of the RF foil with 100 μm thickness at the region within $-22\text{mm} < y < 22\text{mm}$ (44 mm width) and 300 μm thickness elsewhere. Plots (a), (b) and (c) show the percentage of radiation length for the foil before the first hit, before the second hit and total, respectively.	128
A.6	Material scans of the RF foil with 100 μm thickness at the region within $-42\text{mm} < y < 42\text{mm}$ (84 mm width) and 300 μm thickness elsewhere. Plots (a), (b) and (c) show the percentage of radiation length for the foil before the first hit, before the second hit and total, respectively.	129

- A.7 Projections of the material scans, in ϕ and η coordinates, of the RF foil designs with 300 μm thickness on the outer region of the foil and with a 44 mm wide inner thickness of 100 μm (green), 200 μm (red) and 300 μm (black). Plots (a), (b) and (c) show the ϕ projections of the scans before the first hit, before the second hit and total, respectively, while (d), (e) and (f) are the η projections of the same scans 130
- A.8 Projections of the material scans, in ϕ and η coordinates, of the RF foil designs with 300 μm thickness on the outer region of the foil and with inner thickness of 100 μm , but with widths for the thin region that go from 44 mm to 84 mm in 10 mm steps. Plots (a), (b) and (c) show the ϕ projection of the scans before the first hit, before the second hit and total, respectively, while (d), (e) and (f) are the η projections of the same scans 131
- A.9 Projections of the material scans, in ϕ and η coordinates, of the RF foil designs with 300 μm , 400 μm and 500 μm thickness on the outer region of the foil, inner thickness of 100 μm and with width for the thin region of 44 mm. Plots (a), (b) and (c) show the ϕ projection of the scans before the first hit, before the second hit and total, respectively, while (d), (e) and (f) are the η projections of the same scans 132
- A.10 IP resolution vs. $1/p_t$ of samples generated using distinct RF foil designs. It is possible to see the current VELO in black, the upgrade VELO with full 300 μm thick foil in red, the upgrade VELO with 44 mm wide 200 μm foil in pink, the upgrade VELO with 44 mm wide 100 μm foil in blue and the upgrade VELO with no foil in green. 133

A.11	IP resolution vs. $1/p_t$ of samples generated using upgrade VELO and three different RF foil designs. The 300 μm uniform thickness foil is shown in red, the partially thinned foil with a 44 mm wide 200 μm thin region is shown in pink, with solid line and circle symbol, and the partially thinned foil with a 84 mm wide 200 μm thin region is shown in pink, but with dashed line and triangle markers.	133
A.12	IP resolution vs. $1/p_t$ of samples generated using upgrade VELO and three different RF foil designs, with 300 μm (blue), 400 μm (magenta) and 500 μm (orange) outer region thickness. All three shapes used a inner region thickness of 100 μm	134
C.1	Dalitz distribution in 5 MeV/c^2 windows. Units in each plot subcaption is also in MeV/c^2	139
C.2	Dalitz distribution in 5 MeV/c^2 windows. Units in each plot subcaption is also in MeV/c^2	140
C.3	Dalitz distribution in 5 MeV/c^2 windows. Units in each plot subcaption is also in MeV/c^2	141
E.1	$K^*(892)$ resonant contribution to the $D^+ \rightarrow K^- K^+ \pi^+$ decay on 2D (left) and 3D (right) plots.	155
E.2	$K^*(1430)$ resonant contribution, with Breit-Wigner formulation, to the $D^+ \rightarrow K^- K^+ \pi^+$ decay on 2D (left) and 3D (right) plots.	155
E.3	$a_2(1320)$ resonant contribution to the $D^+ \rightarrow K^- K^+ \pi^+$ decay on 2D (left) and 3D (right) plots.	155
E.4	$K^*(1680)$ resonant contribution to the $D^+ \rightarrow K^- K^+ \pi^+$ decay on 2D (left) and 3D (right) plots.	155
E.5	$K_1^*(1410)$ resonant contribution to the $D^+ \rightarrow K^- K^+ \pi^+$ decay on 2D (left) and 3D (right) plots.	156

E.6	$K_2^*(1430)$ resonant contribution to the $D^+ \rightarrow K^- K^+ \pi^+$ decay on 2D (left) and 3D (right) plots.	156
E.7	κ resonant contribution, with a Breit-Wigner formulation with constant width, to the $D^+ \rightarrow K^- K^+ \pi^+$ decay on 2D (left) and 3D (right) plots.	156
E.8	$K^*(1430)$ resonant contribution, with a Flatté-like formulation, to the $D^+ \rightarrow K^- K^+ \pi^+$ decay on 2D (left) and 3D (right) plots.	156
E.9	κ resonant contribution, with a pole function formulation, to the $D^+ \rightarrow K^- K^+ \pi^+$ decay on 2D (left) and 3D (right) plots.	156
E.10	$f_0(980)$ resonant contribution, with Flatté formulation, to the $D^+ \rightarrow$ $K^- K^+ \pi^+$ decay on 2D (left) and 3D (right) plots.	156
E.11	$f_0(X)$ resonant contribution to the $D^+ \rightarrow K^- K^+ \pi^+$ decay on 2D (left) and 3D (right) plots.	156
E.12	$f_0(1500)$ resonant contribution to the $D^+ \rightarrow K^- K^+ \pi^+$ decay on 2D (left) and 3D (right) plots.	156
E.13	$f_0(1710)$ resonant contribution to the $D^+ \rightarrow K^- K^+ \pi^+$ decay on 2D (left) and 3D (right) plots.	157
E.14	$f_2(1270)$ resonant contribution to the $D^+ \rightarrow K^- K^+ \pi^+$ decay on 2D (left) and 3D (right) plots.	157
E.15	$f_2'(1525)$ resonant contribution to the $D^+ \rightarrow K^- K^+ \pi^+$ decay on 2D (left) and 3D (right) plots.	157
E.16	$\phi(1020)$ resonant contribution to the $D^+ \rightarrow K^- K^+ \pi^+$ decay on 2D (left) and 3D (right) plots.	157
E.17	$\phi(1680)$ resonant contribution to the $D^+ \rightarrow K^- K^+ \pi^+$ decay on 2D (left) and 3D (right) plots.	157
E.18	$a_0(1450)$ resonant contribution to the $D^+ \rightarrow K^- K^+ \pi^+$ decay on 2D (left) and 3D (right) plots.	157

List of Tables

5.1	Blatt-Weisskopf form factors for angular momentum $L = 0, 1, 2$ with two distinct formulations.	52
6.1	Generation parameters of the code validation tests, inspired in the CLEO model.	63
6.2	Comparison table between generation parameters and fitted values for fits with 100 integrations points. P_{gen} stands for generation parameters, μ is the mean of the fitted Gaussian over the fit results distribution and the last column is the pull. Fit results are not in good agreement with generation parameters.	66
6.3	Comparison table between the widths of Gaussian fits and errors provided by the fit with 100 integrations points. σ_{Gaus} stands for the width of the Gaussian fit over the fit result distribution, σ_{fit} is the mean of the Gaussian fit over the error distribution and the last column is the pull. Fit errors are compatible with the observed distribution, even though a discrepancy can be seen.	66

6.4	Comparison table between generation parameters and fitted values for fits with 250 integrations points and the special integration on the $\phi(1020)$ region. P_{gen} stands for generation parameters, μ is the mean of the fitted Gaussian over the fit results distribution and the last column is the pull. Fit results are in good agreement with generation parameters.	67
6.5	Comparison table between the widths of Gaussian fits and errors provided by the Dalitz fits with 250 integrations points and the special integration on the $\phi(1020)$ region. σ_{Gaus} stands for the with of the Gaussian fit over the fit result distribution, σ_{fit} is the mean of the Gaussian fit over the error distribution and the last column is the pull. Fit errors are compatible with the observed distribution, even though a discrepancy can be seen.	67
6.6	Fit results for the $D^+ \rightarrow \pi^- \pi^+ \pi^+$ decay using the Rio+ package. . .	68
6.7	Fit results for the $D^+ \rightarrow \pi^- \pi^+ \pi^+$ decay using the Laura++ package. . .	68
7.1	Cuts applied at generator level.	70
7.2	Monte Carlo simulated data samples for signal and specific backgrounds. .	71
7.3	Stripping 20 cuts for StrippingD2hhh_KKPLine and StrippingD2hhh_HHHIncLine . . .	75
7.4	Selection criteria for HLT2CharmHadD2HHH	76
7.5	Hlt1TrackAllL0 requirements on at least one track	77
7.6	Kinematically vetoed regions of the p and η phase space such that the data-driven PIDCalib method may be properly utilized.	77
7.7	Offline cuts. The efficiency is obtained by fitting the data sample and is calculated with respect to the previous cut.	83
9.1	Resonant parameters used in the fit.	98

9.2	Summary of model composition. Elements marked with \surd are included in the corresponding model, with $\surd\surd$ are included with floating mass and width and with - are not included.	99
9.3	Fit results for model 1.	100
9.4	Fit results for the CLEO model with model 2.	102
9.5	Fit results for model 3. The first 7 resonant channels are the contributions given in the CLEO model, while the remaining resonances follow the order of addition to the fit model.	103
9.6	Fit results for model 4. The first 6 resonant channels are the contributions given in the CLEO model, with exception of the $a_0(1450)$ that was removed, while the remaining resonances follow the order of addition to the fit model.	105
B.1	TCKs used in 2012. The fraction indicates how many data, after the stripping selection, were taken with these TCK. The values of the cuts used in the <code>Hlt1TrackAllLO</code> and <code>LOHadron</code> are also shown.	137

Chapter 1

Introduction

The Large Hadron Collider beauty (LHCb) experiment [1] is one of the four large experiments of the Large Hadron Collider (LHC) at CERN [2]. Two of these experiments — CMS and ATLAS — probe the Standard Model (SM) and search for new physics exploring the limit of high energy, where possible new particles would be produced and observed directly (e.g. the recent observation of the Higgs boson).

The LHCb experiment has an alternative and complementary strategy, exploring the high intensity regime, searching for physics beyond the SM through indirect effects of higher energy scales that appear in rare phenomena. Following this strategy, the experiment was designed for studies of quark mixing, CP violation and rare decays of hadrons containing quarks c and b .

These studies include a comprehensive program on charm physics. One of the main topics of the charm physics program in LHCb is the systematic analysis of three-body decays of D mesons. One of the subjects of this thesis is part of this program: the Dalitz plot analysis of the decay $D_s^+ \rightarrow K^- K^+ \pi^+$.

The LHCb experiment took data from 2010 to 2012, a period which is referred to as Run I. After a two-years shutdown, the experiment is currently taking data in what is called Run II, which should last until 2018. Run II will be followed by another shutdown period, in which most detector components will be upgraded.

The other subject of this thesis are the studies performed for the upgrade of the VERtEX LOcator (VELO) detector, developed during a one year stay at CERN. Several subdetectors compose the LHCb detector, each one providing a distinct type of measurement. The VERtEX LOcator (VELO) [3] is one of these subdetectors and it is responsible for measuring the position of charged particles with high precision near the interaction region, providing excellent trajectory reconstruction allowing the determination of the proton-proton collision point and the B or D decay position, with enough resolution to distinguish them. This is a very important feature, since a signature of B and D mesons is that they travel significant distances before decaying. In order to be able to take measurements close to the interaction region, the VELO is placed inside a vacuum chamber. Two Radio-Frequency (RF) aluminium foils separate the VELO vacuum from the beam vacuum, providing shielding against RF radiation from the beam and helping to suppress wake fields induced by the beam.

The LHCb is going through a major upgrade during the next Long Shutdown (LS) period [4, 5]. Several subdetectors will be redesigned and the VELO is one of them [6]. The VELO detection technology, currently of silicon microstrips sensors, will be replaced by hybrid silicon pixel modules. A new RF foil must be designed in order to fit in the upgrade geometry, attending the operational requirements. By performing simulations we are able to study the RF foil impact on the measurements and to make choices focusing on the best possible performance.

This thesis is organized as follows. Chapter 2 gives a general overview of the LHCb experiment with special attention to the VELO subdetector. Next, we describe the LHCb and VELO upgrade projects, including the simulation studies of the RF foil in chapter 3 and appendix A. Afterwards, in chapter 4, we discuss the general motivation and expectations with respect to the amplitude analysis of the $D^+ \rightarrow K^- K^+ \pi^+$ decay. Chapter 5 presents general aspects of Dalitz plot and amplitude analysis in 3-body decays. A description of the Rio+ package, used for the amplitude analysis and developed as part of this thesis, is given in chapter 6. De-

tails about selection criteria, mass fits and background contributions are presented in chapter 7. The study of the efficiency variation across the Dalitz plot is presented in chapter 8. Chapter 9 shows the obtained fit results for the amplitude analysis, followed by a discussion of systematic effects in chapter 10. Conclusions are discussed in chapter 11.

Chapter 2

The LHCb Experiment

The Large Hadron Collider beauty Experiment (LHCb) is one of the four main experiments at the Large Hadron Collider (LHC). Its main purposes are to study CP violation and rare decays in B and D meson systems, fields where physics beyond the standard model may be found. The detector is composed by several subsystems, each with its own function. In this chapter, a general view of LHC and LHCb, with its main features, will be presented. Special attention will be given to the Vertex Locator, since this thesis contains direct contributions to the Upgrade of this subdetector.

2.1 LHC

Built by the *Organisation Européenne pour la Recherche Nucléaire* (CERN), on the border between Swiss and France, the LHC [2] is the largest particle accelerator currently running. The accelerator has a circumference of 27 km and it is situated at the same tunnel as its predecessor, the Large Electron-Positron Collider (LEP), at approximately 100m below ground level (fig. 2.1).

The four main experiments at LHC are:

- **ALICE** (*A Large Ion Collider Experiment*) - An experiment focused in ob-

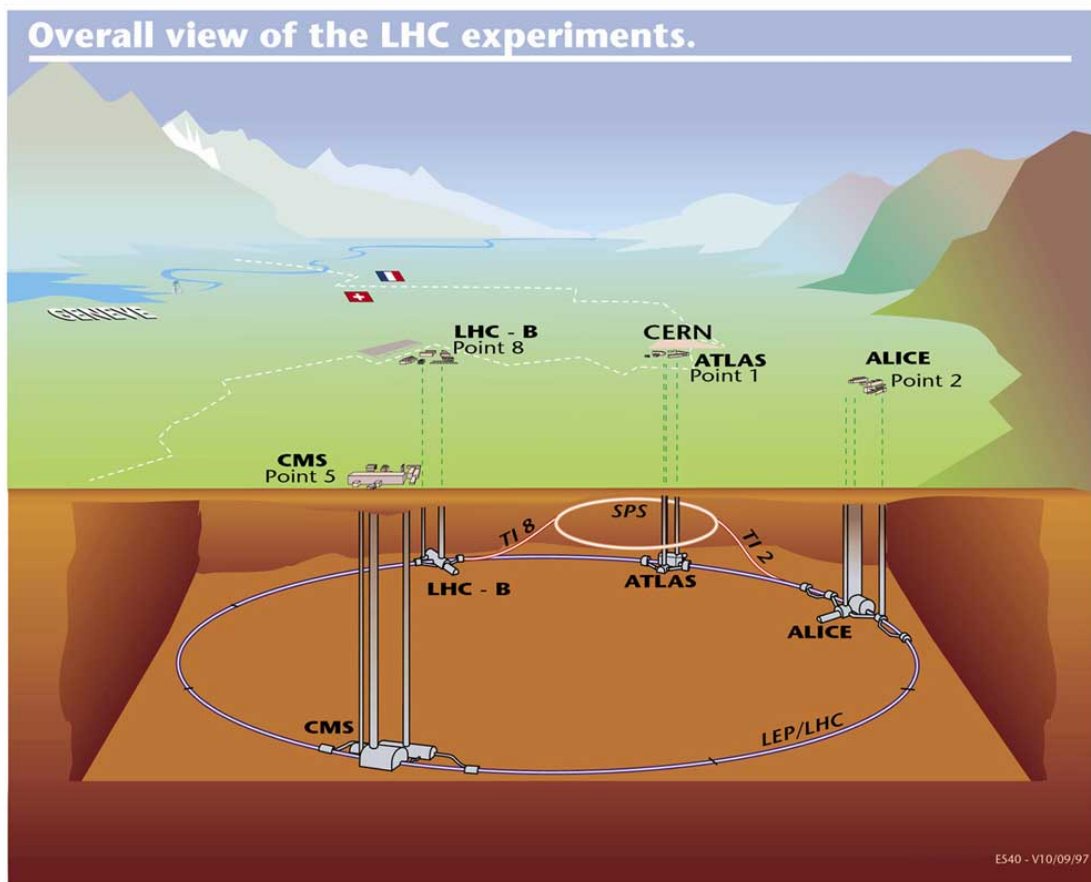


Figure 2.1: Representation of the LHC accelerator with its four main experiments.

serving lead ions collisions with protons to study the quark gluon plasma. [7].

- **ATLAS** (*A Toroidal LHC Apparatus*) - A general purpose experiment. It is the largest between the four main experiments. It was involved in the Higgs boson discovery and it studies many other topics, such as extra dimensions and dark matter [8].
- **CMS** (*Compact Muon Solenoid*) - Also a general purpose experiment, such as ATLAS, but with a complementary strategy, focusing in better momentum resolutions [9].
- **LHCb** (*The Large Hadron Collider Beauty Experiment for Precision measurements of CP Violation and rare Decays*) - A more general view about LHCb will be given in the next sessions [1].

The LHC was projected to collide 2 proton beams (or heavy ions) with a total of 14 TeV energy on the center of mass rest frame and with a luminosity of $L = 10^{34} \text{cm}^{-2} \text{s}^{-1}$. To achieve such a luminosity, the accelerator would be filled with two beams, both with 2808 bunches of protons of around 1.1×10^{11} protons each. With this configuration, it would provide a bunch crossing every 25 ns. Previous accelerators contain inferior energy and luminosity levels. For example, Tevatron, a proton-antiproton circular collider built at FermiLab, achieved a 2 TeV energy at the center of mass and a luminosity of $3 \times 10^{32} \text{cm}^{-2} \text{s}^{-1}$.

In 2012, however, the accelerator worked with a different configuration. Energy and luminosity conditions had been lower than nominal since it started running. Slowly increasing its parameters, year by year, it worked with 4 TeV energy-per-beam, 1380 bunches-per-beam and 1.48×10^{11} protons-per-bunch, achieving peak luminosities of $L = 0.7 \times 10^{34} \text{cm}^{-2} \text{s}^{-1}$.

In order to be accelerated in LHC, the beams must have an initial energy of 450 GeV. A pre-acceleration system is used for this purpose (fig. 2.2). Protons from hydrogen atoms go through a linear accelerator (LINAC2), where they achieve an energy of 50 MeV. Afterwards, the beam is inserted in the Proton Synchrotron Booster (PSB), where it acquires the energy of 1.4 GeV. The proton bunches are, then, sent to the Proton Synchrotron (PS) and accelerated up to the energy of 25 GeV. Finally, the beam is inserted in the Super Proton Synchrotron (SPS), where they reach the necessary energy to go to LHC.

Beams injected in LHC run in opposite directions inside separated beam pipes, kept in high level vacuum and at the temperature of -271°C . The acceleration is provided by superconducting magnets: 1232 magnetic dipoles, responsible for driving the beam, and 392 magnetic quadrupoles, responsible for the beam focusing. When the beams achieve the appropriate energy they are crossed in specific points to collide. The experiments are located in these points, where each takes its own data for analyses.

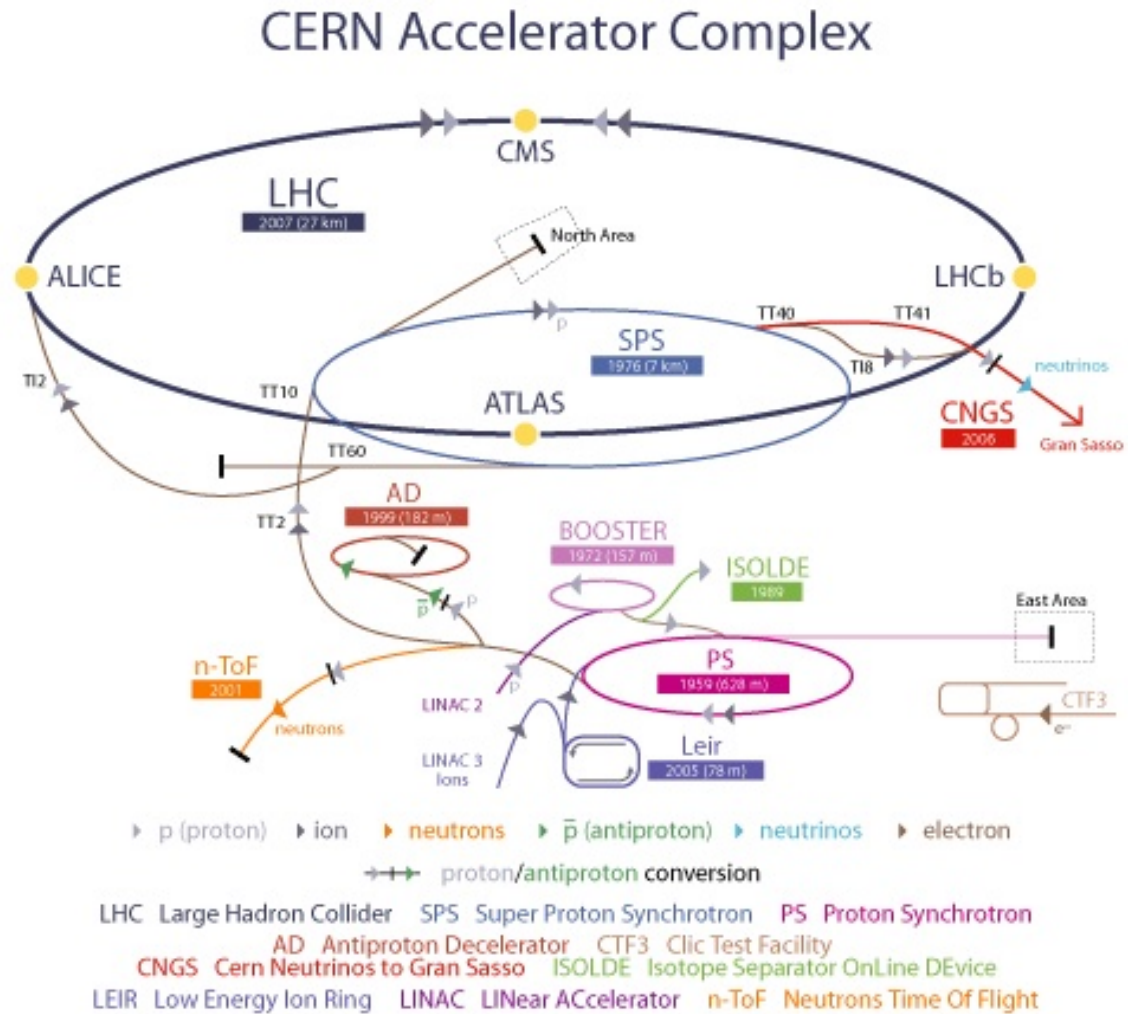


Figure 2.2: CERN accelerator complex.

2.2 LHCb General Aspects

The single-arm LHCb geometry is similar to the one in fixed target experiments, having an angular acceptance between 10 mrad and 300 mrad on the horizontal plane and 10 mrad to 250 mrad on the vertical plane (fig. 2.3). This geometry was chosen because the B meson is predominantly produced at smaller angles, closer to the beam (fig. 2.4). This way, around 40 % of the $B\bar{B}$ pairs are produced inside LHCb acceptance.

The nominal luminosity for LHCb in 2012 was $2 \times 10^{32} \text{cm}^{-2}\text{s}^{-1}$, smaller than for the other experiments because of the detector geometry, but enough to acquire large samples of B and D meson samples, enabling studies of rare decays and precise

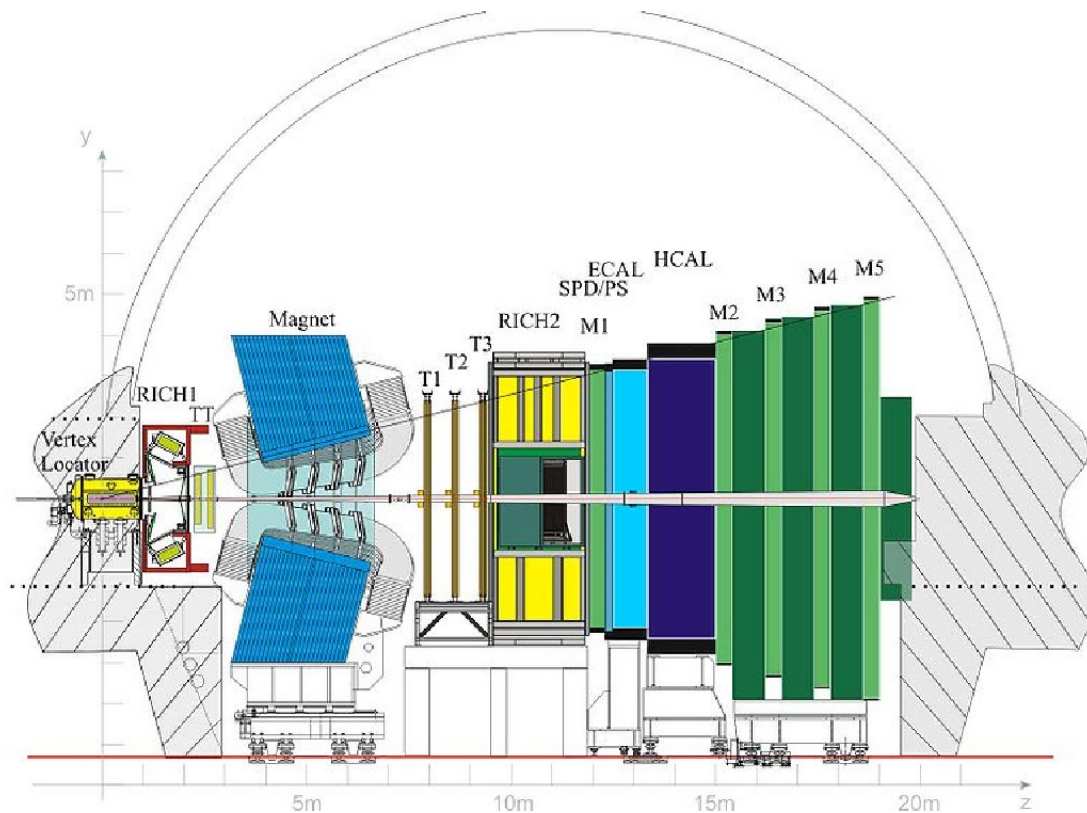


Figure 2.3: Side vision of LHCb. Names indicate the position of each subdetector.

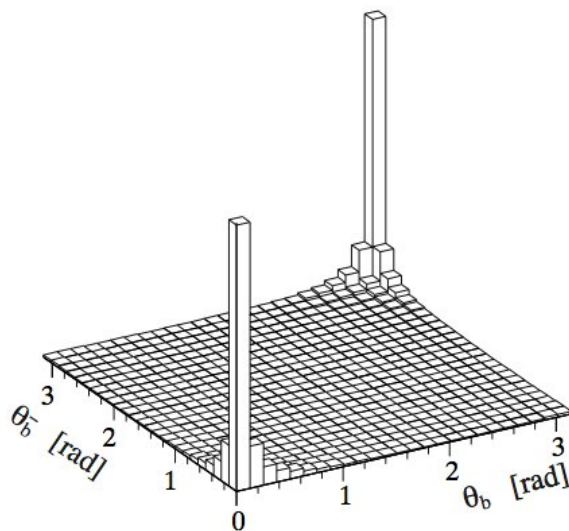


Figure 2.4: Simulation of the B meson production angular distribution, with respect to the beam.

CPV measurements.

In order to make these measurements, it is necessary to have a good precision

in vertex and track reconstruction. B and D mesons typically travel distances of $O(1)$ cm with respect to the primary vertex before decaying and, therefore, it is vital to be able to separate well those vertices as well as to identify which tracks are produced in each one. Good particle identification, decay time and mass resolution are also important. Moreover, the number of produced events is much higher than the storage capacity requiring, thus, to filter the acquired data, storing only the most relevant events based on the characteristics of the decay. The mechanism responsible for this task is called trigger system.

The LHCb is composed by a set of subdetectors (fig. 2.3). The VERtEX LOcator (VELO) is the subdetector responsible for measuring particle positions near the interaction region, providing good track and vertex reconstruction. The Ring Image Cherenkov 1 (RICH1) purpose is to provide particle identification in the low momentum range. Tracking stations TT, T1, T2 and T3 measure particle position before and after the magnet, granting track reconstruction and momentum measurement. The magnet bends the tracks, allowing the measurements of particles charge and momentum. The Ring Image Cherenkov 2 (RICH2) identifies high momentum particles. Electromagnetic and Hadronic Calorimeters (ECAL and HCAL) contribute to the particle identification, by separating electrons and photons from kaons, protons and pions, and to the trigger, by providing the energy deposition measurement. Finally, the Muon stations identify muons, measuring their positions.

The detector coordinate system is such that the z axis lays in the beam direction, x axis is on the horizontal plane and y on the vertical plane. The full detector performance report for the first years of operations can be seen in [10]

2.3 Beam pipe and Vacuum Chamber

The segment of the beam pipe where LHCb is located was specially designed considering its mechanical, geometrical and performance requirements. Due to the

fact that LHCb is interested in events near the beam axis, its properties directly affect the measurements. Attributes such as mass, material, geometry and the presence of flanges and bellows have impact on the amount of material traversed by particles and, therefore, on the number of secondary interactions. Besides that, it is vital that the beam pipe endure the extreme pressure and temperature conditions to which it will be submitted during LHC operational periods.

The beam pipe is divided in four parts and connected to a vacuum chamber, which holds the VELO detector (fig. 2.5). The first three segments after the vacuum chamber, called UX85/1, UX85/2 and UX85/3, are composed by beryllium and are 1.9 m, 3.7 m and 6.0 m respectively. Beryllium was chosen due to its high transparency for particles and its elasticity. Its mechanical fragility, cost and toxicity are drawbacks. The last segment is made of stainless steel and is 5.3 m long. Bellows connecting beryllium segments are composed by aluminium, while the last bellow is made of stainless steel. The UX85/1 part has a conical geometry with 25 mrad angle. The other segments also have a conical shape, but with a 10 mrad angle.

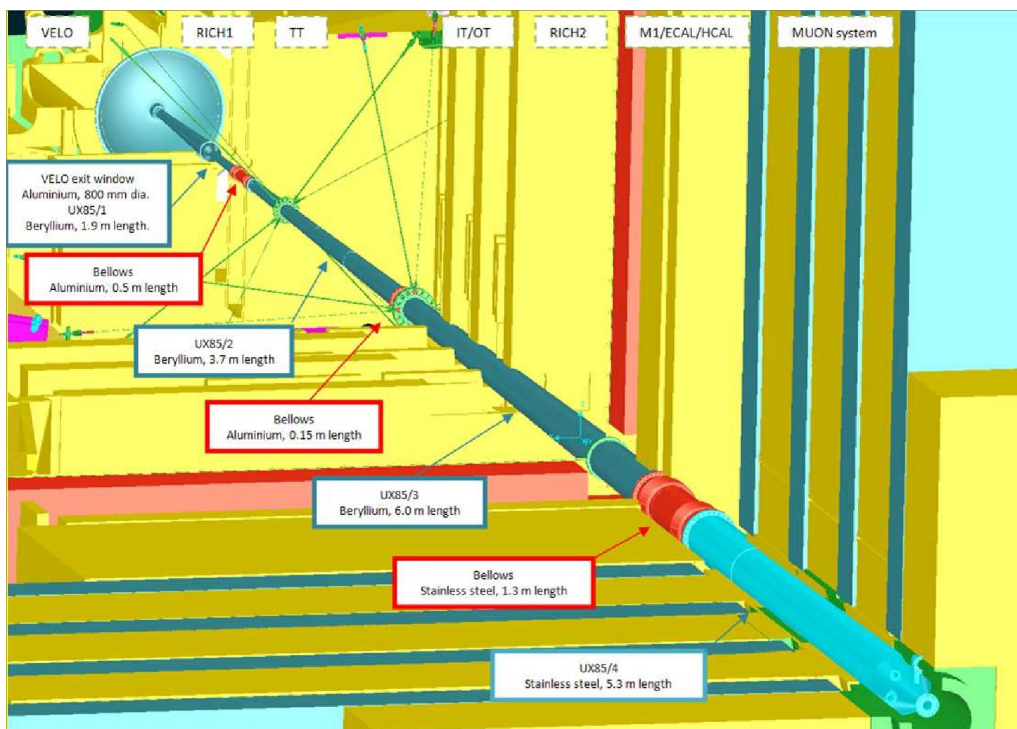


Figure 2.5: Beam pipe representation.

In order to reconstruct vertices with precision, VELO must be placed near the interaction region. A vacuum chamber was built to hold the detector in such position. With this configuration it is possible to place the detection modules 8 mm away from the beam. The chamber can reach a dynamical pressure between 10^{-8} and 10^{-9} mbar. The exit window is where the connection between the chamber and the beam pipe is established and it is made of stainless steel, also to get as few secondary interactions as possible, since the particles resulting from the proton-proton interaction traverse it.

2.4 Magnet

The LHCb magnet [11] is responsible for bending particle trajectories, enabling charge and momentum measurements. The magnetic dipole is composed by large, resistive coils in saddle shape, providing an integrated field of 4 Tm over a 10 m extension (fig. 2.6) and achieving a peak field of 1 T.

The magnet polarity can be reversed, allowing the field to be generated on both upwards and downwards directions along the vertical (y) axis, which contributes to systematic errors study, specially with respect to asymmetry measurements. The field mapping can be seen in figure 2.7.

2.5 VELO

The VELO [3] is the subdetector responsible by measuring positions of particles near the interaction region, enabling track and vertex reconstruction. The modules measure the position of traversing particles, providing its coordinates. By combining the measured positions, or hits, the reconstruction algorithms are able to recreate the particles trajectory, or tracks. Vertices may be reconstructed using tracks that point to the same region. B and D meson decay vertices (secondary vertices) are typically displaced from the proton-proton collision (primary vertex) by $O(1)$ cm.

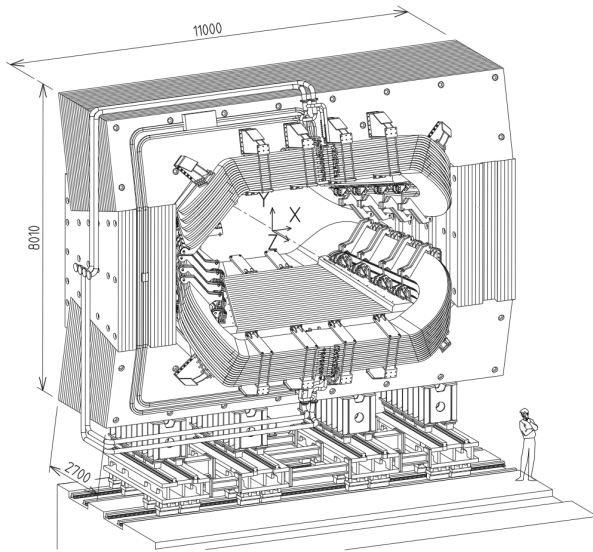


Figure 2.6: Magnet representation.

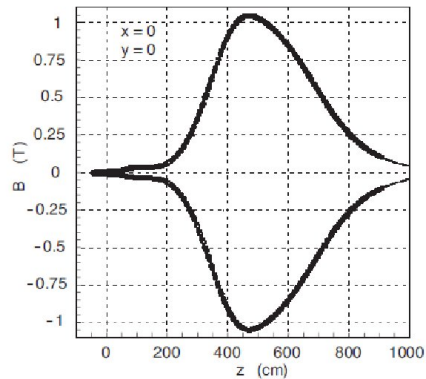


Figure 2.7: Mapping of the y component of the magnetic field along the z axis.

Therefore, it is essential to have an extremely precise vertex reconstruction.

The detector contains 21 stations, each composed by 2 modules and each module accommodates two types of sensors: R-type and ϕ -type (fig. 2.8). The number of stations and their position was planned requiring that each track inside LHCb angular acceptance crossed at least 3 stations (fig. 2.9). A few stations were installed on the $z < 0$ region in order to improve primary vertex reconstruction precision. Modules of a single station are separated by 1.5 cm along the z axis in order to overlap thus providing full azimuthal coverage.

The chosen technology for the detectors was the microstrip silicon sensors. Each R-type sensor is composed by concentric circular strips with pitches varying linearly from $38 \mu m$, at the inner region, to $101.6 \mu m$ at the outer region (fig. 2.8). R-type sensors are separated in four regions, each covering a 45° angle and containing 512 strips. ϕ -type sensors are divided in 2 regions: the inner area, that contains 683 strips, and the outer area, that contains 1365 strips. Strips at the inner region make a 20° angle with respect to the radial direction and have pitches between $39 \mu m$ and $78 \mu m$. The outer region strips have an angle of 10° with respect to radial direction and their pitches vary between $39 \mu m$ and $97 \mu m$. Both sensors are

In order to be able to make precise vertex measurements it is necessary that VELO acts extremely close to the interaction region. Therefore, the detector was installed inside the vacuum chamber with a rigid mechanical structure for support, responsible for precisely positioning the detector, called roman pots (fig. 2.10). This structure places the detector 8 mm away from the beam during data taking periods and draws it back to 6 cm away during beam injection and inactive periods. Modules must not be too close to the beam during its injection and focusing to avoid interactions and subsequent damage to the detector and to beam quality.

The two detector halves are placed inside a thin walled aluminium box, called Radiofrequency-box (RF-box), which maintains vacuum around sensors and are separated from the machine vacuum by a thin corrugated aluminium foil, called the Radiofrequency-foil (RF foil) (figs. 2.10 and 2.11). The RF foil has a few different purposes. It provides a vacuum tight separation between the primary vacuum of the beam pipe and the secondary vacuum of the detector, it shields the detector against RF pickup from the proton beams and it contributes to the suppression of wake fields that are induced in the detector by the beam by providing a continuous conductive surface between them. A wake field suppressor, located at the exit window, is also used for that purpose.

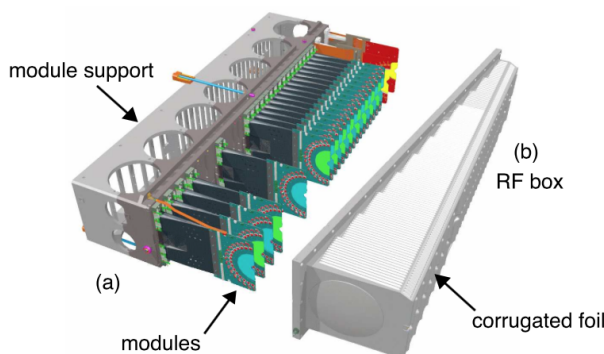


Figure 2.10: Open view of VELO mechanical structure, with the roman pots holding one half of the modules and the RF-box.

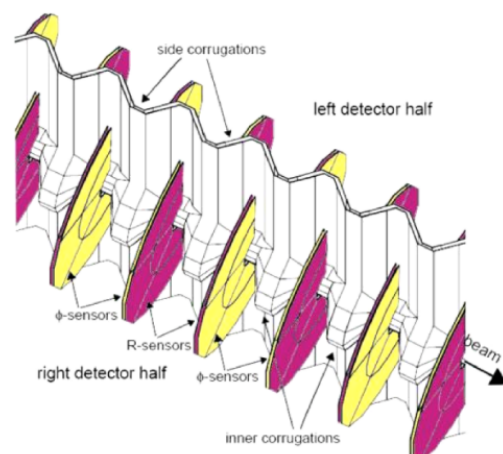


Figure 2.11: Modules and RF foil in closed position.

Aluminium was chosen as material for the RF foil due to its low material contribution, good electrical conductivity and its mechanical properties. The side walls of the box are 0.5 mm thick, while the corrugated foil is 0.3 mm. The corrugated geometry (fig. 2.11) was chosen to allow sensors to overlap and it reduces the length of material traversed before the first hit, where the impact of the secondary interaction on the reconstruction is larger. The RF foil is the largest material contribution and, as can be seen in figure 2.12, therefore, its design is extremely relevant to the VELO performance.

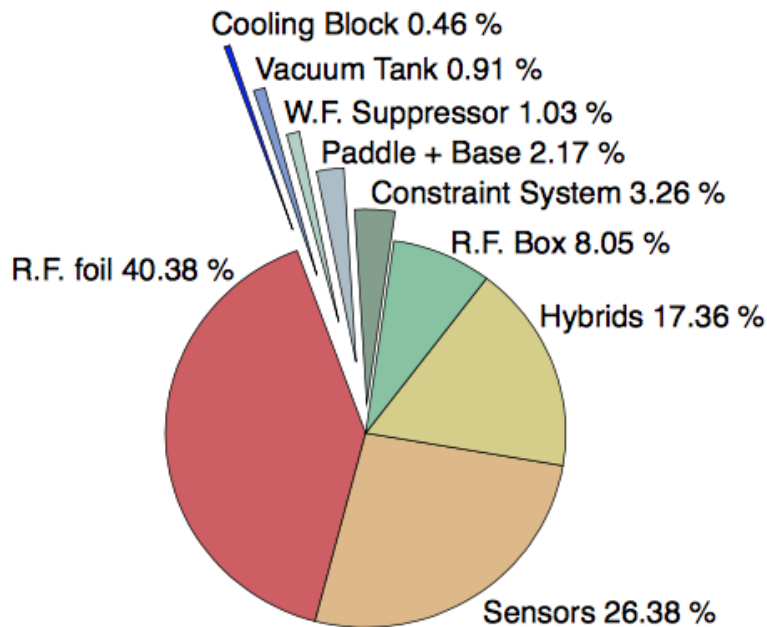


Figure 2.12: Average material contribution for tracks passing through VELO.

The full VELO performance report for the first years of operation, up to early 2013, can be seen at [12]. The primary vertex resolution achieved was $13 \mu\text{m}$ in the transverse plane and $71 \mu\text{m}$ along the z axis for vertices with 25 tracks (fig 2.13). The impact parameter resolution in the transverse plane was less than $35 \mu\text{m}$ for tracks with small transverse momentum, e.g. $p_T < 1\text{GeV}/c$ (fig. 2.14). Finally, the typical decay time resolution is of 50 fs (fig. 2.15). These features provide measurements with extraordinary precision and play a key role in LHCb physics program.

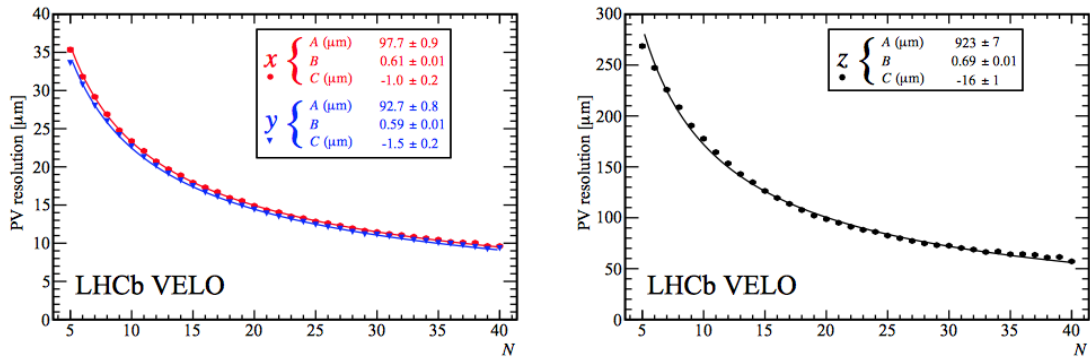


Figure 2.13: Primary vertex resolution in the transverse plane (left) and along the z axis (right) for events with one PV as a function of track multiplicity.

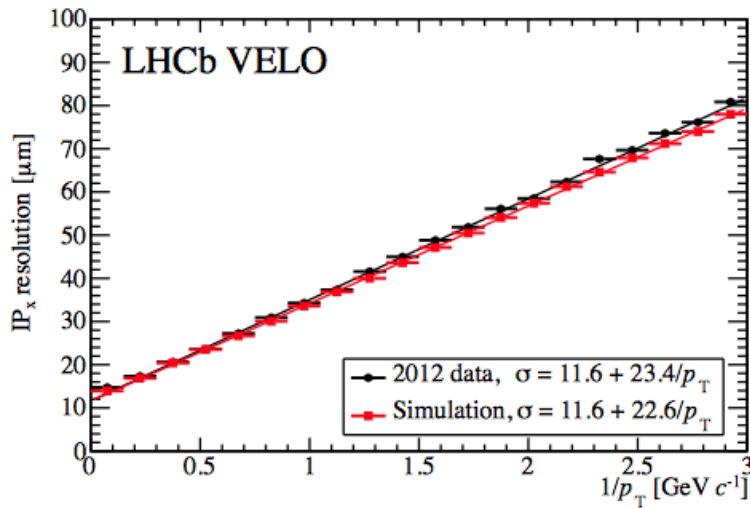


Figure 2.14: IP_x resolution as a function of $1/p_T$ for 2012 data and MC samples. IP_y is nearly identical.

2.6 Tracking Stations

The tracking stations are responsible for measuring positions before and after the magnet, which provides the necessary information to calculate the momentum of each particle. Together with VELO, they compose the tracking system, which reconstructs particles tracks in LHCb. The tracking stations are the Tracker Turicensis (TT), located before the magnet, and stations T1, T2 and T3, placed after the magnet (fig. 2.16). Tracking stations T1, T2 and T3 are divided in two regions: the inner area, with higher occupancy, is called the Inner Tracker (IT) [13], while

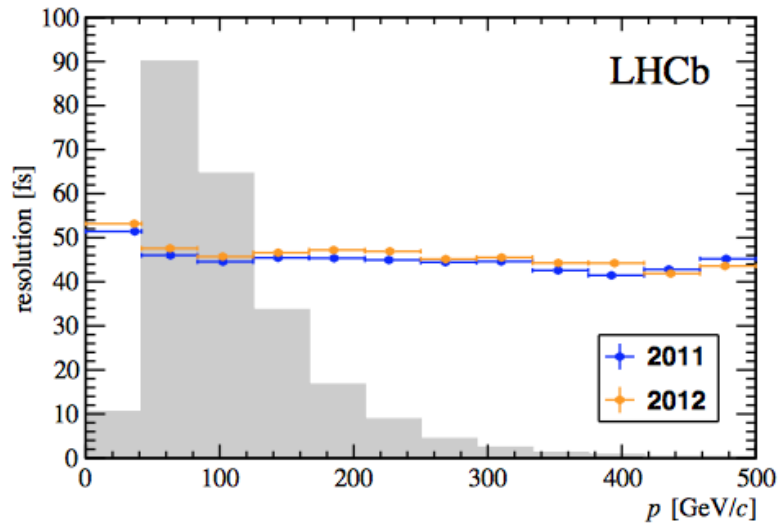


Figure 2.15: Decay time resolution as a function of momentum P of fake prompt $B_s^0 \rightarrow J/\psi\phi$ for events with exactly one PV.

the outer zone is called the Outer Tracker (OT) [14].

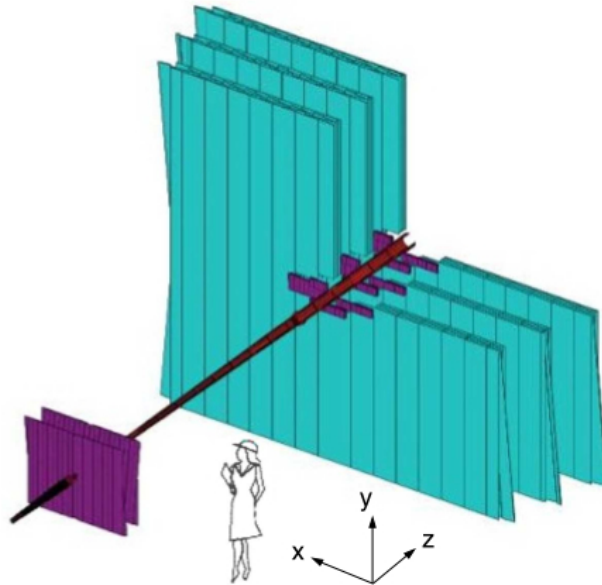


Figure 2.16: Tracking stations TT, T1, T2 and T3. In purple we see the IT regions, while the OT is seen in blue.

TT stations are built with microstrip silicon sensors and are 150 cm wide and 130 cm high (fig. 2.17). Four detector layers, arranged in two pairs, which are displaced by around 27 cm along the z axis, form each station. A 5° inclination

with respect to the y axis is given to one of the layers, while a second one has an inclination of -5° . This geometry is called “x-u-v-x”.

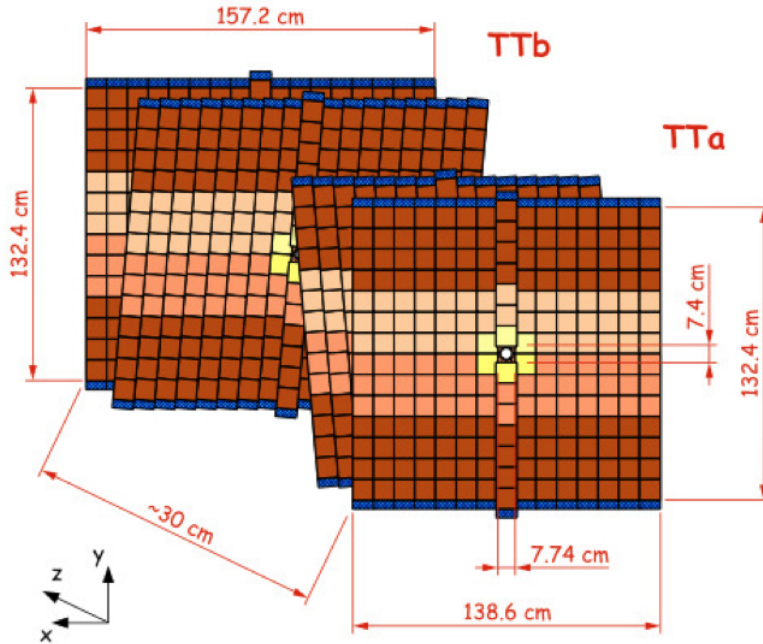


Figure 2.17: TT station layers.

Each TT sensor is 9.64 cm wide and 9.44 cm high, containing 512 silicon strips with a pitch of $183 \mu m$. Sensors are $500 \mu m$ thick and provide a spacial resolution of $50 \mu m$.

The technology chosen for the IT was similar to the one used in the TT, of silicon microstrips. The IT is located at the inner region, and therefore with higher occupancy, of the stations T1, T2 and T3. The detector is composed by four layers, also with the “x-u-v-x” geometry, divided in four boxes, each containing 7 modules (fig. 2.18). Each module has one sensor, if located at the superior or inferior box, or two, if it is placed at one of the side boxes.

Sensors contain 384 strips with a $198 \mu m$ pitch. Their thickness is $320 \mu m$ for the two sensor modules or $410 \mu m$ for the one module sensor and their resolution is a little higher than μm .

The OT stations are also formed by four layers with “x-u-v-x” geometry. The detectors are composed by straw tubes, a type of drift-time gas chambers. Each layer

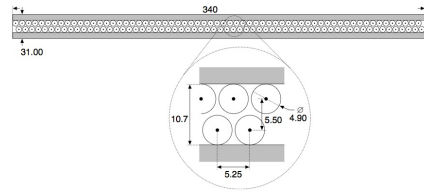
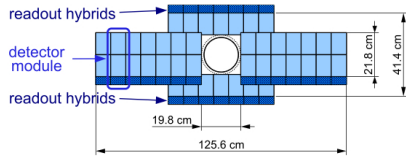


Figure 2.18: Frontal view of an IT station. Figure 2.19: Side view of an OT module.

is composed by two superimposed tube planes, arranged in a dislocated fashion, in order to avoid dead regions (fig 2.19). The tubes are filled with a mixture of Argon (70%) and CO_2 (30%), which guarantees a small drift time and a resolution of $200 \mu\text{m}$. The active area of the stations is $5971 \times 4850 \text{mm}^2$, with 96 S-type modules, which are shorter and cover the region directly above and below the beam pipe, and 168 long modules, which cover the remaining area. Long modules hold 256 tubes, while short modules hold 128 tubes.

Tracking stations were designed to provide a precise track reconstruction and, therefore, a good resolution on the particles momenta ($\delta p/p \approx 0.4\%$), vital for the mass calculation of mesons B and D. Keeping that in mind, its design had to overcome challenging issues, such as the mechanical rigidity, necessary to provide a good alignment, the material budget, to avoid multiple scattering, electrical shielding, to avoid crosstalk and electronical noise, and radiation hardness, to guarantee the effective performance of the detector during the full operation period.

The report for the OT performance for the first years of operation can be seen at [15]. The report with respect to the radiation damage of the detector can be found at [16].

2.7 RICH

Together with muon stations, the hadronic and electromagnetic calorimeters, the Ring Imaging Cherenkov counters (RICH1 and RICH2) [17] are part of the particle identification system. Its purpose is to identify kaons, pions and protons,

a vital task in B and D meson studies, including this thesis. This identification is particularly important in studies of 3-body hadronic decays, since these are particles that dominate the final state in such decays.

In order to provide identification, the RICH mechanism uses Cherenkov radiation, emitted by particles with speed greater than the speed of light in the given medium. Having quantified the linear momentum of the corresponding track, it is possible to estimate the particle identity by measuring the angle of Cherenkov radiation photon emission. The irradiated photons form a cone with a typical angle given by the equation:

$$\cos \theta_c = \frac{1}{vn}.$$

where v is the particle speed and n is the refraction index of the medium.

The RICH1 is located between the VELO and the TT and it is responsible for identifying particles with low momenta, within the 1 GeV/c and 60 GeV/c range. The RICH2 is placed directly after T3 and it identifies particles with higher momenta, within the 15 GeV/c to 100 GeV/c range. The RICH1 (fig. 2.20) is filled with aerogel ($n = 1.03$) and C_4F_{10} ($n = 1.0014$) radiators and it was designed to minimize the active material, in order to avoid multiple scattering, by using low density mirrors. Its angular coverage is between 25 mrad and 300 mrad (250 mrad) on the vertical (horizontal) direction, where the inferior limit is set by the presence of the beam pipe. The irradiated photons are reflected by the mirrors and sent to Hybrid Photon Detectors (HPDs). The RICH2 detector (fig. 2.20) contains basically the same mechanism, but it is filled with CF_4 ($n = 1,0005$) and its angular acceptance is between 15 mrad and 120 mrad (100 mrad) on the horizontal (vertical) direction, covering the most likely region for high momentum particles to be produced. The report of the RICH detectors performance can be found in [18].

The particle identification provided by the RICH detectors has a strong discriminating power. Figures 2.22 and 2.23 show a K^+K^- mass distribution before and

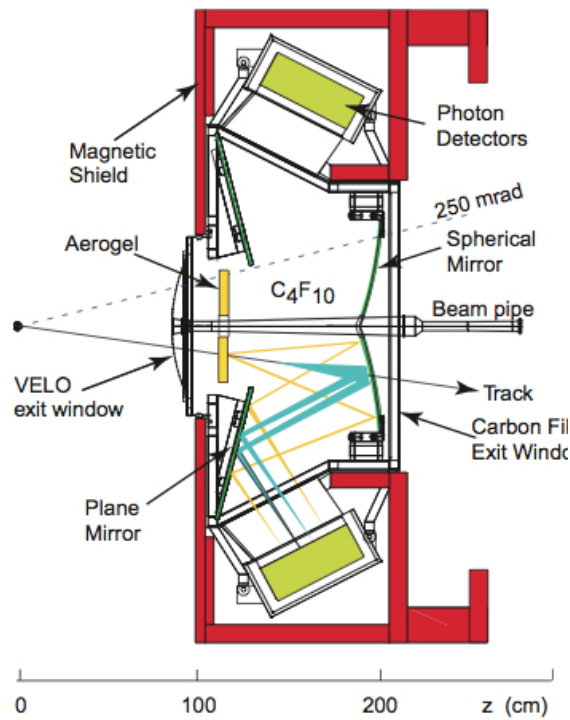


Figure 2.20: Side view of RICH1.

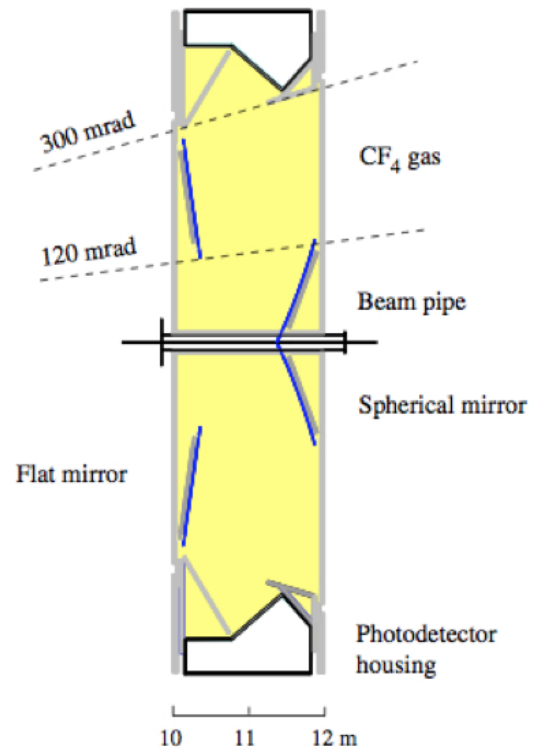
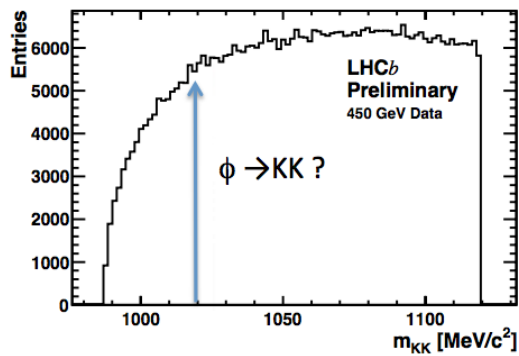
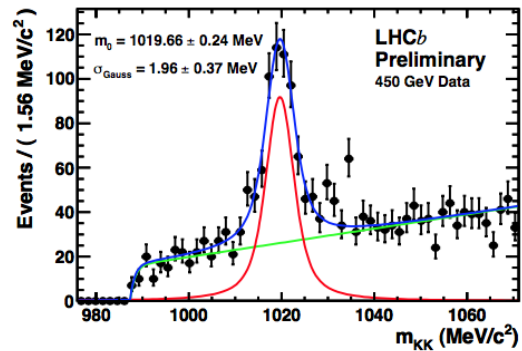


Figure 2.21: Side view of RICH2.

after PID cuts. The PID information improves drastically the signal over background ratio, unveiling the ϕ mass peak.

Figure 2.22: $\phi \rightarrow K^+K^-$ mass distribution, only with kinematical cuts.Figure 2.23: $\phi \rightarrow K^+K^-$ mass distribution, with PID and kinematical cuts.

2.8 Calorimeters

The calorimeters [19] provide transverse energy measurements for the first level of trigger decision and aids with the identification of electrons, photons and hadrons. It is composed by four parts: the Electromagnetic Calorimeter (ECAL) is responsible for measuring energies of electrons and photons, interrupting their trajectories, while the Hadronic Calorimeter (HCAL) is responsible for the same task, but with pions, kaons, protons and neutrons. The calorimeters also contain the Scintillator Pad Detector (SPD), which contributes to the rejection of electrons that are detected at the ECAL but are originated from π^0 , and the PreShower detector (PS), which rejects background due to charged pions.

The SPD and PS are placed before the ECAL, are separated by a lead layer of 15 mm and their active area is 7.6 m wide and 6.2 m high. They are composed by scintillating modules, as shown in figure 2.24. The lead layer was designed with a radiation length enough to generate a electromagnetic shower, but not a hadronic shower.

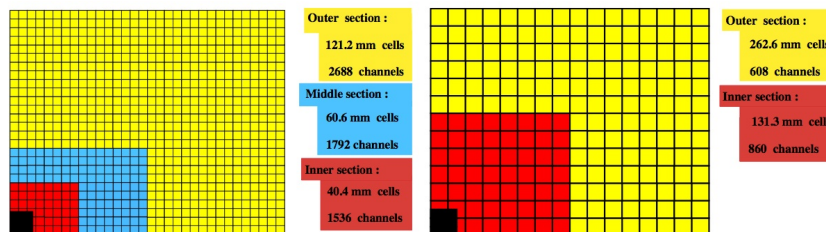


Figure 2.24: Module arrangement in SPD, PS and ECAL (left), and in the HCAL (right). Each color indicates a separated region, with distinct module configuration. The inner regions contain greater granularity, in order to deal with the higher occupancy.

The ECAL is composed by scintillating detectors, of shashlik technology, alternating 4mm scintillator tiles, 2 mm lead layers and $120 \mu\text{m}$ white, reflecting paper. When particles traverse the detector they interact, generating a shower of particles, a cascade reaction resulting from the interaction between the measured particle and the detector material. By collecting the photons irradiated from the

shower, the ECAL is able to measure its energy. The ECAL is designed to prevent electrons and photons from traversing it. The energy resolution provided is $\sigma_E/E = 10\%/\sqrt{E} \oplus 1\%$.

The HCAL is also composed by scintillating detectors, alternating 4mm scintillating tiles with 16mm iron layers. The mechanism is similar to the ECAL, but focused on stopping and measuring the energy of protons, kaons, pions and neutrons. Its structure can be seen in figure 2.24. The HCAL energy resolution is of $\sigma_E/E = 80\%/\sqrt{E} \oplus 10\%$.

2.9 Muon Chambers

The LHCb has five muon chambers, called M1-M5 [20]. Their purpose is to provide information to the muon trigger and identification system. While M1 is located before the SPD, in order to measure muon trajectories before they are scattered in the calorimeters and, this way, achieve a better linear momentum resolution for the trigger, the chambers M2-M5 are placed after the calorimeters. Only muons are supposed to reach the muon chambers M2-M5. In order to avoid hadron contamination, 80 cm iron absorbers are put between muon chambers.

The muon chambers are divided in regions, according to their occupancy rate, as seen in figure 2.25. The predominant technology is the Multi-Wire Proportional Chamber (MWPC). The innermost region of M1, however, used Gas Electron Multiplier (GEM) chambers due to its high occupancy rate. MWPC's are composed by gas chambers, filled with a mixture of Argon (40%), CO₂ (55%) and CF₄ (5%), containing a plane of gold-plated tungsten wires of 30 μm diameter each. When a muon traverse the chamber, the gas is ionized and the ions are collected by the cathode, on the chamber walls, while the electrons are captured by the anode, one of the wires. The GEM chambers have 3 foils, sandwiched between anode and cathode planes and submitted to high voltage. The foils contain small holes that collect

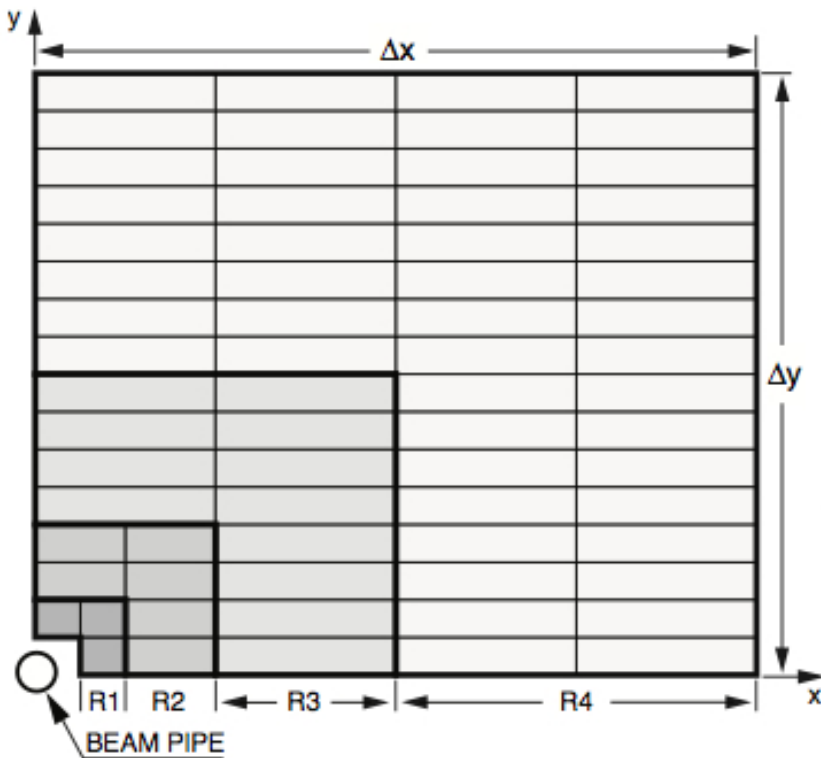


Figure 2.25: Region division in the muon chambers. Each rectangle represents one chamber.

the electrons originated in the ionization. The GEM stations are also filled with a mixture of Argon (45%), CO_2 (15%) and CF_4 (40%).

The muon identification algorithm is composed by three steps. First, a binary response, called `isMuon`, is given based on the track penetration through the calorimeters and iron filters. This response is used in our analysis to reduce backgrounds coming from decays with muons on its final state. Second, a likelihood is computed considering the muon and non-muon hypotheses, and the logarithm of the ratio between both hypotheses gives a discriminating variable called `muDLL`. Finally, a likelihood is calculated considering muon and pion particle hypotheses, taking into account information from the calorimeters and RICH detectors. The third step also produces a discriminating variable given by logarithm of the ratio between the muon and pion hypotheses.

The full LHCb muon identification performance can be seen at [22]. The `isMuon`

tag, used in our analysis, achieves misidentification rates between 6.2% and 0.33%, depending on the particle and the transverse momentum range, providing good discrimination against muon backgrounds.

2.10 Trigger

With a nominal luminosity of $2 \times 10^{32} \text{cm}^{-2} \text{s}^{-1}$, LHCb data rate is about 10 MHz. The storage rate, on the other hand, is 4 kHz. Therefore, it is necessary to have a system that selects the events, among all available data, based on physical criteria, in order to reduce the data acquisition rate. The trigger system [59] was developed with this purpose.

The trigger system is segmented in two levels. The first level, called L0, is implemented on the acquisition electronics and reduces the data rate to 1 MHz. The selected events are processed in a computer farm, where they are submitted to the second level of the trigger, the High Level Trigger (HLT), which is software based. The HLT is further divided in two sublevels, the HLT1 and the HLT2. The HLT1 confirms the L0 trigger decision with higher precision and a few additional information, reducing the data rate to 10 kHz, while the HLT2 uses fast reconstruction algorithms in order to apply stronger criteria to the data selected by Hlt1, finally reducing the rate to the desired 4 kHz.

Since the L0 acts on the electronic level, its decision must be extremely fast ($4 \mu\text{s}$), to allow subdetectors to proceed with the data flux, or not, without harming the measurement of subsequent events. The L0 decision is based on simple information such as the occupancy level of the detectors, preferably not too high due to the complexity of events with high multiplicity, and the presence of particles with high transverse momentum, which are typically produced in B and D meson decays. These criteria are variable, being softer or stronger depending on the needs of the experiment. All criteria are applied in parallel, but all detector information is taken

to the L0 decision unit (L0DU), where a single response is given with respect to the approval or refusal of the entire event, e.g., no event can be partially accepted.

The HLT criteria may also fluctuate according to operation conditions and interest. The HLT acts on the Event Filter Farm (EFF), a set of about 2000 computers. Due to the necessity of quick responses and the limited computational resources, the HLT algorithms must adopt simplified criteria. The C++ programming language was used to develop the algorithms due to its satisfactory processing speed performance. The HLT1 improves the precision of the L0 decision by adding impact parameter measurements and additional VELO information, achieving a linear momentum resolution of $\delta p/p = 1 - 2\%$. The HLT2 already makes full secondary vertices reconstructions applying criteria based on fast event reconstruction. This allows the HLT2 to select both inclusive and exclusive events of B and D meson decays. Trigger selection is divided in “lines”, according to sets of criteria and physical interest. Figure 2.26 shows the data flux through the trigger system and a full performance report for the trigger system can be found at [28].

Trigger selection often distorts data kinematical distributions due to its non-uniform efficiencies. In order to study trigger effects, the data is separated under two tags. The Trigger On Signal (TOS) tag identifies candidates whose daughter tracks triggered the event, while the Trigger Independent of Signal (TIS), identifies candidates that were in events triggered by other tracks.

2.11 Stripping

The acquired data is stored in Data Summary Tapes (DSTs) as raw data. After the data is permanently stored, it is submitted to reconstruction algorithms and an offline selection is performed, called Stripping, to reduce sample sizes in storage and to prepare data for analysis.

The selection criteria is divided in streams, each focused in distinct classes of

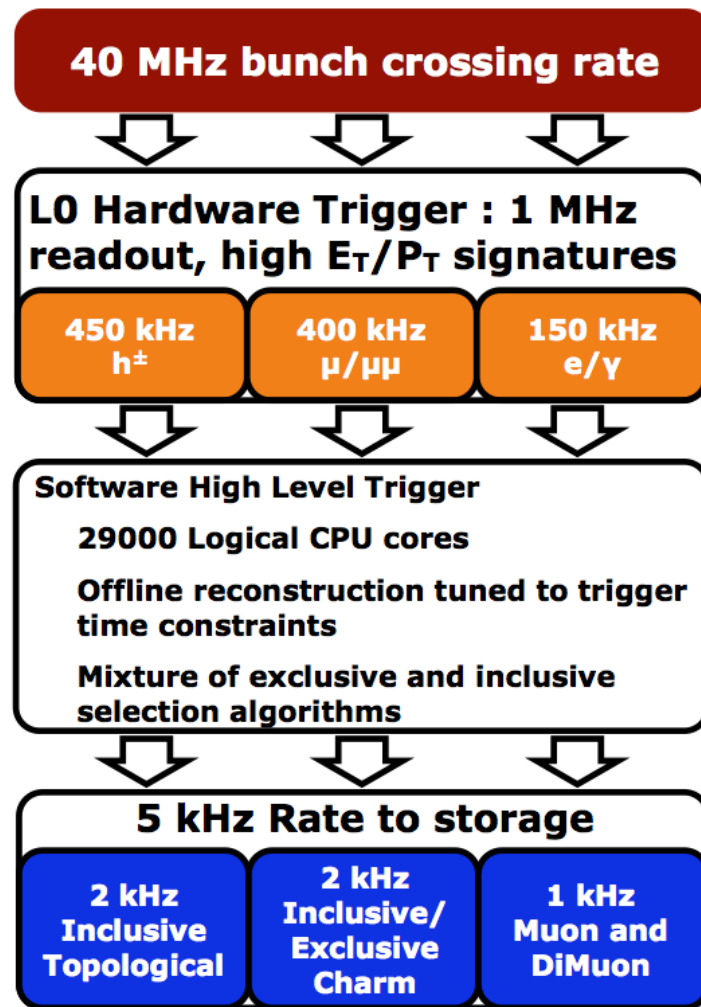


Figure 2.26: Data flux through the trigger system.

decays. Each stream is separated in stripping lines, one for each specific decay. Stripping selection criteria use offline variables obtained after reconstruction and are able to optimize the signal over background ratio.

2.12 LHCb Software Framework

LHCb software framework provides tools to perform tasks such as data reconstruction, selection and MC simulation. Each package has a distinct functionality.

The Gauss project is responsible for generating MC samples, using PYTHIA [24] event generator to simulate the collision dynamics and GEANT4 [25–27] to simulate

detector interaction with particles. Boole project simulates the electronic response and digitalization in data acquisition. Moore package controls HLT for both data and simulation, producing DST's in both cases. Brunel project provides track and vertex reconstruction. Finally, DaVinci package provides general tools for data analysis, for example, calculating variables for selection criteria. DaVinci supplies as output ntuples, which are standard files containing all data information, such as particle momenta, trigger responses, etc.

Chapter 3

LHCb Upgrade, VeloPix and RF foil studies

While in 2012 the LHCb took data with an average instantaneous luminosity of $4 \times 10^{32} \text{cm}^{-2} \text{s}^{-1}$, it is expected that the experiment will operate with a luminosity of $2 \times 10^{33} \text{cm}^{-2} \text{s}^{-1}$ after the next Long Shutdown (LS) [4], due to the improvement of LHC conditions. The current LHCb system, however, is not ideal for acquiring data in such circumstances. In order to make full profit of the potential provided by the LHC accelerator, an upgrade is required.

Considering the current L0 trigger, a larger data rate would imply stronger selection criteria and, therefore, a reduced efficiency. In fact, the hadronic yields are expected to saturate quickly as the luminosity increases, as can be seen in figure 3.1. An alternative approach is required and the most effective strategy to achieve a better yield is to move the entire trigger selection to software, supplying it with the full event information at a 40MHz rate.

Detectors must also be upgraded. Each detector must be re-designed considering the required precision, material budget, radiation hardness and occupancy rate.

The upgraded LHCb detector is expected to collect a sample of 50fb^{-1} . The huge amount of data, combined with the excellent detector precision, will provide

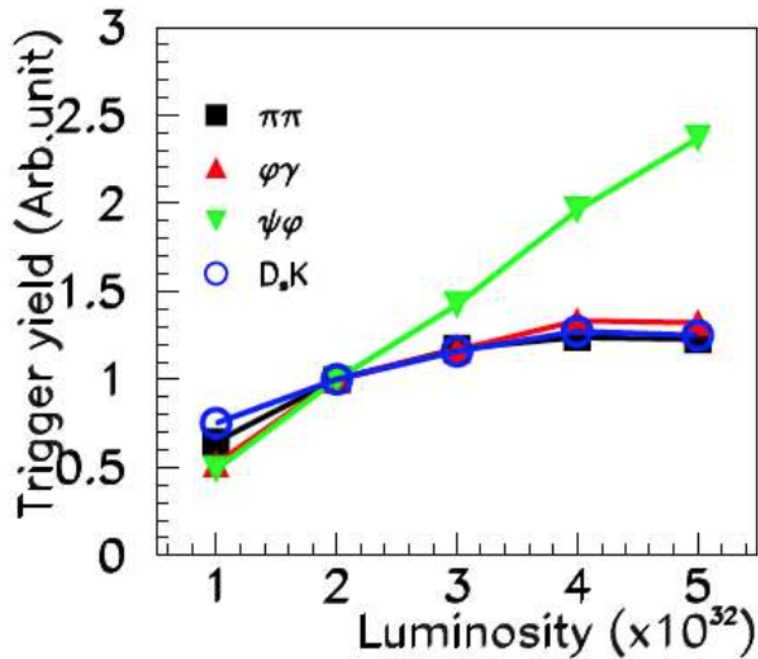


Figure 3.1: L0 trigger yields for distinct B meson decays.

resolutions on flavour observables improved by up to a factor 10 with respect to the current LHCb measurements [5]. The higher luminosity expands the fields LHCb can study and, due to its unique acceptance, complementary measurements with respect to other experiments can be made.

On the next sections, brief descriptions of the upgrade subsystems will be given. The VELO upgrade will be described in greater detail in section 3.4 since this is the topic where I have made a contribution.

3.1 Tracker

The current design of the tracking stations is insufficient to operate on the upgrade LHCb. The silicon sensors are not radiation hard enough, the expected occupancy rate saturates the detectors and the readout electronics is not compatible with the 40 MHz readout. Moreover, improving the performance is required in order to achieve the necessary resolution on the relevant observables and to select the larger amount of data on the trigger system. Therefore, an upgrade for the tracking

stations has been proposed [29].

The TT stations will be replaced by a new generation of micro-strip silicon detectors named Upstream Tracker (UT) (fig. 3.2). The same “x-u-v-x” geometry as the current TT will be used, but with higher granularity and eliminating gaps on the detection area.

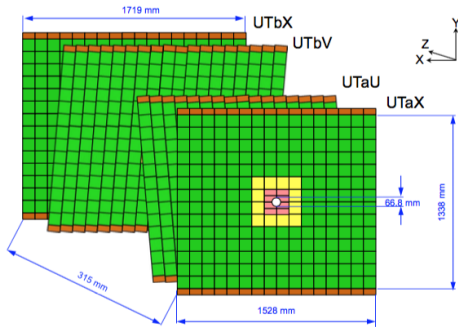


Figure 3.2: UT layers geometry.

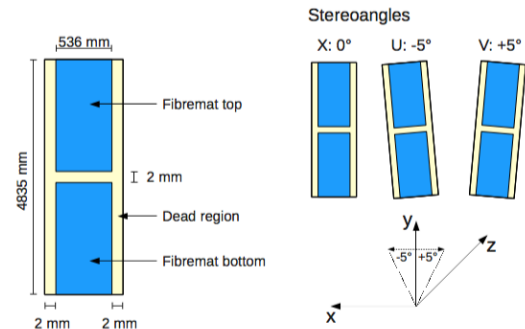


Figure 3.3: SFT modules design. Note that the dimensions are not proportional, the dead area is enlarged for a better view.

The T1, T2 and T3 will be fully replaced by a Scintillating Fiber Tracker (SciFi Tracker, or SFT) with silicon photo-detectors, also with “x-u-v-x” geometry (fig. 3.3). The SFT has the advantage of requiring less stringent temperature requirements with respect to silicon detectors, sufficient radiation hardness, high granularity and it allows the readout electronics to be placed outside the LHCb acceptance, reducing material contribution, one of the most crucial factors for the track reconstruction.

3.2 Particle Identification System

The subdetectors involved with the particle identification, the RICH1, RICH2, ECAL, HCAL and Muon chambers, will also be upgraded [30]. As well as to the other subdetectors, the higher luminosity conditions and the 40 MHz readout requirements will affect their operational needs.

The overall structure of the RICH detectors will remain unchanged. The RICH1

detector, however, demands significant modifications due to its performance at high luminosities. The aerogel will be removed and, as a consequence, the optical design had to be adjusted accordingly. Photon detectors must also be replaced in both RICH detectors with a new generation, the multianode photomultipliers (MaPMTs), capable of operating at 40MHz rate.

A sub new detector is being considered in order to recuperate the low momentum particle identification performance. The Time Of internally Reflected Cherenkov light (TORCH) (fig. 3.4) detector is based on the measurement of the time of travel of Cherenkov light produced by particles traversing a quartz plane, but it is still on early R&D stages.

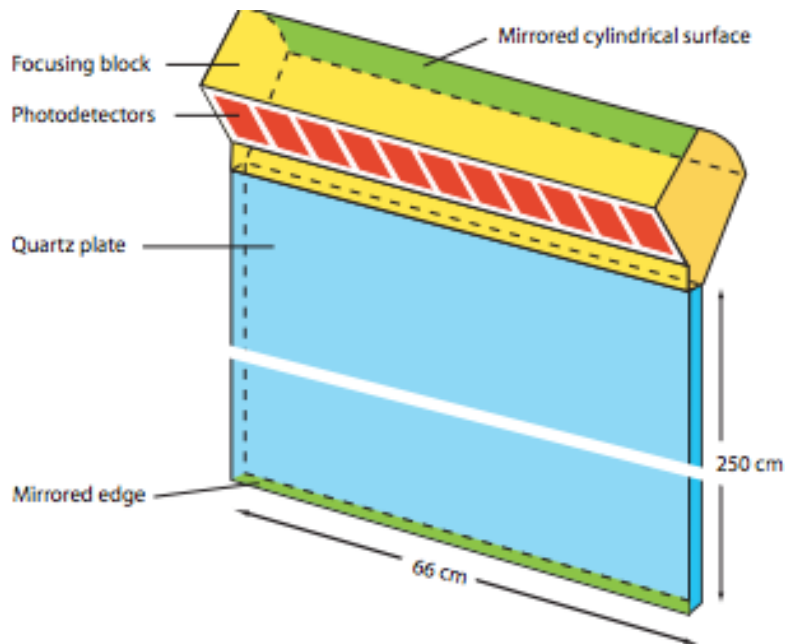


Figure 3.4: Schematic view of the TORCH module.

The ECAL and HCAL will not go through detection technology modifications. The key elements of the upgrade of the calorimeters are the redesign of the readout electronics, to be able to operate at a 40 MHz rate, the reduced gains in PMTs, to ensure longer lifetimes at high luminosity, and the removal of the SPD/PS systems, since their purpose is basically linked to the L0. Measurements and simulated studies have shown that the detectors functionality won't be affected by the extra radiation

dose in general, at least until the following long shutdown (LS3).

Finally, the main modifications on the Muon chambers for the upgrade are the removal of the M1 station, since with higher luminosities it would be extremely difficult to associate hits at M1 with muon tracks segments on the other stations and its current function is mostly used in the L0 trigger, the redesign of readout electronics, to be able to operate at a 40 Mhz rate, and the installation of additional shielding before M2, in order to reduce the contamination due to hadrons.

3.3 Trigger

One of the most important features of the LHCb upgrade is the removal of the L0 trigger level [31]. The upgrade trigger goes to an all-software structure (fig. 3.5), providing flexibility to the selection strategies, in particular allowing more efficient triggering on low momentum tracks. Limits on processing power and bandwidth are the main challenges to be overcome.

The upgrade trigger is composed by a few distinct levels. The Low Level Trigger (LLT) is a software version of the L0, which applies cuts based on the p_T of hadrons, electrons, photons or muons. Current studies show that the LLT is not necessary, since the following stages would be able to read the full data rate, but it will be developed in case the LHC conditions change. After LLT, or as a first stage if the LLT is not implemented, tracks are reconstructed with precision similar to the offline reconstruction and selection criteria are applied, reducing the data rate. Finally, the available processing power is enough to apply Kalman filter based track fits, for RICH algorithms provide particle identification and for a full reconstruction selection to be applied to the remaining events. The data rate is, then, reduced to a rate which can be processed offline, between 20 and 100 kHz .

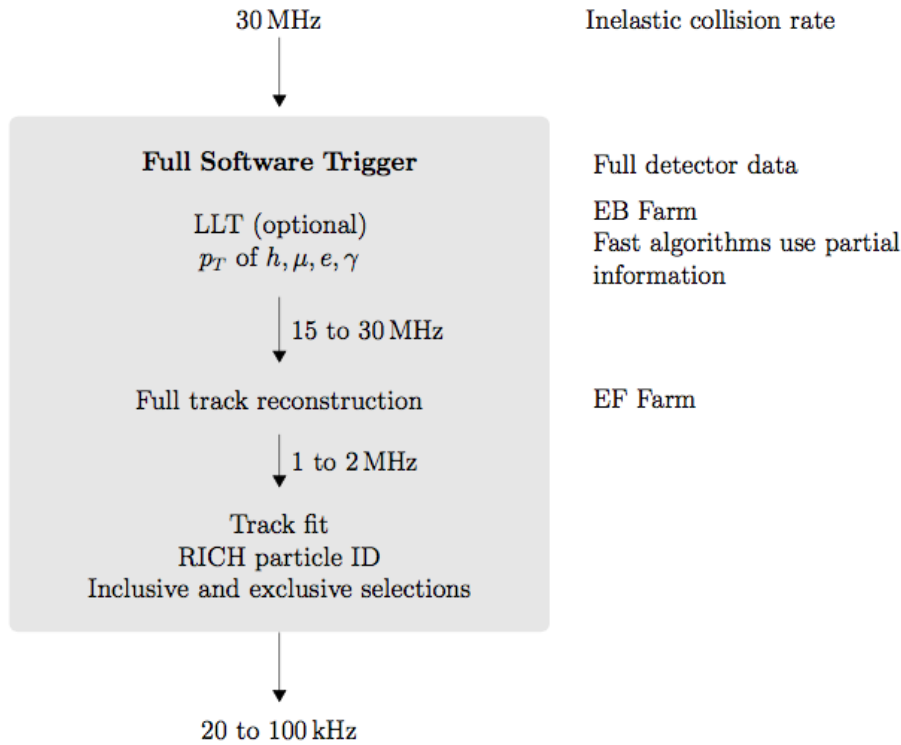


Figure 3.5: Upgrade trigger scheme.

3.4 VELO Upgrade - VeloPix

Several requirements have to be taken into account for the VELO upgrade design in order to operate with the best possible performance [6]. The radiation flux for the VELO under the higher luminosity regime is higher than the current conditions and, therefore, the new detector must be more radiation damage resistant. The expected integrated flux is up to $\approx 8 \times 10^{15}$ neq/cm².

The readout electronics must also improve in order to be able to handle the higher data rate. The huge data flux, combined with the radiation conditions mentioned above, cause an increase on the amount of heat produced and, therefore, on heat dispersion requirements.

The impact parameter (IP), a signature observable of B and D meson decays, must be optimal, not only for analysis purposes, but it will also play a vital role on

the trigger system. The IP resolution is given by the following expression:

$$\sigma_{IP}^2 = \frac{r_1^2}{p_T^2} \left[0.0136 \text{ GeV}/c \sqrt{\frac{x}{X_0}} \left(1 + 0.038 \ln \frac{x}{X_0} \right) \right]^2 + \frac{\Delta_{02}^2 \sigma_1^2 + \Delta_{01}^2 \sigma_2^2}{\Delta_{12}^2} \quad (3.1)$$

where r_1 is the radius of the first hit of the particle track, p_T is the transverse momentum of the particle, x/X_0 is the fractional radiation length before the second measured point, σ_1 and σ_2 are the spacial uncertainties on the first and second hits, respectively and Δ_{ij} is the distance between points i and j , where 0 stands for the vertex, 1 is the first hit and 2 is the second hit. Equation 3.1 shows that the IP resolution depends basically on the distance between the first measured points to the vertex, in particular the radial distance r_1 , and the amount of material traversed by the particle before the first hits, where the largest material contribution comes from the RF foil. These parameters must be taken into account to obtain an optimal performance.

In order to be able to operate under the upgrade conditions the chosen technology for the upgrade VELO detector is of hybrid pixel modules, with new sensors called VeloPix [6], which are more radiation resistant, have less probability of reconstructing ghost tracks and handle better the higher data flux. The new module contains four sensors, two on each half-module, forming a “L” shape, as shown in figure 3.6. Each sensor is composed by three readout chips and each chip features a matrix of 256x256 silicon square pixels with 55 μm sides.

Two distinct approaches were considered for the detector cooling system, both using CO₂: with titanium tubes on a graphite based foam, called POCOFoam, or with microchannels on a silicon substrate. The chosen alternative was the microchannels (fig. 3.6), since they present a smaller material contribution and in this case the cooling substrate is directly in touch with the heat source. For more information on the microchannel CO₂ cooling for the VELO upgrade see [32].

With respect to the detector geometry, in order to achieve the best IP resolution

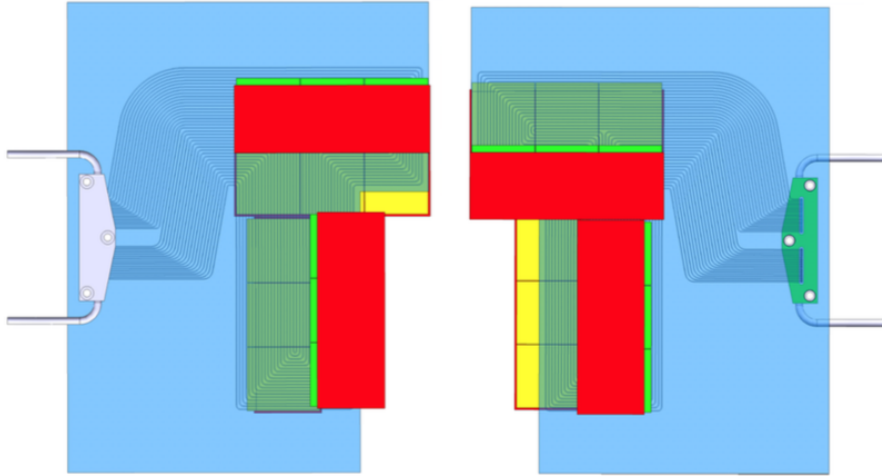


Figure 3.6: Front and rear view of the upgraded VELO module. Sensors are shown in red and the microchannel cooling substrate in blue.

the detector must be placed as close to the interaction region as possible. This means to reduce the distance between the RF foil and the beam, as well. Considering the LHC requirements, the proposed inner radius for the foil is 3.5 mm. This places the detector 5 mm away from the beam at its closest point. Also, the number and position of modules have been optimized as well (fig. 3.7). The IP resolution for the upgraded VELO compared with the current one can be seen in figure 3.10.

The RF foil design must also be studied in order to obtain the smallest possible material contribution. Simulation studies aiming to improve the RF foil performance were performed as part of this thesis. The upgrade design for the foil follows basically the same strategy, but adapted to the upgrade VELO geometry (fig. 3.8). The proposed RF-shield has a “step function” shape, following the edge of the “L” shaped module. It is made of aluminium, the same material as the current foil, but with uniform thickness of $250 \mu m$. The upgrade foil also has the largest material contribution, specially before the first and second hits, as shown in figure 3.9. The impact of the RF foil on the IP resolution can be seen in figure 3.11. The slope seen on the IP resolution decreases linearly with the foil thickness.

Improvements on the RF foil design would be of great interest, since it has

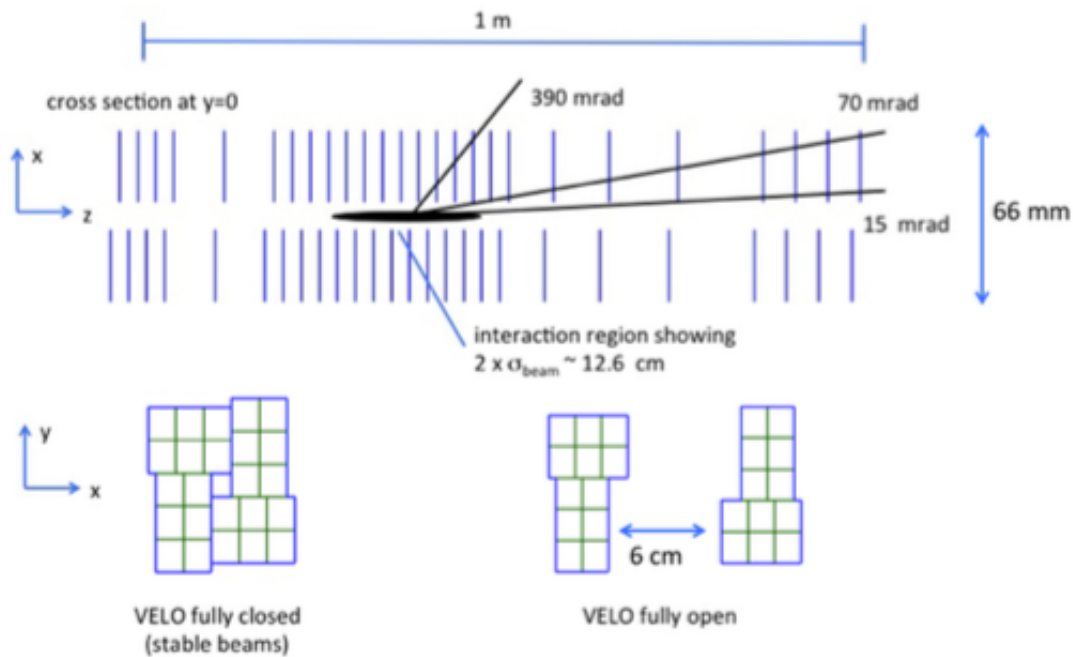


Figure 3.7: Schematic view of the upgraded VELO.

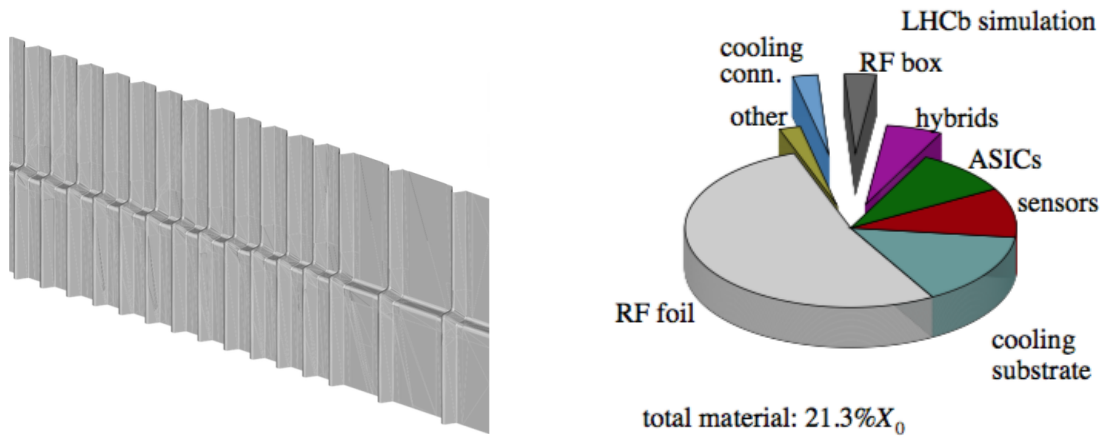


Figure 3.8: RF foil design for the VELO upgrade.

Figure 3.9: Material contributions for the upgraded VELO.

a major impact over the IP resolution. Chemical etching techniques are under development and the possibility of thinning specific regions of the foil provide a number of alternative designs. Tests with different thicknesses on the region close to the beam, performed as part of this thesis, show that these techniques can bring an excellent improvement on the IP resolution, as shown in figure 3.12. A public

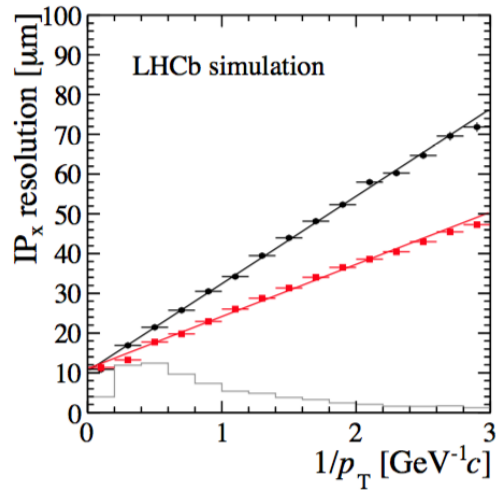


Figure 3.10: IP resolution for the current VELO in black and the upgraded VELO in red. In light gray we see the relative population of b-hadron daughters in each bin.

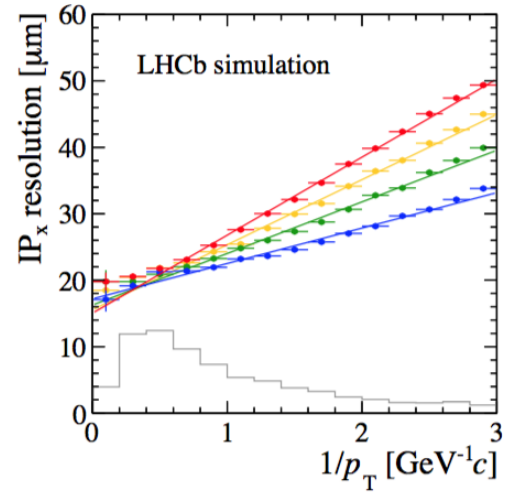


Figure 3.11: IP resolution with different foil thickness configurations. In red the nominal thickness of 250 μm is used, while in orange we have 167 μm, in green, 83 μm and no foil in blue (0 thickness). In light gray the relative population of b-hadron daughters is shown.

note, which went through reviews from internal referees, was written describing the full simulation study. The public note is attached to this thesis, in appendix A.

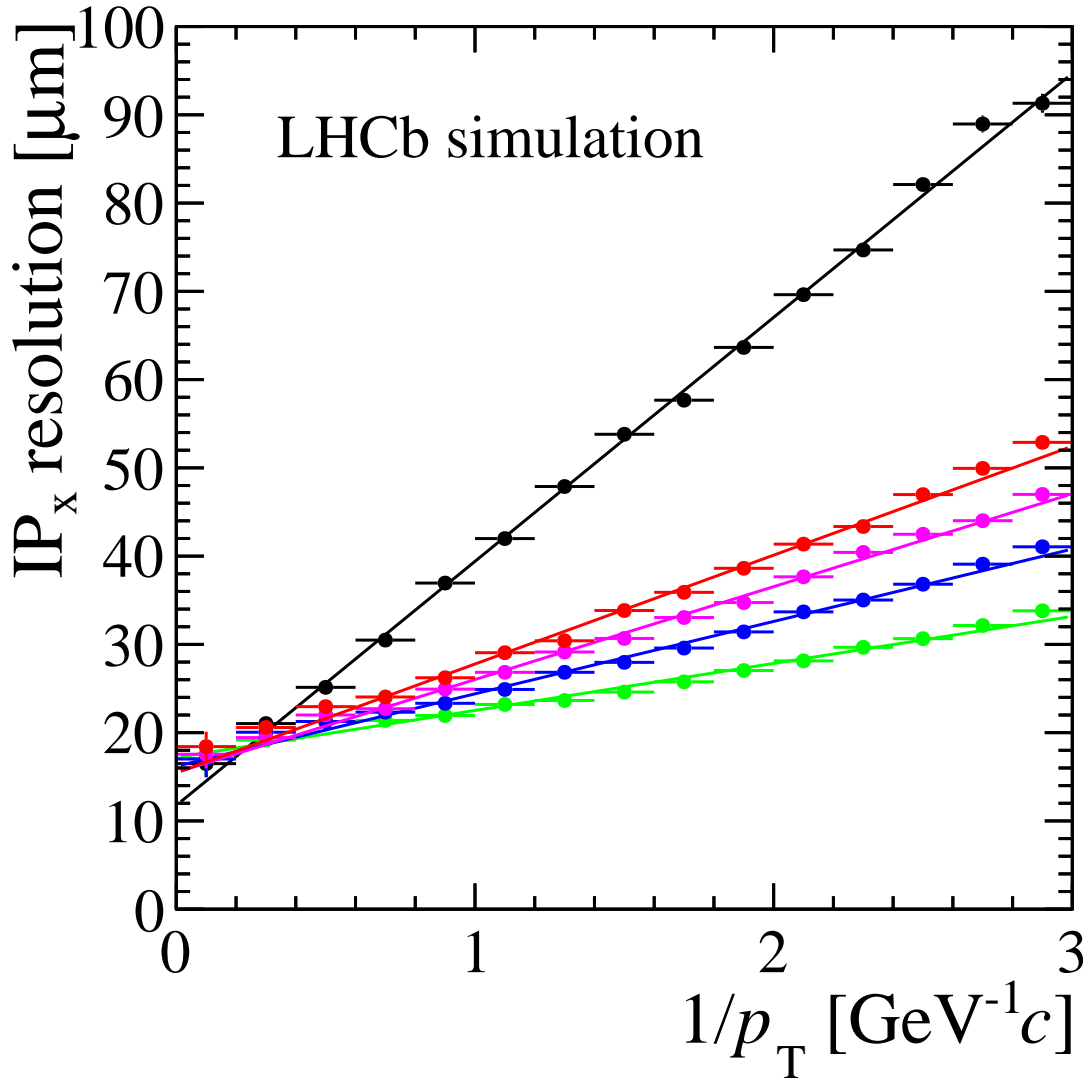


Figure 3.12: IP resolution for partially thinned RF foil with different thicknesses on the region around the beam, compared to the current VELO. In black, the IP resolution for the current VELO is shown. In red, magenta and blue are shown the upgraded VELO IP resolution for RF foils with inner thickness of 300 μm , 200 μm and 100 μm , respectively. In green, the configuration without RF foil is shown.

Chapter 4

The $D^+ \rightarrow K^- K^+ \pi^+$ Decay

Large samples of $D_{(s)}^+$ mesons were acquired during the first years of LHCb operation. This enables several studies related to the charm sector. In particular hadron spectroscopy is one of the main topics within the LHCb charm physics program. The analysis of 3-body decays of the $D_{(s)}^+$ meson offer unique opportunities for meson spectroscopy studies.

The motivation for these studies is twofold: the analysis of the resonant component of the decay brings information about the decay mechanisms, which is a complex interplay between weak and strong interactions; the understanding of the strong phases, in particular those from S-wave amplitudes, is crucial for CPV measurements that use hadronic decays.

The $D^+ \rightarrow K^- K^+ \pi^+$ decay is Cabibbo suppressed and can proceed mainly via two distinct tree level diagrams, to $(K^- \pi^+) K^+$ and $(K^- K^+) \pi^+$ quasi two-body states, shown in figures 4.1 and 4.2.

Resonances in the $K\pi$ systems arise from diagrams as the one presented in figure 4.1. These may include resonant states of the K^* family. Resonant states with $u\bar{u} + d\bar{d}$ components in the KK system can also be formed through his diagram. The annihilation diagram in figure 4.3 could also contribute for this process, but it is highly suppressed.

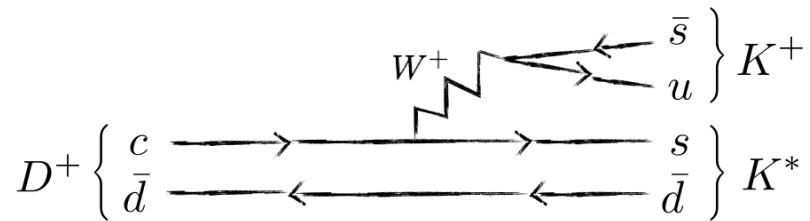


Figure 4.1: Decay diagram of the type $D^+ \rightarrow R(\rightarrow K^- \pi^+) K^+$.

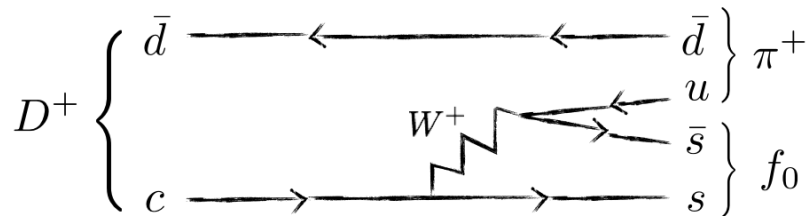


Figure 4.2: Decay diagram of the type $D^+ \rightarrow R(\rightarrow K^- K^+) \pi^+$.

Diagram 4.2, on the other hand, show an example of a $D^+ \rightarrow K^- K^+ \pi^+$ decay with a resonance in the KK system. This is a color suppressed diagram, since quark pair arising from the W^+ must match the color of the others. Contributions from

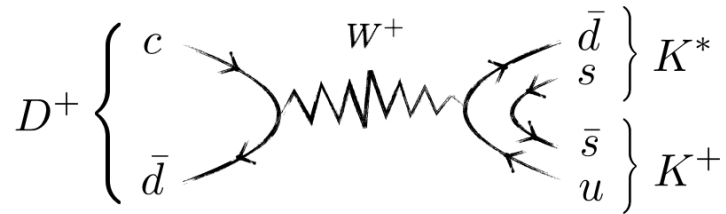


Figure 4.3: Annihilation decay diagram of the type $D^+ \rightarrow R(\rightarrow K^-\pi^+)\pi^+$.

resonances such as the $\phi(1020)$ and the f_0 family are expected. The $a_0(1450)$ and $a_2(1320)$ resonances have isospin 1 and, since the $s\bar{s}$ pair has isospin 0, it is a highly suppressed contribution.

The analysis of very large data samples is extremely challenging. Determining the resonant structure of this decay requires an accurate model to precisely describe the underlying physics. The most common approach to describe the dynamics in the Dalitz plot is the isobar model, that has known limitations. The Breit-Wigner (BW) formulation, widely used for this type of analysis, is an approximation for narrow, isolated resonances, which is often not the case for S-wave resonances. The K-Matrix formalism is an alternative approach to describe the S-wave, but it neglects re-scattering effects.

The Model Independent Partial Wave Analysis can be used to describe the S-wave amplitude without making any assumptions regarding its dynamics. This method, developed by the E791 collaboration [51], represents the S-wave contribution as a single complex function $\mathcal{A}_S = a(s_{ij})e^{i\delta(s_{ij})}$, where s_{ij} is the squared invariant mass of particles i and j , where i and j can be the two particles of either of the resonant

systems, $K^-\pi^+$ or K^-K^+ . The P- and D-waves are described by the regular isobar model.

Final State Interactions (FSI) provide an important ingredient to the decay dynamics. Studies of the composition the $K^-\pi^+$ and $\pi^-\pi^+$ systems S-waves using the MIPWA show discrepancies between measured phases in D meson decays and in scattering experiments, indicating the impact of this kind of interaction [52–55]. The MIPWA does not explicitly describes the FSI interaction, but the FSI phases are implicitly incorporated in the MIPWA parameters.

Under this context, the comparison between the D^+ and D_s^+ S-waves is particularly interesting. The FSI has a smooth dependance on the mass and, therefore, should present similar behaviors in both decays. The subtraction of the MIPWA phases from D^+ and D_s^+ provide information on the weak interaction.

Previous analysis done by the CLEO [56] and BaBar [57] collaborations, although mainly focused in searches for CP violation, included Dalitz plot analyses for the $D^+ \rightarrow K^-K^+\pi^+$ decay. Both analyses presented fits with unsatisfactory p-values (2.05×10^{-6} for CLEO and 4.37×10^{-11} for BaBar). LHCb provides a much larger sample, in which an extremely accurate description will be needed in order to fit the data, making this analysis very challenging.

In Figure 4.4 we show the Dalitz plot for the $D^+ \rightarrow K^-K^+\pi^+$ decay with LHCb 2012 data, with 2 fb^{-1} . The $\phi(1020) + \pi$ channel peaks clearly in the low KK region, the $\kappa + K$ populates the low $K\pi$ mass region, the $K^{*0}(892) + K$ can be seen in around the $s_{23} = 0.8 \text{ MeV}^2/c^4$ region and the $K^{*0}(1430)$ arises less clearly in the high $K\pi$ mass region. Both CLEO and BaBar analyses include these resonances as the main contributions. On the other hand, the S-wave introduces a series of resonant channels, and individual contributions are not well measured. Considering that these resonances are broad, overlapping and interfering with each other, using the Breit-Wigner formulation for them is problematic. The MIPWA method is able to provide us with better results, even though it still does not take into account

three-body interactions and the interpretation of such results would require further investigation.

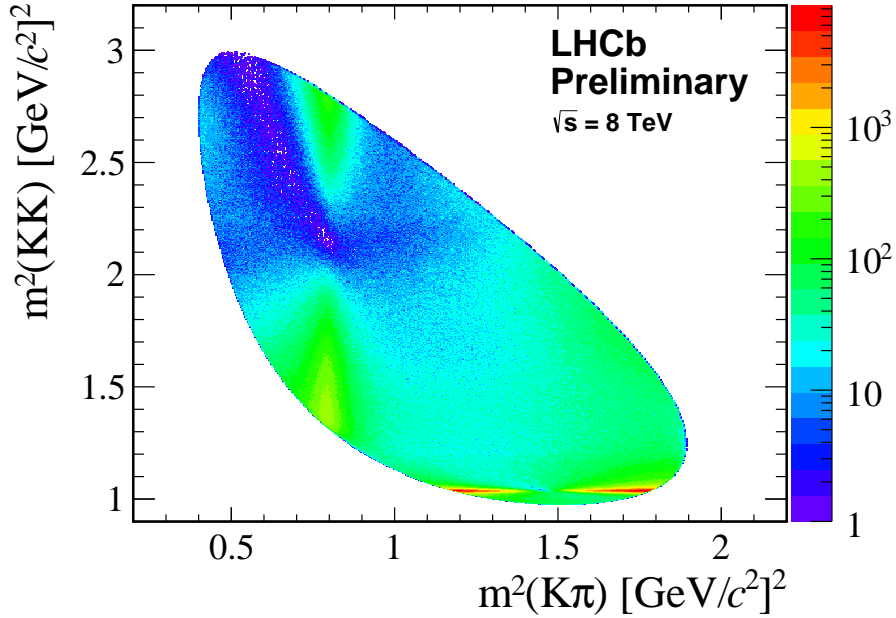


Figure 4.4: Dalitz plot of the $D^+ \rightarrow K^- K^+ \pi^+$ decay with LHCb 2012 data.

Another challenging aspect of this analysis is that it presents S-waves in both KK and $K\pi$ axis. Since a flat distribution could be fitted as part of both S-waves, providing a infinite number of solutions to the fit, it's not possible to use the PWA approach for both simultaneously using the method we have implemented so far. We choose to use it for the KK axis, which is less studied and may present important information on the dynamics of this system [48], which is dominant on the $D_s^+ \rightarrow K^- K^+ \pi^+$. The MIPWA is not performed in this thesis, but all aspects related to it are presented. We present results using the regular isobar model, in which the S-wave is represented as a sum of BW components. The next step is to use these results as input to the PWA fits.

Chapter 5

Amplitude Analysis Formalism

Three-body hadronic decays are dominated by resonant channels and, in order to unveil the dynamics behind them, we must conceive an amplitude analysis. The Dalitz plot is an important tool in this process, given that it provides us the phase space distribution of the decay. With the Dalitz plot distribution in hand, we can compare it with different models in order to interpret it.

In this chapter we describe the basics of Dalitz plots and its characteristics. Afterwards, we explain the most used approach for this kind of analysis, the Isobar Model. Later, we talk about a more accurate alternative to the Isobar Model, the Partial Wave Analysis (PWA). Finally, we discuss the aspects and challenges related to this type of analysis and more specifically to the $D^+ \rightarrow K^- K^+ \pi^+$ decay.

5.1 Dalitz Plot

Considering a three-body decay $D \rightarrow P_1 + P_2 + P_3$ ¹, the combination of linear momenta in the final state provides us a nine-dimensional momentum space. Taking

¹In this thesis we use as a standard for the $D^+ \rightarrow K^- K^+ \pi^+$ decay P_1 for the K^- , P_2 for the K^+ and P_3 for the π^+ , unless otherwise specified.

into account the conservation of the 4-momenta:

$$E_D = \sum_{i=1}^{i=3} E_{P_i} \quad (5.1)$$

$$\vec{p}_D = \sum_{i=1}^{i=3} \vec{p}_{P_i} \quad (5.2)$$

where $E_{D(P_i)}$ is the energy of the particle D (P_i) and $\vec{p}_{D(P_i)}$ is their corresponding 3-momenta, the phase space is reduced by four degrees of freedom. In addition, a decay where both the mother and the final state particles have no spin would be invariant under rotations of the full system and, therefore, allow the integration over the three rotation angles. Under these circumstances we have only two degrees of freedom left. Thus, the resulting 2-dimensional phase space contains the physically allowed region of the momentum space and its limits are established by the kinematical constraints of the decay.

In order to study the decay dynamics, a first step is to understand the phase space properties and characteristics. The next definitions and conclusions follow the path given in [33]. Defining the squared invariant masses:

$$s \equiv M_D^2 \quad (5.3a)$$

$$s_{12} \equiv m_{12}^2 = (p_1 + p_2)^2 \quad (5.3b)$$

$$s_{23} \equiv m_{23}^2 = (p_2 + p_3)^2 \quad (5.3c)$$

$$s_{31} \equiv m_{31}^2 = (p_3 + p_1)^2 \quad (5.3d)$$

where p_i is the 4-momentum of the particle i , and introducing the kinematical

function:

$$\lambda(x, y, z) \equiv (x - y - z)^2 - 4xy \quad (5.4)$$

we can derive the energies and 3-momenta in the rest frame of the 1-2 system of the decaying particle (R_{12}), where $p_1 + p_2 = (\sqrt{s_{12}}, 0)$:

$$E_1^{R_{12}} = \frac{s_{12} + m_1^2 - m_2^2}{2\sqrt{s_{12}}} \quad (5.5a)$$

$$E_2^{R_{12}} = \frac{s_{12} + m_2^2 - m_1^2}{2\sqrt{s_{12}}} \quad (5.5b)$$

$$E_3^{R_{12}} = \frac{s - s_{12} - m_3^2}{2\sqrt{s_{12}}} \quad (5.5c)$$

$$E^{R_{12}} = \frac{s + s_{12} - m_3^2}{2\sqrt{s_{12}}} \quad (5.5d)$$

$$P_1^{R_{12}} = P_2^{R_{12}} = \frac{\lambda^{1/2}(s_{12}, m_1^2, m_2^2)}{2\sqrt{s_{12}}} \quad (5.5e)$$

$$P_3^{R_{12}} = P^{R_{12}} = \frac{\lambda^{1/2}(s_{12}, m_1^2, m_2^2)}{2\sqrt{s_{12}}} \quad (5.5f)$$

Therefore, expanding 5.3 with 5.5 in hands, we have, for particles 1 and 3, for example:

$$s_{31} = p_3^2 + 2p_3p_1 + p_1^2 = m_3^2 + m_1^2 + 2E_3^{R_{12}} E_1^{R_{12}} + 2P_3^{R_{12}} P_1^{R_{12}} \cos \theta_{31}^{R_{12}} \quad (5.6)$$

where θ_{23}^{CM} is the angle between the 3-momenta of particles 1 and 3 on the R_{12} rest

frame. Isolating, then, $\cos \theta_{31}^{R_{12}}$:

$$\cos \theta_{31}^{R_{12}} = \frac{m_3^2 + m_1^2 + 2E_3^{R_{12}} E_1^{R_{12}} - s_{31}}{2P_3^{R_{12}} P_1^{R_{12}}} \quad (5.7)$$

$$= \frac{2s_{12}(m_3^2 + m_1^2 - s_{31}) + (s_{12} + m_1^2 - m_2^2)(s - s_{12}^2 - m_3^2)}{\lambda^{1/2}(s_{12}, m_1^2, m_2^2)\lambda^{1/2}(s, s_{12}, m_3^2)} \quad (5.8)$$

This result can be extended to other rest frames in similar fashion producing equivalent results.

For a given value of s_{12} , the maximum and minimum values of s_{31} will be those where particles 1 and 3 are antiparallel or parallel to each other, respectively. We can write those limits as:

$$s_{31_{max/min}} = \frac{1}{2s_{12}}(s_{12} + m_1^2 - m_2^2)(s - s_{12}^2 - m_3^2) + m_1^2 + m_3^2 \pm \lambda^{1/2}(s, m_1^2, s_{23})\lambda^{1/2}(s_{23}, m_2^2, m_3^2) \quad (5.9)$$

This provides a contour of the physical region where the decays can happen.

The Dalitz plot [34] is the biunivocal representation of the phase space through 2 out of the 3 invariant masses, or any linear combination of them with constant Jacobian, which arises from the pairing of the final state particles (Figure 5.1). It is limited within the range imposed by equation 5.9. In this thesis we are going to use as a standard the Dalitz plot as a function of s_{12} and s_{31} , since those are the axis where resonances may occur.

The partial decay rate for a decay of a particle with mass M , energy E and 3-momentum \mathbf{P} into N particles, as defined in [38], can be written as:

$$d\Gamma = \frac{(2\pi)^4}{2M} |\mathcal{M}|^2 \delta^3 \left(\mathbf{P} - \sum_{i=1}^{i=N} \mathbf{P}_i \right) \delta \left(E - \sum_{i=1}^{i=N} E_i \right) \prod_{i=1}^{i=N} \frac{d^3 \mathbf{P}_i}{(2\pi)^3 2E_i} \quad (5.10)$$

where \mathcal{M} is the Lorentz invariant amplitude matrix element. In our case, of a D

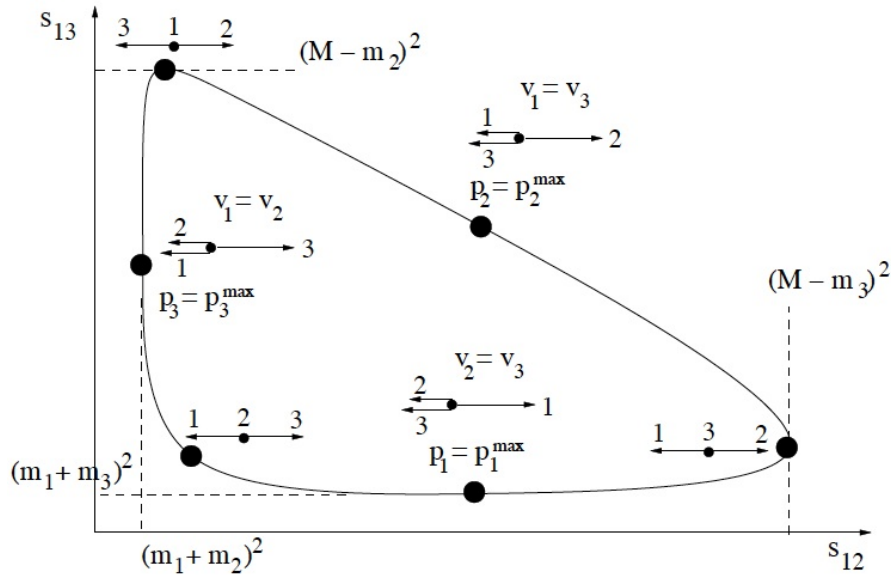


Figure 5.1: Dalitz plot boundary and distinct final state momentum configurations that occur in each region of the (s_{12}, s_{31}) plane. In the extremities we have the configuration in which one of the final state particles is at rest, while in the intermediate regions we see the events were one of the particles have maximum momentum.

meson decaying into three pseudoscalar particles, this rate is given by:

$$d\Gamma = \frac{1}{(2\pi)^5} \frac{1}{16M} |\mathcal{M}_D|^2 \delta^3 \left(\mathbf{P}_D - \sum_{i=1}^{i=N} \mathbf{P}_i \right) \delta \left(E_D - \sum_{i=1}^{i=N} E_i \right) \frac{d^3\mathbf{P}_1 d^3\mathbf{P}_2 d^3\mathbf{P}_3}{E_1 E_2 E_3} \quad (5.11)$$

It can be shown, as demonstrated in [33], [36] and [37], that the phase space element:

$$dQ = \delta^3 \left(\mathbf{P}_D - \sum_{i=1}^{i=N} \mathbf{P}_i \right) \delta \left(E_D - \sum_{i=1}^{i=N} E_i \right) \frac{d^3\mathbf{P}_1 d^3\mathbf{P}_2 d^3\mathbf{P}_3}{E_1 E_2 E_3} \quad (5.12)$$

can be integrated, using equations 5.5, over the delta functions and the spatial orientation, resulting in a constant density across the Dalitz plot:

$$\frac{dQ}{ds_{12} ds_{31}} = \frac{2\pi^2}{M_D^2} \quad (5.13)$$

This is a very important property of the Dalitz plot. Equation 5.13 shows us that the phase space distribution is constant and, therefore, if the Lorentz invariant amplitude is also constant, then the Dalitz plot distribution will be flat. As a consequence,

any non-uniformities across the phase space are signatures of the underlying decay dynamics.

5.2 Isobar Model

The $D^+ \rightarrow K^- K^+ \pi^+$ decay is dominated by resonant channels where the D^+ decays into two particles, one being unstable and quickly decaying into two more, as shown on Figure 5.2. If we call this unstable state R , then the transition is of the type:

$$\begin{aligned} D^+ &\rightarrow R + P_c \\ R &\rightarrow P_a + P_b \end{aligned} \tag{5.14}$$

Hereafter we use as a standard, when discussing a generic resonance, P_a and P_b for the particles that come from it and P_c for the remaining one, unless otherwise specified. Resonances form structures on the phase space distribution due to their properties and the interference of their amplitudes, but, unfortunately, it is not possible to describe them from first principles. The most common approach to provide an interpretation to the Dalitz plot is the Isobar Model [38]. In this model the amplitude is given as the coherent sum of complex amplitudes, each one representing the contribution of a resonant channel, in addition to a non-resonant component:

$$\mathcal{A}(s_{12}, s_{31}) = C_{NR} \mathcal{M}_{NR}(s_{12}, s_{31}) + \sum_r C_r \mathcal{M}_r(s_{12}, s_{31}) \tag{5.15}$$

where C_r are empirical complex parameters that give the relative contribution of each component, considering one resonant channel is always used as reference and its corresponding coefficient is set to one. The interference between each component is also tuned by the complex factors C_r . Finally, $\mathcal{M}_{r(NR)}(s_{12}, s_{31})$ are complex phenomenological functions that approximately describe the component dynamics.

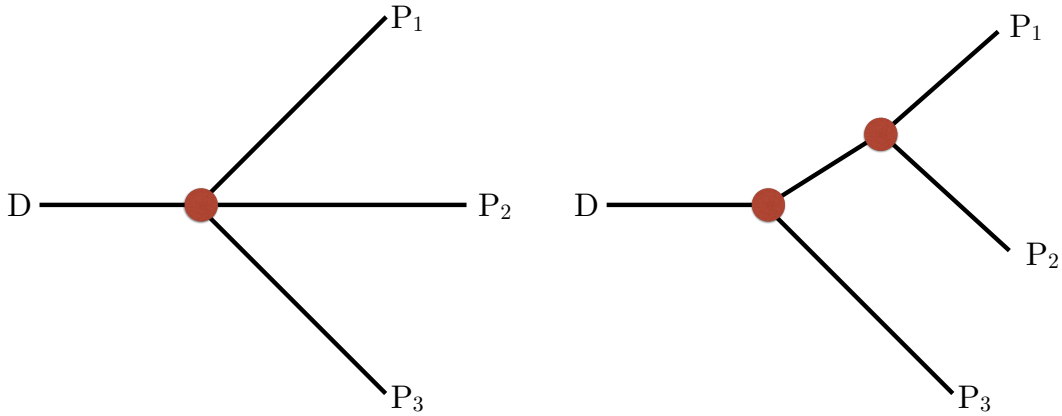


Figure 5.2: A non-resonant (left) and a resonant (right) decay.

The functions $\mathcal{M}_r(s_{12}, s_{31})$ are phenomenological objects that take into account general principles, such as the Lorentz invariance, the conservation of angular momentum and the size of interaction vertices. They may include form factors, mass and angular distribution functions. It can be typically be written as a composition of these elements:

$$\mathcal{M}_r(s_{12}, s_{31}) = F_D(s_{12}, s_{31})F_r(s_{12}, s_{31})M_r(s_{12}, s_{31})\Theta(s_{12}, s_{31}) \quad (5.16)$$

Where, F_D and F_r are the form factors for the D and the resonance decay, respectively, M_r is a dynamical function that describes 2-body invariant the mass distribution and Θ is the angular distribution. Each of these elements may have different formulations.

The Blatt-Weisskopf form factors [39] are functions that represent the spin and momentum dependence, suppressing states with higher angular momenta when in the region close to the threshold. If we consider a decay as shown in equation 5.14, where q is the momentum of particles a and b in the center of mass rest frame of the resonance R, q_0 is their momentum when $s_{ab} = m_R^2$, L is the orbital angular momenta of the R daughters, which is equal to the spin of R and d is a free parameter related to the meson radius, we can define $z \equiv (qd)^2$ and $z_0 \equiv (q_0d)^2$ and write the form factors, with two different formulations, as given in table 5.1. In the first, $B_L = 1$

when $z = 1$, while in the second, $B'_L = 1$ when $z = z_0$. For a 3-body decay, two

L	B_L	B'_L
0	1	1
1	$\sqrt{\frac{2z}{1+z}}$	$\sqrt{\frac{1+z_0}{1+z}}$
2	$\sqrt{\frac{13z^2}{1+z}}$	$\sqrt{\frac{(z_0-3)^2+9z_0}{(z-3)^2+9z}}$

Table 5.1: Blatt-Weisskopf form factors for angular momentum $L = 0, 1, 2$ with two distinct formulations.

form factors must be used, one for each step on the decay shown in the decay chain 5.14.

Although the analysis involve spinless particles in both initial and final states, the intermediate states may have spin. As a consequence of the angular momentum conservation, the transition probability will reflect on a non-uniform angular distribution. Using the Zemach formalism described in [40] we can describe the angular distribution \mathcal{A} as a function of the spin and momenta:

$$\mathcal{A} = (-2|p_a||p_c|)^J P_J(\cos \theta_{ac}) \quad (5.17)$$

where P_J is the Legendre polynomial and θ_{ac} is the angle between the trajectory of one of the particles that come from the resonance and the trajectory of the bachelor, with $\cos \theta_{ac}$ being calculated as in 5.8. This function is Lorentz invariant and, therefore, its result is valid for all rest frames. This term typically introduces zeros in the Dalitz plot across resonance region, for non-zero spin states.

The Breit-Wigner parametrization [41] was created to describe resonant transitions in capture of slow neutrons. It is an approximation that assumes a narrow, isolated resonance. The relativistic formulation of the Breit-Wigner can be written as:

$$BW(s_{ab}) = \frac{1}{m_R^2 - s_{ab} - im_r \Gamma(s_{ab})} \quad (5.18)$$

where m_R is the mass of the resonance and $\Gamma(s_{ab})$ is the mass-dependent width:

$$\Gamma(s_{ab}) = \Gamma_R \left(\frac{q}{q_0} \right)^{2L+1} \frac{m_R}{\sqrt{s_{ab}}} \left(\frac{B_L(z)}{B_L(z_0)} \right)^2 \quad (5.19)$$

where Γ_R is the resonance width.

Given that the Breit-Wigner formulation is an approximation, it better describes narrow, isolated resonances. This is hardly the case, since D decays often contain many overlapping broad resonances.

In the case where the resonance is close to a opening threshold, distortions may arise from the contribution of coupled channels. The Flatté formulation [42] is commonly used in this case. It is given by:

$$\mathcal{F}(s_{ab}) = \frac{1}{m_R^2 - s_{ab} - im_R(\rho_{\pi\pi}g_1^2 + \rho_{KK}g_2^2)} \quad (5.20)$$

where g_1 and g_2 are dimensionless coupling constants, with the KK and $\pi\pi$ channels, and such that $g_1^2 + g_2^2 = m_R\Gamma_R$ and $\rho_{\pi\pi}$ and ρ_{KK} are phase space terms, in which depend on the masses of the decay particles. In the f_0 case in the $D^+ \rightarrow K^-K^+\pi^+$ decay, for example, they are given by:

$$\begin{aligned} \rho_{\pi\pi} &= \sqrt{\left(\frac{s_{KK}}{4} - m_\pi^2\right)} + \sqrt{\left(\frac{s_{KK}}{4} - m_{\pi^0}^2\right)} \\ \rho_{KK} &= \sqrt{\left(\frac{s_{KK}}{4} - m_K^2\right)} + \sqrt{\left(\frac{s_{KK}}{4} - m_{K^0}^2\right)} \end{aligned} \quad (5.21)$$

Other formulations have been developed to describe the S-wave resonances, typically broad overlapping, for which Breit-Wigner formulation is a poor approximation. The K-matrix [44] formalism which assumes that the resonant system does not interact with the remaining particle, and the LASS formalism [45], which describes the $K_0^*(1430)$ interference with a slowly varying contribution, are common empirical approaches, but none give an adequate description.

5.3 Partial Wave Analysis

An alternative approach for the amplitude analysis model is the Partial Wave Analysis (PWA). In this model, the S-wave is represented as a generic complex function, to be extracted directly from the data, without making any assumptions with respect to the S-wave composition. Since the Breit-Wigner formulation has limitations when dealing with broad, overlapping resonances and the S-wave components are mostly within this profile, this method can give us better results.

This complex function is given by two cubic spline interpolations, as described in [46], one for the real part and the other for the imaginary part or one for the amplitude and the other for the phase. Given a tabulated function $y_i = y(x_i)$, $i = 0, \dots, N$, the interpolation formula for it, such that $x_j < x < x_{j+1}$, is:

$$y(x) = A(x)y_j + B(x)y_{j+1} + C(x)y_j'' + D(x)y_{j+1}'' \quad (5.22)$$

where:

$$\begin{aligned} A(x) &\equiv \frac{x_{j+1} - x}{x_{j+1} - x_j} \\ B(x) &\equiv \frac{x - x_j}{x_{j+1} - x_j} \\ C(x) &\equiv \frac{1}{6}[(A^3(x) - A(x))(x_{j+1} - x_j)^2] \\ D(x) &\equiv \frac{1}{6}[(B^3(x) - B(x))(x_{j+1} - x_j)^2] \end{aligned} \quad (5.23)$$

The basic idea is to use as amplitude for the S-wave a tabulated function in which the parameters are the complex numbers at specific points:

$$\mathcal{M}_{S\text{-wave}}(s_{ab_j}) = a_j e^{i\delta_j} \quad (5.24)$$

where the dynamical function only depends on s_{ab} , since the S-wave has zero spin. With this tabulated function in hand we can use the cubic spline interpolation to

calculate either the real and imaginary parts or the amplitude and phase of this function at any point of the s_{ab} axis. In the fit we can set the complex values at each point as free parameters, and achieve a more precise description of the S-wave distribution. A good starting set of values for these parameters is the sum of the amplitudes of the expected S-wave resonances, at each point. The initial set of parameters can come from a preliminary Isobar fit.

Resonances from the P-wave and the D-wave are represented as resonant contributions according to the isobar model. These are an assumption for this method.

5.4 Fit Fraction

Due to the many different parametrizations for each one of the possible formulations, the complex parameters C_r in equation 5.15 are not universal, e.g., two different analysis of the same decay may result in distinct fit parameters, due to distinct normalization methods, but still agree with each other. On the other hand, the rate of each single component and the corresponding phase are directly comparable. The Fit Fraction (FF) is the contribution of a single process in the decay and can be calculated by integrating the amplitude of the given component and dividing by the integral of the full coherent sum of all amplitudes:

$$FF_r = \frac{\int |a_r e^{i\delta_r} \mathcal{M}_r(s_{12}, s_{31})|^2 ds_{12} ds_{31}}{\int |\sum_i a_i e^{i\delta_i} \mathcal{M}_i(s_{12}, s_{31})|^2 ds_{12} ds_{31}} \quad (5.25)$$

The total sum of fit fractions is, in general, different from 100%. Constructive interferences between amplitudes of different contributions decrease the total sum of fit fractions, while destructive interferences raise it.

Chapter 6

Rio+ Package for Dalitz Plot

Analyses

In this chapter we present a description of the Rio+ package. It is based on the well established code used for amplitude analysis by the E791 collaboration. The package was developed for all analyses within the Rio charm group, in a combined effort among the students Josué Molina, Rafael Aoude and me, and it is a crucial part of this thesis.

6.1 Features

The Rio+ package is focused on the amplitude analysis of 3-body hadronic decays of the $D_{(s)}^+$ meson. It is able to simulate and fit the Dalitz plot of decays containing $\pi^-\pi^+$, $K^-\pi^+$ and K^-K^+ resonances, using the isobar model described in 5.2.

The amplitudes for several resonant channels are already implemented in the code and the package was developed in a flexible fashion, allowing the addition of other amplitudes within a few easy steps. The fit parameters are the complex coefficients C_r , as shown in equation 5.15. In order to use the amplitude given in equation 5.15 as a Probability Density Functions (PDF), it is necessary, in general, to normalize it to $\int A(s_{12}, s_{31})ds_{12}ds_{31}$. Masses and widths of each resonance can

also be set as free parameters. The parameters C_r can be given as magnitudes and phases or as real and imaginary parts. Writing those parameters as magnitudes and phases is convenient for the physical interpretation of the results, but makes the fits less stable.

The MIPWA is implemented on the Rio+ as well. The input for the S-wave model is written from a .txt file, providing the points to be interpolated along with the initial values of the complex amplitude in each point, as discussed in 5.3.

The Rio+ also has all necessary infrastructure to include acceptance correction in the model. Background contributions can also be included. Both features are implemented using histograms.

Two fitting methods are available within Rio+: the maximum likelihood or the least squares methods. The maximum likelihood method is the standard approach for this kind of analysis. As a drawback, its processing time increases linearly with the number of events, which is specially complicated when dealing with large samples. The least squares method, on the other hand, depends only on the number of bins. Its drawback is that it requires amplitudes integrals to be calculated for each bin, in order to obtain the PDF average in the corresponding bin, resulting in large processing time for fits in which integrals need to be recalculated.

The calculation of the normalization integrals is particular sensitive when dealing with fits with free masses and widths or using the MIPWA model. In general, it is not necessary to recalculate the normalization integrals every iteration of the minimizer. Since the complex coefficients do not depend on the phase space point, they can be treated as constants. If the fit contain as free parameters only the coefficients C_r , then the integral of the amplitude functions remain the same and only need to be calculated once. On the other hand, if masses and widths are set as free parameters or in the MIPWA model case, the integrals of the amplitude functions depend on the fit parameters, forcing the integrals to be recalculated every iteration of the minimizer. This is extremely relevant with respect to processing power and

computing time.

Integrals are calculated through Gauss Legendre quadratures [46]. This method is in a numerical approach in which the integral is approximately calculated as the weighted sum of function values at specific points. The precision of the method is defined by the number of points used for the calculation and the precision of the calculation of the weights.

6.2 Toy Monte Carlo Generator

The segment of the package responsible for the sample simulation is called ToyMCGenerator. It uses as input a text file with information such as the number of events to be produced, the decay channel, the resonant parameters, etc.

The algorithm begins by reading the text file, saving the information and starting a loop to generate the required number of samples. It calculates the normalization of each background component by integrating it over the full phase space using the Gauss-Legendre quadrature.

Next, the maximum of the signal and background PDFs is calculated in two steps. First, a large number of events is generated and the one with maximum PDF value is stored. Afterwards, this event is given as input to a MINUIT minimization of $-PDF$. Starting from the input event, MINUIT sweeps the phase space, providing the maximum (PDF_{max}) with better precision. The combination of these methods has been found the one which provides the best precision without consuming excessive computing power. The maximum of the PDF is latter used to normalize the PDF function, setting its maximum value to one.

Another loop is initiated to generate the required number of events. Events are produced by generating random points inside the $s_{12_{min}} < s_{12} < s_{12_{max}}$ and $s_{13_{min}} < s_{13} < s_{13_{max}}$ window, keeping those within the Dalitz plot limits. This is implemented by requiring $-1 < \cos \theta_{12} < 1$, with $\cos \theta_{12}$ given by eq. 5.8. A random

number $R_{bkgfraction}$ between 0 and 1 is generated and compared with the background fraction to decide the event type: if it is going to be simulated as background or signal. Another random number R_{PDF} between 0 and 1 is generated to be compared with the PDF/PDF_{max} ratio. This ratio contains the exact PDF shape, but it is normalized to have maximum value one. Events in regions with higher probability will most likely present $R_{PDF} < PDF/PDF_{max}$, while events in low probability regions tend to present $R_{PDF} > PDF/PDF_{max}$. The algorithm stores the events with $R_{PDF} < PDF/PDF_{max}$, reproducing the PDF shape. If the event is ignored, the next one will repeat the current event type in order to preserve the background fraction.

By the end of this process, the stored events have the desired distribution. They are saved in a ROOT ntuple containing the invariants for each event. A simplified fluxogram of the generator algorithm is shown at figure 6.1.

6.3 Maximum Likelihood Fitter

The interface with the maximum likelihood fitter algorithm, called Log Likelihood Fitter, is a text file, similar to the one used for the ToyMCGenerator, but with the addition of the input ntuple name, the limits of each free parameter and booleans to set parameters fix or not. The fitter begins by reading the information on the input file and saving it.

In the next step, it reads ntuple events, storing the invariant masses in vectors. For each event read, the amplitudes of each resonant channel and background component is calculated and also stored in vectors. This way, processing time is saved since amplitudes are not recalculated every iteration of the minimization, only when there are any changes in masses, widths or in the PWA case.

Next, the normalization integrals are calculated, for signal and background, which also not recalculated unless necessary. The integration of the amplitudes

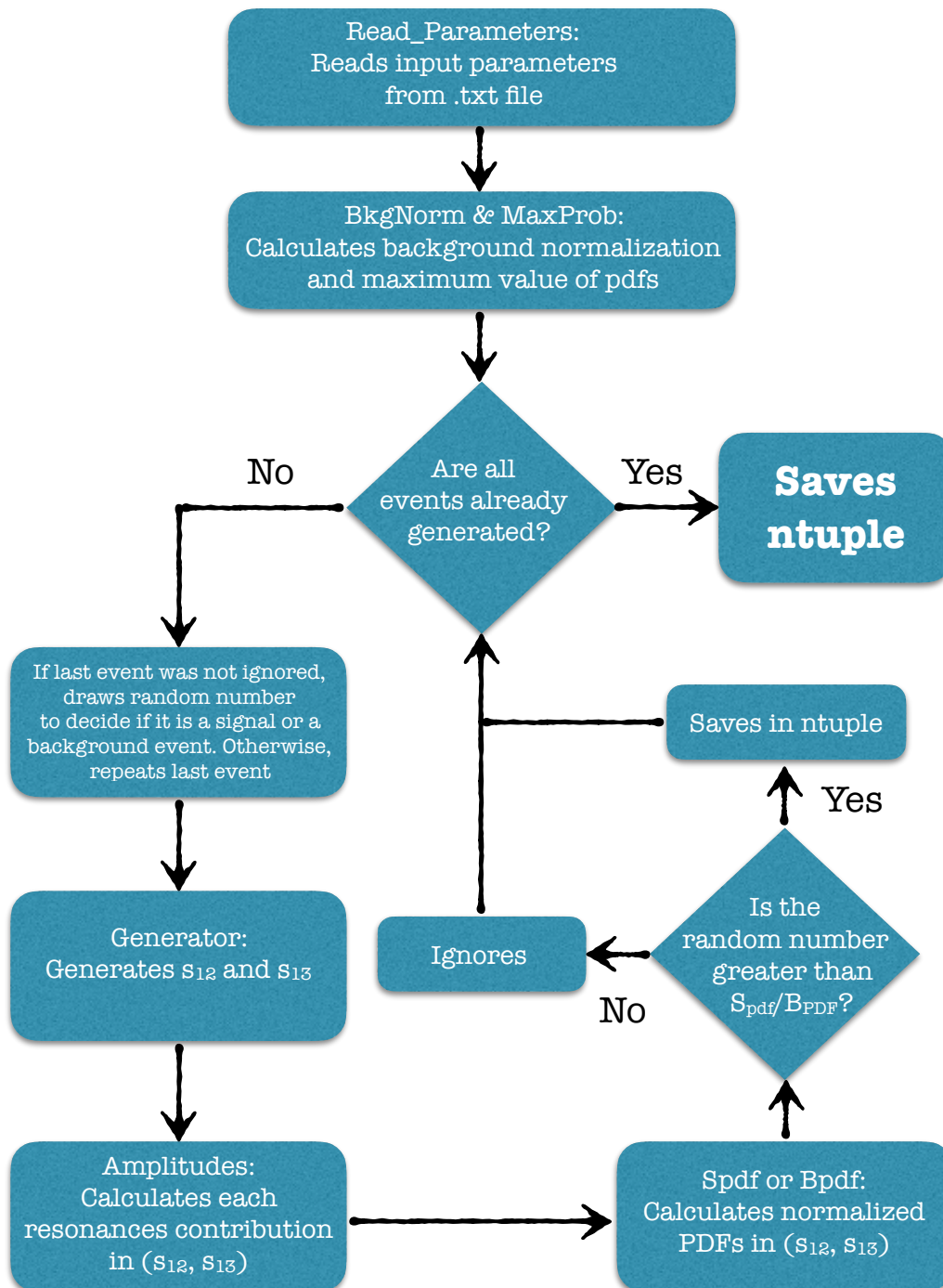


Figure 6.1: Simplified fluxogram of the ToyMCGenerator algorithm.

of signal components are necessary for the fit, opposed to the ToyMCGenerator. The normalization for the signal PDF cancels out in the PDF/PDF_{max} ratio, eliminating the need to calculate it for the generation.

This information is, then, fed into the MINUIT minimizer. Resonant coefficients C_r (together with masses, widths and PWA parameters, if required), are floating parameters, changing values in pairs at each iteration, and the PDF is calculated. The minimizer explores the parameter space until it finds the one that minimizes the the Negative Log Likelihood $-2 \log \mathcal{L}$, where:

$$\mathcal{L}(C_1, C_2, \dots) = \prod_{i=0}^{N_{events}} PDF(s_{12_i}, s_{13_i} | C_1, C_2, \dots) \quad (6.1)$$

Finally, the algorithm prints the best parameter values, the corresponding fit fractions and produces plots of the PDF and resonant contributions. A simplified fluxogram of the Log Likelihood Fitter algorithm can be seen in figure 6.2.

6.4 Least Squares Fitter

The basic principles and workflow of the least squares fitter, called Chi2 Fitter, are similar to the Log Likelihood Fitter. The main difference are that the least squares method is based on a binned comparison. The Dalitz plot is divided into bins, which may or may not be uniform in size, and, for each bin, the model expected content is calculated by integrating each resonant contribution over the given bin. As a result we have a “binned PDF”, which is compared with the binned Dalitz plot every iteration of the minimizer, by calculating the χ^2 , given by:

$$\chi^2 = \sum_{i=0}^{i=n_{bins}} \frac{(N_{PDF_i} - N_{obs_i})^2}{N_{obs_i}} \quad (6.2)$$

where n_{bins} is the number of bins on the Dalitz plot, $(N_{PDF_i} (N_{obs_i}))$ is the “binned PDF” (observed) content of the i^{th} bin.

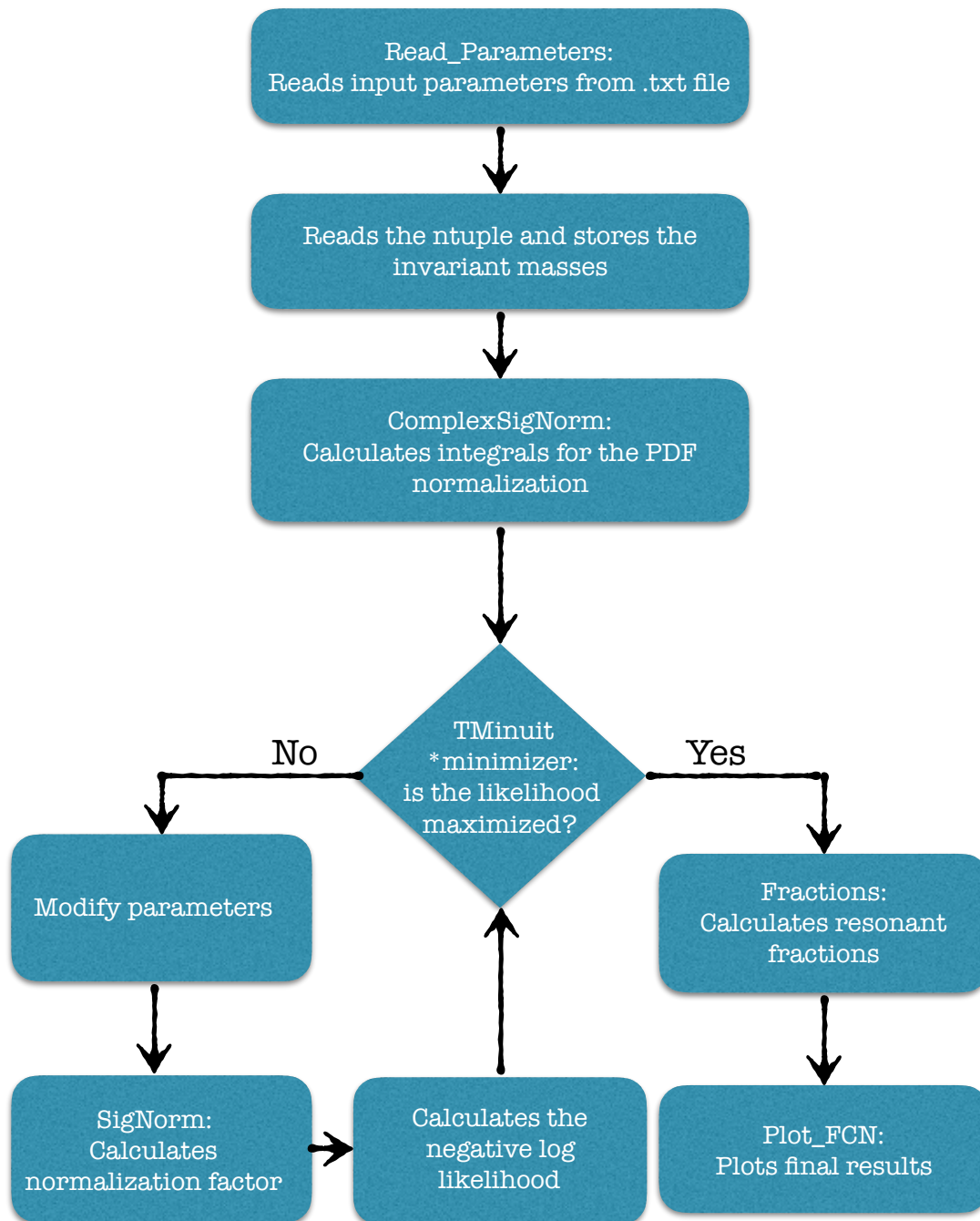


Figure 6.2: Simplified fluxogram of the Log Likelihood Fitter algorithm.

For fits with floating masses and widths, as well as PWA fits, where integrals must be recalculated every iteration, the least squares fitter requires longer processing times, when compared to the Log Likelihood Fitter, since the integrals calculation must be done for every bin. The large amount of events represents a smaller increase in processing time in the maximum likelihood fitter. We use in our analysis the ML fitter and all results are shown with this choice, unless stated otherwise. A simplified fluxogram of the Chi2 Fitter algorithm is shown at figure 6.3.

6.5 Code Validation

The code is validated by fitting ensembles of toy MC samples generated according to the same model and comparing the fit results with the generation parameters. A large number of samples is generated and fitted in order to make a statistically significant comparison. A total number of 500 samples with 10^6 events each are used. We use for this test a simplified model of the $D^+ \rightarrow K^- K^+ \pi^+$ decay, inspired by the best fit obtained by CLEO [56], with the generation parameters shown in table 6.1.

Resonant Channel	Parameter	Value
$K^*(892) + K$	Real part	1.0
	Imaginary part	0.0
$K^*(1430) + K$	Real part	0.14364
	Imaginary part	0.39467
$\phi(1020) + \pi$	Real part	-1.46112
	Imaginary part	-0.4190
$a_0(1450) + \pi$	Real part	-0.05918
	Imaginary part	0.1213
$\phi(1020) + \pi$	Real part	0.01151
	Imaginary part	-0.2197

Table 6.1: Generation parameters of the code validation tests, inspired in the CLEO model.

A histogram for each fitted parameter is filled with fit results and fitted with a Gaussian, as seen in figure 6.4. If the fit is working properly, the fitted parameter

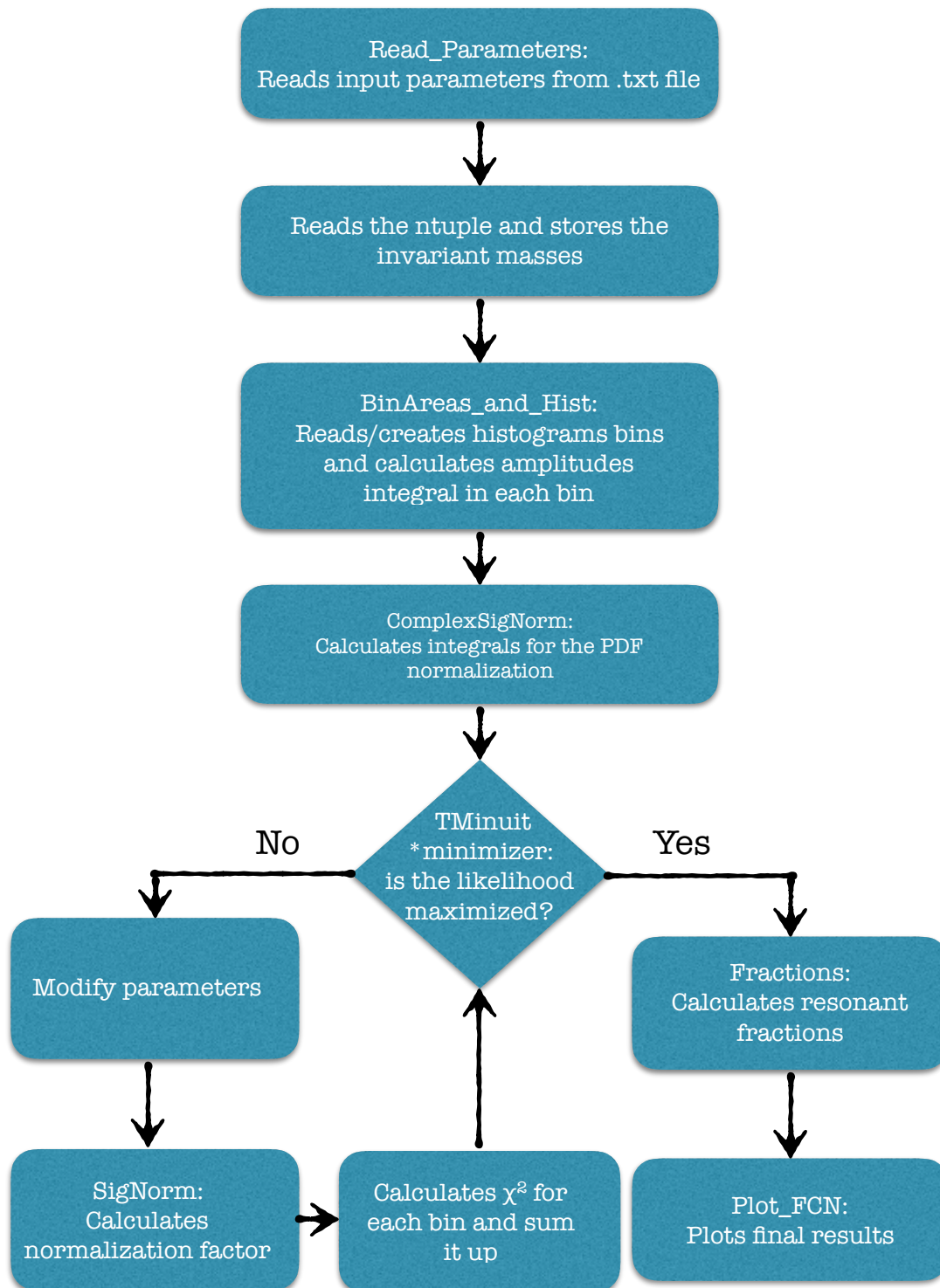


Figure 6.3: Simplified fluxogram of the Chi2 Fitter algorithm.

distribution is expected to be Gaussian with mean equal to the parameter value used in generation. Also, the Gaussian width is expected to be compatible with the error given by the fitter.

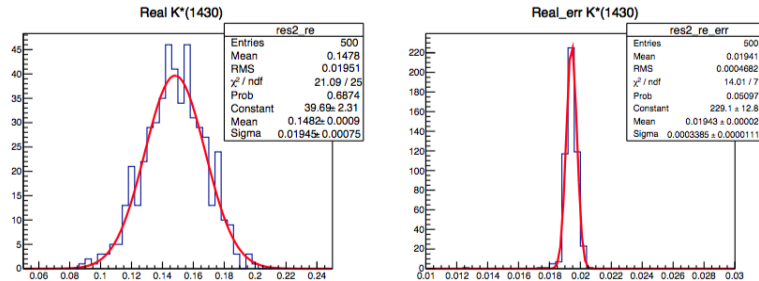


Figure 6.4: Fit results for the real part of the $K^*(892) + K$ resonant coefficient. On the left we see the distribution of fit results for the parameter itself, while on the right we see the error distribution, both fitted by Gaussians.

With this test we are able to check the package self-consistency, to verify if the algorithm presents any biases and if we have a suitable precision on the calculation of the integrals.

We see on table 6.2 and 6.3 the comparison between generated \times fitted parameters and errors \times Gaussian widths using 100 points for the Gauss-Legendre integration. We see that although the fits show a pattern close to the expected, the fit results are not in agreement with the generation parameters. This has been found to be due to the $\phi(1020)$ resonance, which has a width of $\approx 4\text{MeV}/c^2$, for which the derivative of the amplitude function is very large. The precision on the integral calculations is not sufficient for such a narrow function. Fit errors, on the other hand, behave as expected.

Simply increasing the number of integration points for all integrals would increase drastically the processing time of the fit, since the processing of the integral calculation is proportional to the square of the number of integration points. An alternative approach was adopted, in which we use more points only at the region around the $\phi(1020)$ peaks. The optimal number of integration points was found to be a combination of 250 points for the integration along the s_{13} axis and three sets

Resonant Channel	Parameter	P_{gen}	μ	$(P_{gen} - \mu)/\sigma_\mu$
$K^*(892) + K(\text{fixed})$	Real part	1.0	1.0	-
	Imaginary part	0.0	0.0	-
$K^*(1430) + K$	Real part	0.14364	0.1482 ± 0.0009	-5.1
	Imaginary part	0.39467	0.3954 ± 0.0005	-1.5
$\phi(1020) + \pi$	Real part	-1.46112	-1.461 ± 0.001	-0.1
	Imaginary part	-0.4190	-0.4182 ± 0.0003	2.7
$a_0(1450) + \pi$	Real part	-0.05918	-0.0599 ± 0.0003	2.4
	Imaginary part	0.1213	0.1209 ± 0.0003	1.3
$\kappa + \pi$	Real part	0.01151	0.1487 ± 0.0006	-5.6
	Imaginary part	-0.2197	-0.2181 ± 0.0004	4.0

Table 6.2: Comparison table between generation parameters and fitted values for fits with 100 integrations points. P_{gen} stands for generation parameters, μ is the mean of the fitted Gaussian over the fit results distribution and the last column is the pull. Fit results are not in good agreement with generation parameters.

Resonant Channel	Parameter	σ_{Gaus}	σ_{fit}	$(\sigma_{Gaus} - \sigma_{fit})/\sigma_{\sigma_{Gaus}}$
$K^*(892) + K(\text{fixed})$	Real part	0.0	0.0	-
	Imaginary part	0.0	0.0	-
$K^*(1430) + K$	Real part	0.0194 ± 0.0007	0.0194	0.0
	Imaginary part	0.0104 ± 0.0004	0.0103	0.25
$\phi(1020) + \pi$	Real part	0.00234 ± 0.00008	0.00225	1.12
	Imaginary part	0.0073 ± 0.0003	0.0075	-0.7
$a_0(1450) + \pi$	Real part	0.0057 ± 0.0002	0.0058	-0.5
	Imaginary part	0.0060 ± 0.0002	0.0060	-0.0
$\kappa + \pi$	Real part	0.0125 ± 0.0004	0.0137	-3.0
	Imaginary part	0.0090 ± 0.0004	0.0092	-0.5

Table 6.3: Comparison table between the widths of Gaussian fits and errors provided by the fit with 100 integrations points. σ_{Gaus} stands for the width of the Gaussian fit over the fit result distribution, σ_{fit} is the mean of the Gaussian fit over the error distribution and the last column is the pull. Fit errors are compatible with the observed distribution, even though a discrepancy can be seen.

of 250 points along the s_{12} axis: before, on and after the $\phi(1020)$ peak region.

With this special integration in hand it was possible to achieve a consistent generation and fit agreement, as shown on tables 6.4 and 6.5.

The MIPWA implementation is also tested and results show that the model is working as expected. By fitting a sample where we used the same isobar KK S-wave composition as in the previous test, but increasing the $a_0(1450)$ contribution, and fitting with a MIPWA amplitude function for the S-wave, we obtain a result which

Resonant Channel	Parameter	P_{gen}	μ	$(P_{gen} - \mu)/\sigma_\mu$
$K^*(892) + K(\text{fixed})$	Real part	1.0	1.0	-
	Imaginary part	0.0	0.0	-
$K^*(1430) + K$	Real part	0.14364	0.1441 ± 0.0009	-0.5
	Imaginary part	0.39467	0.3950 ± 0.0005	-0.6
$\phi(1020) + \pi$	Real part	-1.46112	-1.4610 ± 0.0001	-1.2
	Imaginary part	-0.4190	-0.4190 ± 0.0001	0.0
$a_0(1450) + \pi$	Real part	-0.05918	-0.0591 ± 0.0003	-0.3
	Imaginary part	0.1213	0.1213 ± 0.0003	0.0
$\kappa + \pi$	Real part	0.01151	0.01186 ± 0.0006	-0.6
	Imaginary part	-0.2197	-0.2199 ± 0.0005	0.4

Table 6.4: Comparison table between generation parameters and fitted values for fits with 250 integrations points and the special integration on the $\phi(1020)$ region. P_{gen} stands for generation parameters, μ is the mean of the fitted Gaussian over the fit results distribution and the last column is the pull. Fit results are in good agreement with generation parameters.

Resonant Channel	Parameter	σ_{Gaus}	σ_{fit}	$(\sigma_{Gaus} - \sigma_{fit})/\sigma_{Gaus}$
$K^*(892) + K(\text{fixed})$	Real part	0.0	0.0	-
	Imaginary part	0.0	0.0	-
$K^*(1430) + K$	Real part	0.0190 ± 0.0007	0.0194	-0.6
	Imaginary part	0.0107 ± 0.0003	0.0103	1.7
$\phi(1020) + \pi$	Real part	0.00214 ± 0.00007	0.00225	-1.7
	Imaginary part	0.0073 ± 0.0003	0.0075	-1.0
$a_0(1450) + \pi$	Real part	0.0056 ± 0.0002	0.0058	-1.0
	Imaginary part	0.0058 ± 0.0002	0.0060	-1.0
$\kappa + \pi$	Real part	0.0134 ± 0.0004	0.0137	-0.75
	Imaginary part	0.0097 ± 0.0004	0.0093	1.0

Table 6.5: Comparison table between the widths of Gaussian fits and errors provided by the Dalitz fits with 250 integrations points and the special integration on the $\phi(1020)$ region. σ_{Gaus} stands for the width of the Gaussian fit over the fit result distribution, σ_{fit} is the mean of the Gaussian fit over the error distribution and the last column is the pull. Fit errors are compatible with the observed distribution, even though a discrepancy can be seen.

is compatible with generation parameters. Figures 6.5 and 6.6 show, for the real and imaginary parts, respectively, the direct comparison of the fitted value and the generated S-wave amplitude value at each point.

Another validation test was performed by comparing Rio+ with the Laura++ package [47], which is well established and has been used in many analyses by BaBar

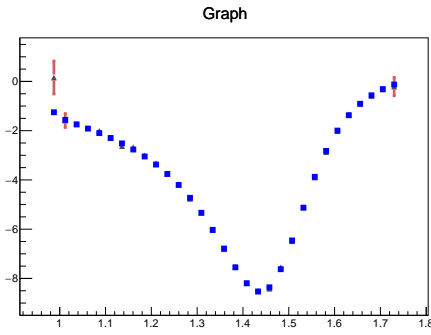


Figure 6.5: Comparison between fitted (grey triangles) and generation (blue squares) values for the real part of the MIPWA S-wave amplitude.

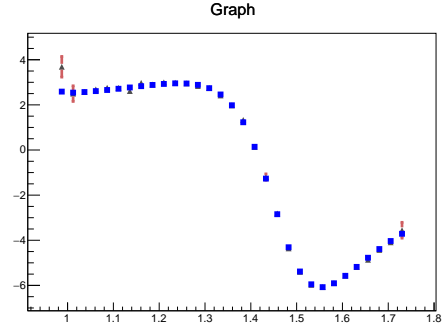


Figure 6.6: Comparison between fitted (grey triangles) and generation (blue squares) values for the imaginary part of the MIPWA S-wave amplitude.

and LHCb. This was done by Josué Molina for the $D^+ \rightarrow \pi^- \pi^+ \pi^+$ decay. For this test it was necessary to modify the amplitude functions in Rio+ to match the one in Laura++. By fitting a single toy MC with both packages and comparing the results we see full agreement with respect to phases and fractions, as shown in tables 6.6 and 6.7. Amplitudes are not comparable due to distinct normalization strategies.

Resonant channel	Amplitude	Phase	Fraction (%)
$\rho(770)$	$1.0 \pm \text{fixed}$	$0.0 \pm \text{fixed}$	54.9 ± 2.1
$f_0(980)$	1.56 ± 0.03	-47.0 ± 2.4	20.8 ± 1.3
$f_2(1270)$	0.31 ± 0.01	26.0 ± 5.8	2.3 ± 0.4
$\rho(1450)$	2.09 ± 0.14	74.8 ± 6.6	2.3 ± 0.4
$f_0(X)$	1.56 ± 0.18	37.7 ± 6.6	2.1 ± 1.0
$\sigma(500)$	3.1 ± 0.1	66.1 ± 1.7	19.1 ± 1.9

Table 6.6: Fit results for the $D^+ \rightarrow \pi^- \pi^+ \pi^+$ decay using the Rio+ package.

Resonant channel	Amplitude	Phase	Fraction (%)
$\rho(770)$	$1.0 \pm \text{fixed}$	$0.0 \pm \text{fixed}$	54.9
$f_0(980)$	0.62 ± 0.01	-46.9 ± 2.4	20.8
$f_2(1270)$	0.21 ± 0.01	25.2 ± 5.9	2.3
$\rho(1450)$	0.29 ± 0.02	74.4 ± 6.8	2.3
$f_0(X)$	0.20 ± 0.02	37.1 ± 6.7	2.1
$\sigma(500)$	0.59 ± 0.02	66.3 ± 1.7	19.1

Table 6.7: Fit results for the $D^+ \rightarrow \pi^- \pi^+ \pi^+$ decay using the Laura++ package.

Chapter 7

Data Sample and Selection Criteria

In this chapter we define the data and simulated samples used in this analysis, as well as the criteria used to select the final sample. This is a crucial stage in the Dalitz plot analysis. Its effect on the phase space distribution may affect drastically the results. It is important, then, to choose selection criteria with an efficiency as flat as possible in the Dalitz plot.

7.1 Data and MC samples

7.1.1 Data Samples

This analysis is based on approximately 2.0 fb^{-1} of pp collisions at $\sqrt{s} = 8 \text{ TeV}$ collected by LHCb during 2012, for which $1.000 \pm 0.012 \text{ fb}^{-1}$ were taken with magnet polarity up (MagUp) and $0.988 \pm 0.012 \text{ fb}^{-1}$ with magnet polarity down (MagDown). The version of the data reconstruction algorithm is called `Reco14` and it was analyzed using `DAVINCI v34r1`. We use data selected by the version of the stripping algorithm called `Stripping20`, through the `StrippingD2hhh_KKPLine` exclusive line, for which the selection criteria were developed specifically for the $D^+ \rightarrow K^- K^+ \pi^+$ decay.

7.1.2 MC Samples

The Monte Carlo simulated data is used to guide the selection criteria and to extract the acceptance across the Dalitz plot. All samples were generated phase space with Gauss v45r3, using MC12 configuration (Reco14a, Digi13, Nu2.5-Pythia8) and DaVinci v34r1 to analyze them. In order to be able to generate large signal MC samples, we have simulated events with generator level cuts (shown in Table 7.1) and also trigger lines `Hlt1TrackAllL0` & `Hlt2CharmHadD2HHH` filters. This sample was also stripping filtered, with `Stripping20` passing through the inclusive line `StrippingD2hhh_HHHIncLine` which has no PID cuts and the mass of the pion is assigned to all the three tracks.

The signal sample and specific backgrounds relevant for this analysis are shown in Table 7.2.

This sample contains a fraction of the order of 9% where the $D^+ \rightarrow K^- K^+ \pi^+$ come from b -hadron decays. In order to ensure that the efficiencies computed from the prompt MC samples are well defined, we process the signal sample with a filter that retains only events that contain a promptly produced signal decay. The filter traces the ancestry of the generated signal D^+ . If any of its ancestors has a mean lifetime longer than 0.1 fs then it is classified as not-prompt.

Table 7.1: Cuts applied at generator level.

variable	cut
$D_{(s)}p >$	14.0 GeV/ c
$D_{(s)}p_T >$	2.1 GeV/ c
each daughter $p >$	2.0 GeV/ c
each daughter $p_T >$	0.25 GeV/ c
all daughters inside the detector acceptance	$0.01 < \theta < 0.4rad$

Table 7.2: Monte Carlo simulated data samples for signal and specific backgrounds.

Event type	Decay	Number of events MagDown/MagUp
21163002	$D^+ \rightarrow K^- K^+ \pi^+$	676725/661661
23103404	$D_s \rightarrow \Phi \pi \pi^0$	50529/50781
23163003	$D_s^+ \rightarrow K^- K^+ \pi^+$	609964/612319
11164450	$B^+ \rightarrow D^+ \pi^-, D^+ \rightarrow K^- \pi^+ \pi^+ \pi^0$	1042631/1032391
11164451	$B^+ \rightarrow D^+ K^-, D^+ \rightarrow K^- \pi^+ \pi^+ \pi^0$	1034458/1015783

7.2 Selection Criteria

In order to reduce the data rate across the acquisition and to improve the signal over background ratio, candidates are selected based on the decay topology and their kinematical profile. We start by requiring good quality tracks by cutting on the $\chi^2/ndof$ of the track fit. Variables such as the momenta of the tracks and the reconstructed mass of the D meson can be used to distinguish signal events from background. The momentum p and the transverse momentum p_T are expected to be higher in signal candidates, due to the high mass of the D meson. Signal candidates are also expected to contain a reconstructed mass M_D closer to the nominal mass of the D meson.

More complex criteria are additionally used. The Impact Parameter (IP) with respect to the primary vertex is the smallest distance between the track (or projected trajectory) and the collision point (fig. 7.1). Daughter tracks are expected to point to the D meson decay vertex, therefore having a higher IP than tracks coming from the PV, while the prompt D itself comes directly from the PV, having a low IP. The IP χ^2 , defined as the χ^2 difference in the IP with respect to the primary vertex (PV) reconstructed with and without this particle, is lower for particles that come from the primary vertex, being higher otherwise, and presents excellent discriminating power. Alternatively, one may use a variable that combines the IP χ^2 of the D

meson and all daughters at the same time, called LogIPChi2, given by:

$$\text{LogIPChi2} = \log \left(\frac{\chi_{IP_{K^-}}^2 \times \chi_{IP_{K^+}}^2 \times \chi_{IP_{\pi^+}}^2}{\chi_{IP_{D^+}}^2} \right) \quad (7.1)$$

The D Vertex χ^2 refers to the quality of the D decay vertex. Signal candidates provide better decay vertices and, therefore, lower D Vertex χ^2 . The D Flight Distance (FD) and its significance (FD χ^2) are good discriminating variables against the D_s meson, which has a lower lifetime. The FD_{χ^2} is the ratio $\text{FD}/\sigma_{\text{FD}}$ and for signal candidates it is higher. The θ_{DIRA} defined as the angle between the reconstructed D momentum and the vector connecting the PV with the reconstructed D decay vertex (fig. 7.2). Since D mesons are expected to come from the primary vertex, this angle is typically low and its cosine, therefore, is close to 1. The Distance Of Closest Approach (DOCA) is the smallest distance between two tracks and, for particles that come from the same vertex, it has a low value.

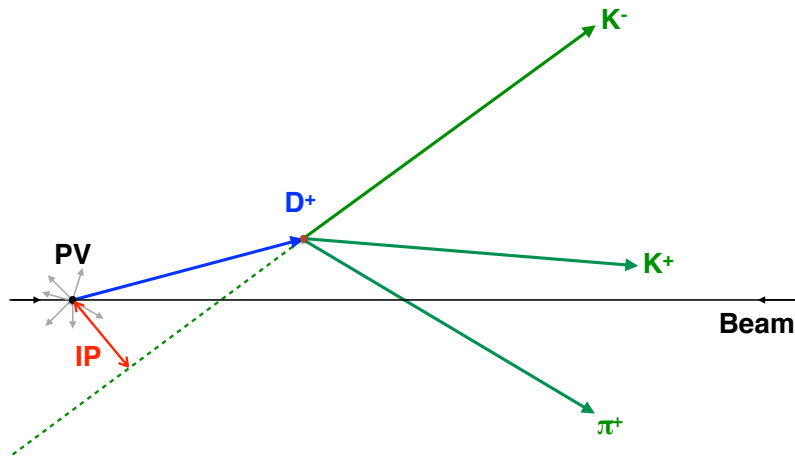


Figure 7.1: Impact parameter representation.

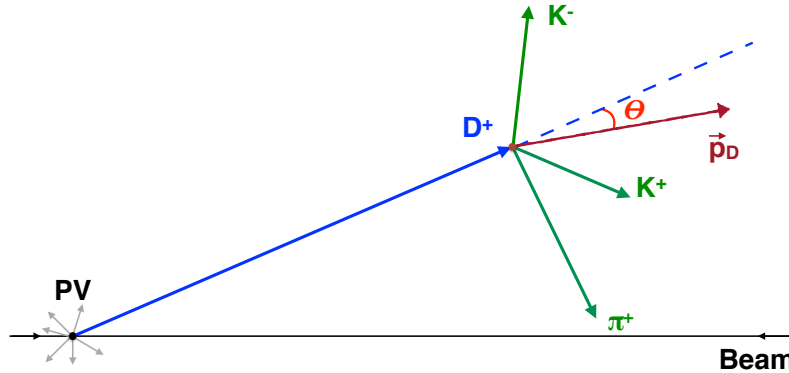


Figure 7.2: Representation of the θ angle, used to calculate the DIRA, shown in red.

7.3 Stripping, Trigger and kinematic vetoes

The stripping selection requirements are chosen as a compromise between signal efficiency, timing and retention. The cuts of the exclusive `StrippingD2hhh_KKPLine` used to select the data are very similar to the ones used in the inclusive `StrippingD2hhh_HHHIncLine` used for the MC sample (shown in Table 7.3). For the variables where the cuts are different, the tightest one is applied to both data and MC (except the PID, which is not applied in MC, due to differences between efficiencies in MC and data). The mass distributions after stripping cuts are shown in Figure 7.3. At this stage we have approximately 20.4M and 20.1M $D^+ \rightarrow K^- K^+ \pi^+$ candidates for MagDown and MagUp polarities, respectively, with a purity of 77% in a $\approx 3\sigma$ mass window around the mean mass, as can be seen in Figure 7.4. At this point we have to choose which trigger requirements will be used in order to know which cuts have been applied to the data.

For Hlt2 [59], the candidate must fire the dedicated `Hlt2CharmHadD2HHH` trigger line, which selects $D_{(s)}^+$ decays into 3 charged hadrons. Its requirements are shown in Table 7.4, where we can see that the candidate needs to have fired any `Hlt1Track`

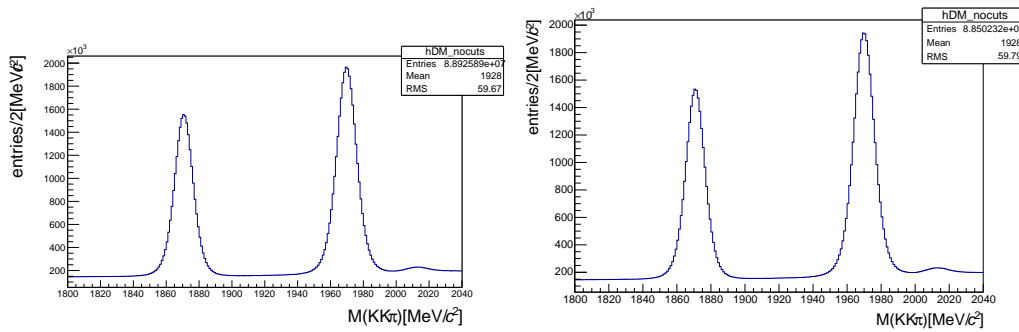


Figure 7.3: $K^- K^+ \pi^+$ Mass distributions for MagDown (left) and MagUp (right) as they come out of the Stripping 20.

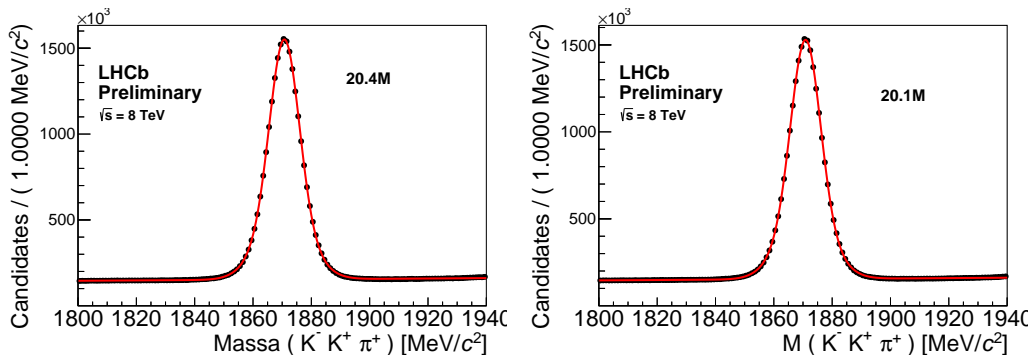


Figure 7.4: Fit to Mass distributions of $D^+ \rightarrow K^- K^+ \pi^+$ for MagDown (left) and MagUp (right) as they come out of the Stripping 20.

Line. For this analysis we restrict them to pass only the `Hlt1TrackAllL0`. This HLT1 line imposes the cuts shown in Table 7.5 on at least one track in the event. After these requirements on Hlt we keep 16.4M and 16.1M $D^+ \rightarrow K^- K^+ \pi^+$ candidates in MagDown and MagUp polarities, respectively, with an improved purity of 88.5%.

For the hardware trigger selection, it is required that the event is either `L0Hadron_TOS` or `TIS` on the `L0Hadron`, `L0Electron`, `L0Photon` or `L0Muon` D^+ candidate. The `L0Hadron` trigger requires at least one E_T deposit in a 2×2 set of cells in the calorimeter with a minimum energy of 3.62 GeV^1 and a total number of SPD hits smaller than 600. By adding the `TIS` candidates to the sample, the statistical significance is improved for signal mode. Besides, this extra path provides an opportunity to subdivide the data and check for systematic effects. The fraction of `L0Hadron_TOS`

¹This value was used in the largest fraction of the data. For a detailed list, refer to Appendix B

candidates at this stage is 34%.

The mass distributions after the trigger requirements on the 3 levels are shown in Figure 7.5. The yields are approximately 15.6M and 15.4M for MagDown and MagUp polarities, respectively, keeping the purity at 89%.

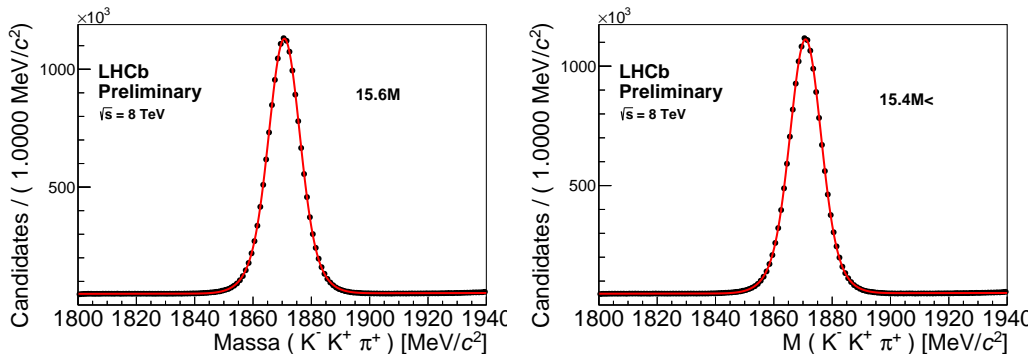
Table 7.3: Stripping 20 cuts for `StrippingD2hhh_KKPLine` and `StrippingD2hhh_HHHInCLine`.

Variable	exclusive KKP	Cuts for inclusive HHH
Final state particles		
Track χ^2 / ndof	< 5	< 5
p_T	$> 250 \text{ MeV}/c$	$> 250 \text{ MeV}/c$
p	$> 2000 \text{ MeV}/c$	$> 2000 \text{ MeV}/c$
IP χ^2	> 4	> 4
IP χ^2 on 2 daughters	> 10	> 10
$\Delta \log \mathcal{L}_{K\pi}$ for K	> 7	–
$\Delta \log \mathcal{L}_{K\pi}$ for π	< 3	–
$\sum p_T$	$> 2800 \text{ MeV}/c$	$> 2800 \text{ MeV}/c$
$D_{(s)}$		
D Vertex χ^2	< 30	< 30
D (p_T)	$> 1000 \text{ MeV}/c$	$> 1000 \text{ MeV}/c$
Mass	$1800 < m_D < 2040 \text{ MeV}/c^2$	$1100 < m_D < 2070 \text{ MeV}/c^2$
D FD χ^2	> 125	> 125
IP χ^2	< 12	< 12
$\cos \theta_{DIRA}$	> 0.98	> 0.0
Global		
Number of Tracks	< 500	< 500

In addition to the stripping and trigger requirements, some vetoes are applied because the use of PIDCalib package. It is known that the $\Delta \log \mathcal{L}_{K\pi}$ variables are not well described in the MC samples. In order to have reliable efficiencies due to PID requirements, it is necessary to use the data-driven PIDCalib technique. It makes use of calibration tracks from decay modes which may be cleanly reconstructed without the use of the PID discriminants. The calibration decay mode used in this analysis is the $D^* \rightarrow D^0(K\pi)\pi$. These tracks are binned in p and η to obtain the data driven PID efficiencies which will be used in the MC candidates as a weight. Since there are

Table 7.4: Selection criteria for HLT2CharmHadD2HHH

Cuts	Value
GEC	N. Long Tracks < 180
	Track χ^2 < 3
final state particles	p_T (MeV/c) > 300
	p (MeV/c) > 3000
	IP χ^2 > 6
hhh combination	$\sum p_T$ (MeV/c) > 2800
	min DOCA (mm) < 0.08
	FD χ^2 > 175
D^\pm	Vertex χ^2/ndf < 15
	IP χ^2 < 12
	Mass (MeV/c ²) 1800–2040
TOS in any Hlt1Track Line	

Figure 7.5: Fit to Mass distributions of $D^+ \rightarrow K^- K^+ \pi^+$ for MagDown (left) and MagUp (right) after the trigger requirements.

regions of p and η with no calibration data, we exclude $D^+ \rightarrow K^- K^+ \pi^+$ candidates in which the daughter tracks fall into these regions. The cuts applied are shown in Table 7.6.

7.4 Offline Selection

The background present in the data sample is composed by a combinatorial contribution and other charm particle decays.

For a more accurate amplitude analysis, we need to choose a selection criteria that provides a highly pure sample, but at the same time, do not distorts the Dalitz

Table 7.5: H1t1TrackAllL0 requirements on at least one track

Track $IP\chi^2 > 16$
Track $p_T > 1.6$ GeV
Track $P > 3$ GeV
Track $\chi^2/ndf < 2$
Track IP > 0.1 mm
Number of VELO hits/Track > 9
Number of missed VELO hits/Track < 3
Number of Velo hits/Track > 9
Number of OT + IT hits/Track > 16
Number of Velo hits < 6000
Number of IT hits < 3000
Number of OT hits < 15000
L0_Decision_Physics

Table 7.6: Kinematically vetoed regions of the p and η phase space such that the data-driven PIDCalib method may be properly utilized.

$3 < \text{Track } p < 100\text{GeV}$
$1.5 < \text{Track } \eta < 5$

plot distribution. Examples of variables that are very efficient in discriminating the signal against backgrounds not coming from D mesons are the p_T and the impact parameter of the three daughter tracks, but they are avoided because they cause large inefficiencies in the corners of the Dalitz plot, regions where one of the daughters have a soft p_T or IP, as can be seen in Figure 7.6.

Another care that should be taken when dealing with Dalitz plot analysis is to avoid border effects. To this end the DecayTreeFitter tool [60] is employed, using a constraint on the D mass.

First, we try to identify and reduce the specific charm backgrounds, like reflections due to misidentification of the final state particles and partially reconstructed decays, where one of the final state particle is missing, and then we proceed to

further reduce the combinatorial background.

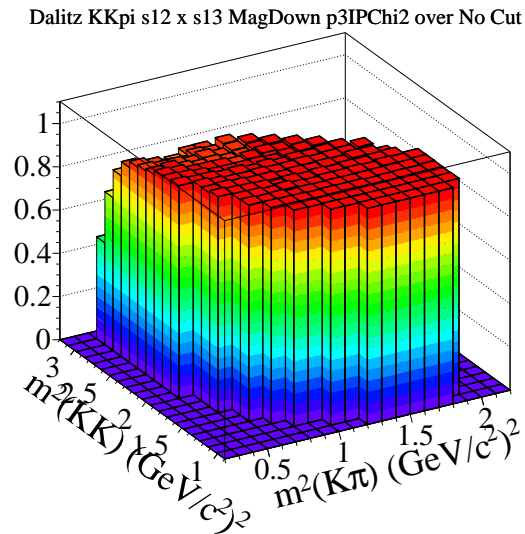


Figure 7.6: Distortion given by a cut in $p3_IPCHI2 > 6$. This cut would discriminate candidates reconstructed with a random pion, but it introduces a large distortion. The distributions correspond to the Dalitz plot after applying the cut divided by the one before applying it.

7.4.1 Specific backgrounds

The main contributions for the charm background are:

- $\Lambda_c^+ \rightarrow K^- p \pi^+$;
- D^0 decays from the D^{*+} chain, $D^{*+} \rightarrow D^0(K^- \pi^+ \pi^0) \pi^+$, $D^0(K^- K^+ \pi^0) \pi^+$;
- semileptonic decays of D mesons with muons in the final state like $D^+ \rightarrow K^- \pi^+ \mu^+ \nu$;
- decays with a missing π^0 such as $D_s^+ \rightarrow \phi \pi^+ \pi^0$ and $D^+ \rightarrow K^- \pi^+ \pi^+ \pi^0$ which has also a misidentification;
- $D_s^+ \rightarrow K^- K^+ \pi^+$

The contamination from $\Lambda_c^+ \rightarrow K^- p \pi^+$ occurs due to a proton to K misidentification of the positively charged Kaon. It can be seen in Figure 7.7 a very clear Λ_c^+

peak when the $D^+ \rightarrow K^- K^+ \pi^+$ data is reconstructed as $K^- p \pi^+$ after the stripping and trigger requirements. At this point there are about 1.1K Λ_c^+ candidates, which are removed by applying a mass veto $2274 < M(K^- p \pi^+) < 2300 \text{ MeV}/c^2$ which has an efficiency of 93.6% on the $D^+ \rightarrow K^- K^+ \pi^+$ signal.

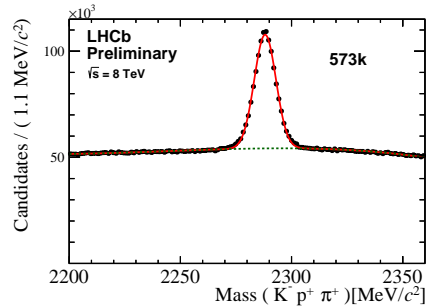


Figure 7.7: $D^+ \rightarrow K^- K^+ \pi^+$ candidates reconstructed as $K^- p \pi^+$ in the MagDown data sample after the stripping and trigger requirements.

The contamination from semileptonic decays with muons in the final state can be controlled by a muon veto (`isMuon==0`) applied to all three tracks. The efficiency of this cut is 94.5%. The `isMuon` is a boolean variable which is true when the number of hits in the muon chambers matching the trajectory of the particle is compatible with the expected number for a muon with the same momentum and direction.

The background from $D_s^+ \rightarrow \phi \pi^+ \pi^0$ is an important source because the ϕ shows up in the Dalitz plot with an angular distribution characteristic of spin 1 resonances, like the ϕ from the signal $D^+ \rightarrow K^- K^+ \pi^+$. To study this channel, we used a 100k MC sample available and processed it through the inclusive `StrippingD2hhh_HHHInc` line. It can be seen in Figure 7.8 that it populates mainly the left side band of the signal mass region. Since this decay is reconstructed with a missing π^0 , suitable discriminating variables are the ones related to pointing to the primary vertices. One of them is the DIRA. A cut on this variable is already applied to the stripping, but as can be seen in Figure 7.9, it can be tightened to reduce background from badly reconstructed decays, as in the case of any decays with missing π^0 and random combinations.

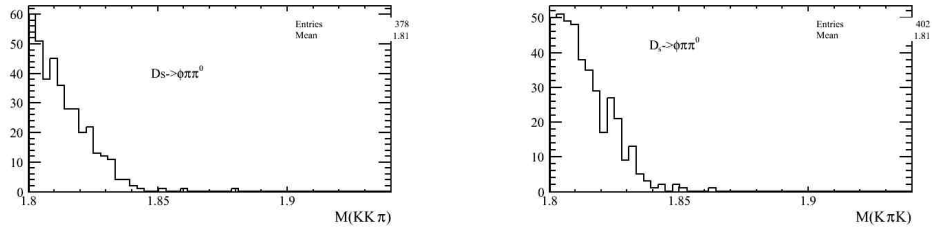


Figure 7.8: $K^-K^+\pi^+$ (right) and $K^-\pi^+K^+$ (left) mass distribution of true MC $D_s^+ \rightarrow \phi\pi^+\pi^0$ after the inclusive stripping.

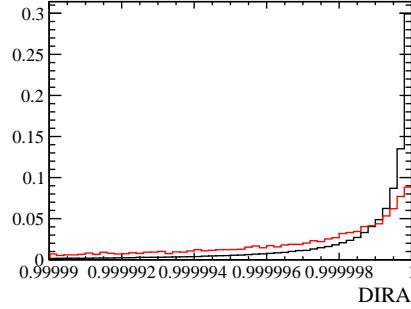


Figure 7.9: DIRA distribution for MC true $D^+ \rightarrow K^-K^+\pi^+$ (black) and true $D_s^+ \rightarrow \phi\pi^+\pi^0$ (red) after the stripping selection.

To further reduce this kind of background we use the LogIPChi2, which has a good discriminating power. Figure 7.10 shows its distribution after applying a $\text{DIRA} > 0.9999975$, for $D_s^+ \rightarrow \phi\pi^+\pi^0$ and $D^+ \rightarrow K^-K^+\pi^+$ MC events. A cut on $\text{LogIPChi2} > 13$ is applied improving the purity to 96.7%.

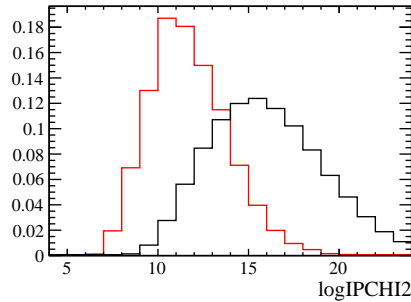


Figure 7.10: LogIPChi2 distribution for MC true $D^+ \rightarrow K^-K^+\pi^+$ (black) and true $D_s^+ \rightarrow \phi\pi^+\pi^0$ (red) after the stripping selection and $\text{DIRA} > 0.9999975$.

Another source of background that contributes with a ϕ with an angular distribution in the Dalitz plot are the $D_s^+ \rightarrow K^-K^+\pi^+$ decays that have a long radiative tail towards the D mass, as can be seen in Figure 7.11, which shows true MC $D_s^+ \rightarrow K^-K^+\pi^+$ decays. To reduce D_s decays we explore the longer lifetime of

the D meson and tighten the cut on the significance of the D vertex detachment $\text{FD } \chi^2 > 700$, improving the purity to 97.2%. The distribution of this variable is shown in Figure 7.12 for true MC decays of $D_s^+ \rightarrow \phi\pi^+\pi^0$, $D_s^+ \rightarrow K^-K^+\pi^+$ and $D^+ \rightarrow K^-K^+\pi^+$.

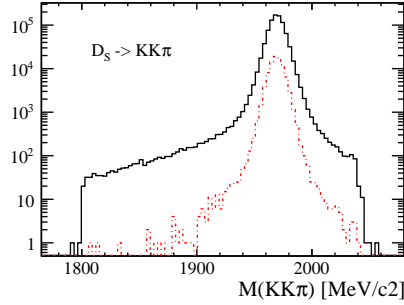


Figure 7.11: $KK\pi$ mass distribution from true MC $D_s^+ \rightarrow K^-K^+\pi^+$ events after stripping selection (solid black) and after all final cuts (dotted red).

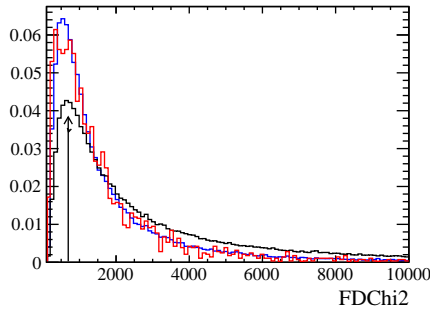


Figure 7.12: D $\text{FD } \chi^2$ for MC $D_s^+ \rightarrow \phi\pi^+\pi^0$ (red), $D_s^+ \rightarrow K^-K^+\pi^+$ (blue) and $D^+ \rightarrow K^-K^+\pi^+$ (black) after the stripping selection, $\text{DIRA} > 0.9999975$ and $\log\text{IPChi2} > 13$.

At this point, by looking at the Dalitz plot in Figure 7.13 it can be seen an structure at the left top corner, $s_{KK} > 2.8 \text{ GeV}^2/c^4$ and $s_{K\pi} < 0.65 \text{ GeV}^2/c^4$ which can be identified as badly reconstructed candidates and can be reduced by requiring a very good quality vertex fit, by cutting on D Vertex $\chi^2 < 15$.

The $D^+ \rightarrow K^-\pi^+\pi^+\pi^0$ can mimic the $D^+ \rightarrow K^-K^+\pi^+$ when the π^0 is lost and one π^+ is misidentified as a kaon, populating the whole 1800-1940 GeV/c region of interest, as can be seen in the left plot of Figure 7.14, where the true MC $D^+ \rightarrow K^-\pi^+\pi^+\pi^0$ decays are reconstructed as $KK\pi$. A tight cut on the particle identification variable $\Delta \log \mathcal{L}_{K\pi}$ for $K > 15$ is applied; the resulting mass distribution is also seen in the same Figure.

In summary, all the offline cuts are the ones in Tables 7.1, 7.3, 7.4, 7.6 and the final ones shown in Table 7.7, where it is displayed also the efficiency and purity reached after each one of them is applied. In Figure 7.7 we show the impact of each cut on the phase space distribution, where it can be seen that the distortion they produced is negligible.

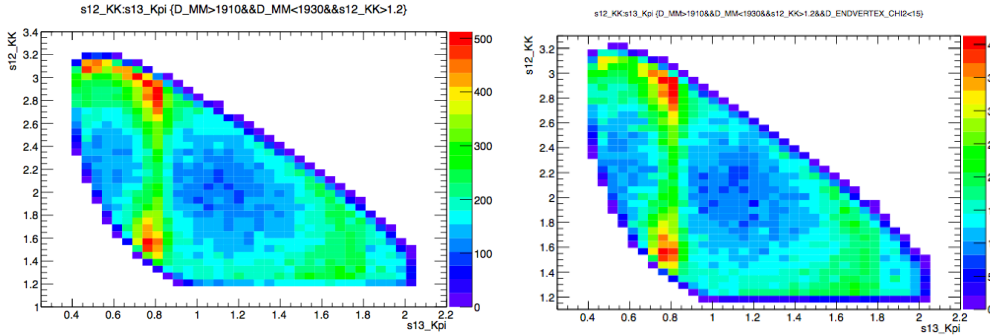


Figure 7.13: Dalitz plot of $D^+ \rightarrow K^- K^+ \pi^+$ in the mass region 1910–1930 (left) and after applying the D Vertex $\chi^2 < 15$ (right).

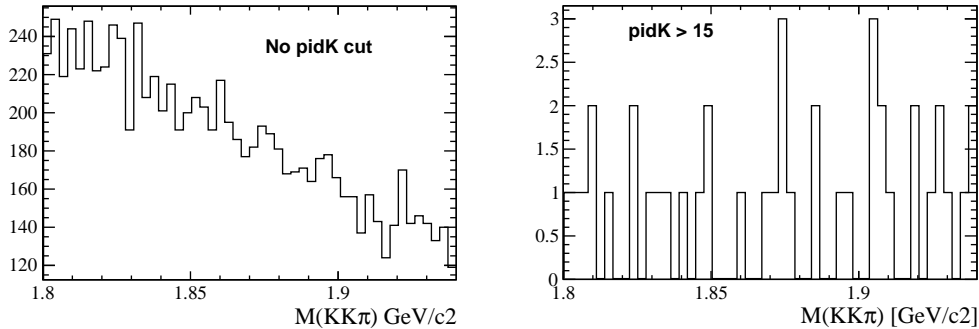


Figure 7.14: $KK\pi$ Mass distribution of true $D^+ \rightarrow K^- \pi^+ \pi^+ \pi^0$ MC events without $\Delta \log \mathcal{L}_{K\pi}$ cut (left) and after $\Delta \log \mathcal{L}_{K\pi} > 15$ (right).

7.4.2 Mass Fits

Data

After applying all the selection criteria mentioned in the previous section, a fit is performed to the $D^+ \rightarrow K^- K^+ \pi^+$ mass distribution in order to quantify the data sample. The fit model consists of a Gaussian plus a Cristal Ball [61] \mathcal{CB} function to describe the signal and an exponential is used for the background.

Table 7.7: Offline cuts. The efficiency is obtained by fitting the data sample and is calculated with respect to the previous cut.

Variable	Cut	Efficiency[%]	purity[%]
$M(K^- p\pi^+)$ veto	2274 – 2300 MeV/ c^2	93.6	90.0
isMuon	== 0	94.5	91.0
DIRA	> 0.9999975	75.0	95.3
Log IP χ^2	> 13	82.8	96.7
D FD χ^2	> 700	86.7	97.2
D Vertex χ^2	< 15	93.7	97.4
$\Delta \log \mathcal{L}_{K\pi}$ for K	> 15	65.2	98.5

The \mathcal{CB} consists of Gaussian core, that models the detector resolution, and a power-law on the left-hand side that parametrizes the effect of photon radiation by the final state particles in the decay.

$$\mathcal{CB}(m) \propto \begin{cases} \exp\left(-\frac{1}{2}t^2\right), & \text{if } t > -|a| \\ \frac{A}{(B-t)^n}, & \text{if } t \leq -|a| \end{cases}$$

where,

$$t = \frac{m - m_1}{\sigma_1}, \quad A = \left(\frac{n}{|a|}\right)^n \exp\left(-\frac{|a|^2}{2}\right) \quad \text{and} \quad B = \frac{n}{|a|} - |a|$$

with m being the free variable (measured mass), m_1 and σ_1 being the mean value and width of the core Gaussian, respectively, a is the transition point where the Gaussian becomes the power-law, and n is the exponent of the power law.

The mean values of the \mathcal{CB} and Gaussian are the same while the widths are allowed to be different, so the total signal probability density function (p.d.f.) is given by:

$$\mathcal{F}_{\text{sig}} = N_{\text{sig}} [f \mathcal{CB}(m_1, \sigma_1, a, n) + (1 - f)G(m_1, R_\sigma \sigma_1)]$$

where f is the fraction of candidates in the \mathcal{CB} and R_σ is the ratio between the widths of the \mathcal{CB} and the Gaussian.

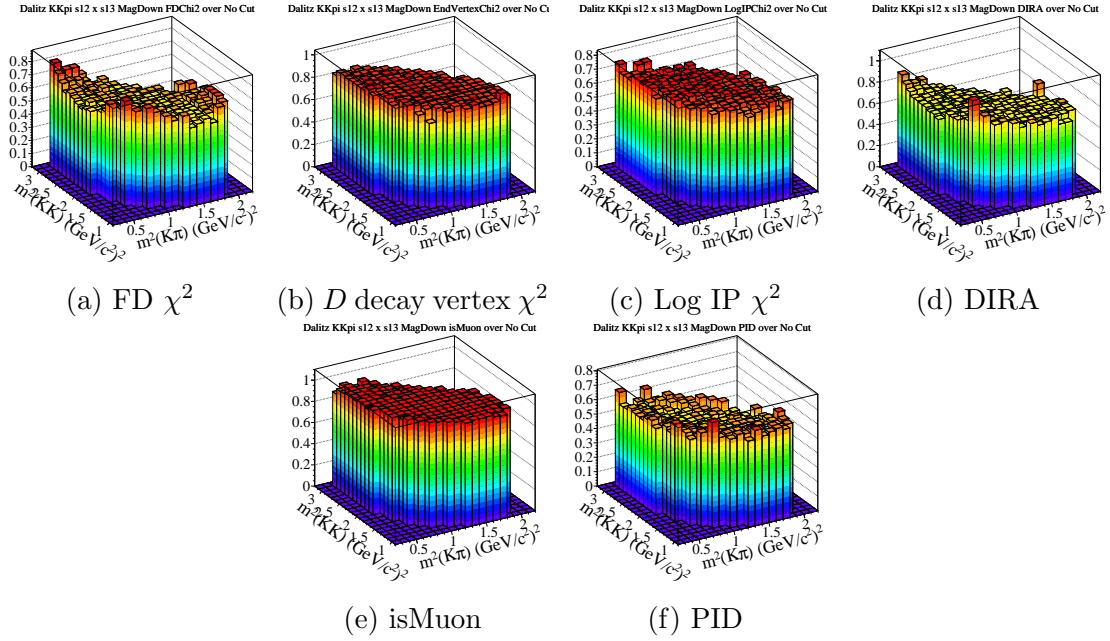


Figure 7.15: Distortion given by each selection criteria. The distributions correspond to the Dalitz plot after applying the cut divided by the one before applying it.

The L0 trigger selection criteria may have impact over the Dalitz distribution. Therefore, it is necessary to consider distinct trigger requirements in order to deal with their effects.

The mass fit of the sample, for both magnet polarities can be seen in figure 7.16. The D^+ yield is $N_{sig} = (8504 \pm 3) \times 10^3$, with 98.6 % purity. The fraction of candidates in the Cristal Ball f with respect to the total amount of candidates is $f = 0.367$, the mean value m_1 is 1870.80 MeV/ c^2 and the effective width, defined by $\sigma_{eff}^2 = f\sigma_{CB}^2 + (1-f)\sigma_{Gauss}^2$, is $\sigma_{eff} = 6.19$.

The corresponding mass fit requiring TOS with respect to L0 hadron line, is shown in figure 7.17. In this case, the D^+ yield is $N_{sig} = (2958 \pm 2) \times 10^3$, with 98.9 % purity. The fraction of candidates in the Cristal Ball is 0.37, with $m_1 = 1870.73$ MeV/ c^2 and $\sigma_{eff} = 6.18$ MeV/ c^2 .

The mass fit requiring TIS with respect to L0 muon, electron, photon and hadron lines, is shown in figure 7.18. The D^+ yield is $N_{sig} = 6404 \pm 3 \times 10^3$, also with 98.9 % purity. The fraction of candidates in the Cristal Ball is 0.73, the effective mean m_1 is 1870.87 MeV/ c^2 and the effective width σ_{eff} is 6.17 MeV/ c^2 .

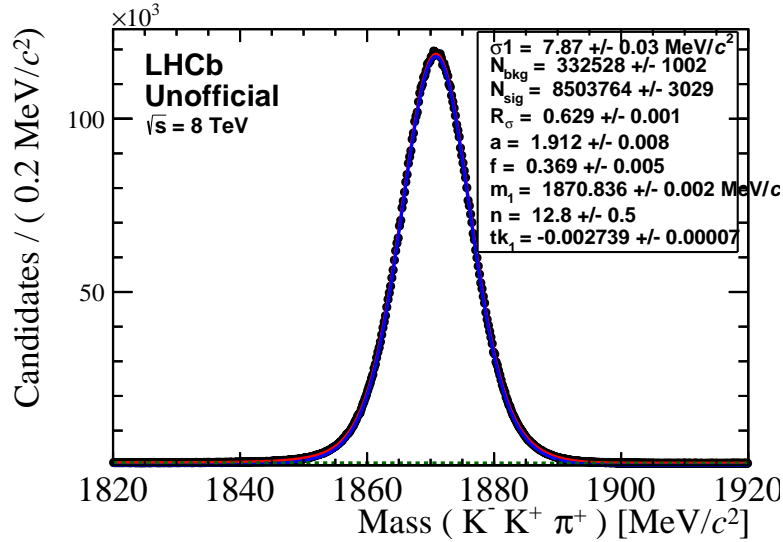


Figure 7.16: $K^-K^+\pi^+$ mass fit for the data sample after all selection criteria, using both magnet polarities. The D^+ yield is around 8.5×10^6 events.

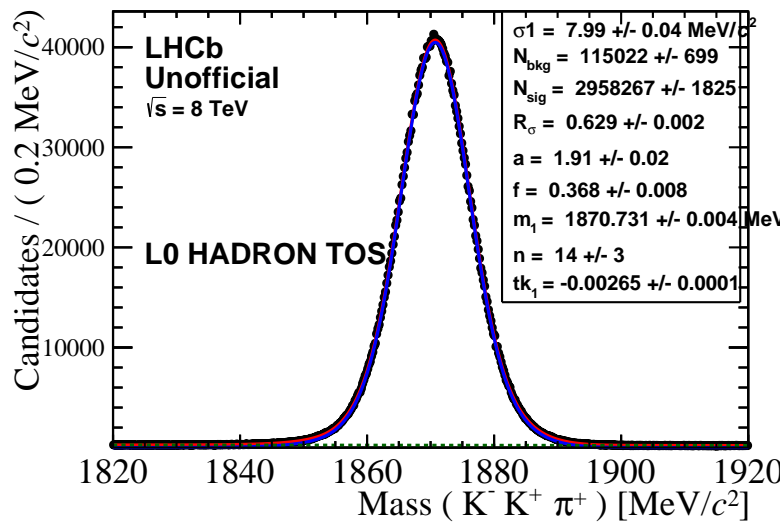


Figure 7.17: $K^-K^+\pi^+$ mass fit for the data sample after all selection criteria requiring TOS with respect to the L0 Hadron trigger lines, using both magnet polarities. The D^+ yield is nearly 3×10^6 events.

Monte Carlo

Monte Carlo simulated samples are needed in order to study the detection, reconstruction and selection efficiency. The mass fit plots for both magnet polarities and after all selection criteria, with the exception of particle identification requirements, are shown in figures 7.19, for the TOS requirement for L0 Hadron line, 7.20, for the TIS requirement with respect to the L0 muon, electron, photon and hadron

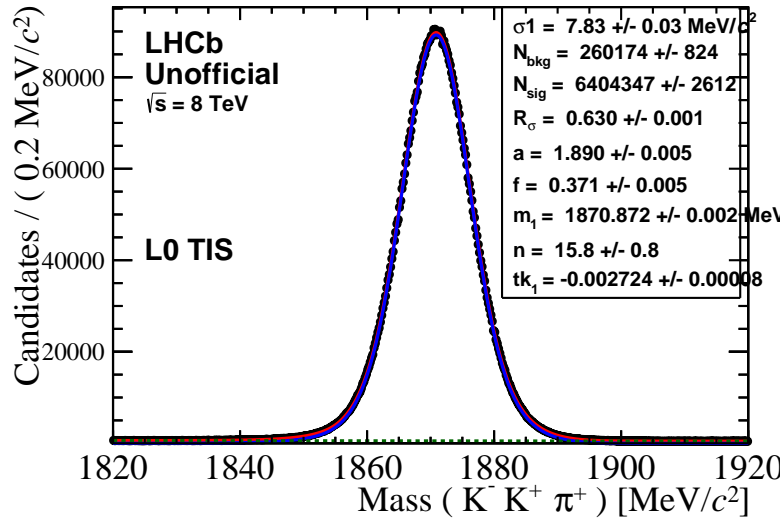


Figure 7.18: $K^-K^+\pi^+$ mass fit for the data sample after all selection criteria requiring TIS with respect to the L0 muon, electron, photon and hadron lines using, both magnet polarities. The D^+ yield is over 6×10^6 events.

lines, and 7.21 for an “or” of both requirements.

The LHCb MC sample is composed only by events which contain at least one signal candidate and is generated flat across the Dalitz plot. Around 105×10^3 events for the TOS sample, 165×10^3 events for the TIS sample and 234×10^3 for the TIS or TOS sample, providing good statistics to study the efficiencies across the Dalitz plot.

7.5 Background Dalitz Distribution

The contributions introduced by background sources modify the Dalitz plot distribution, and therefore, must be taken into account in the fit. To minimize its impact, strong selection criteria were chosen, reducing background levels to $\approx 1\%$.

The background distribution is taken from the sidebands, within the $1820 < M_D < 1840 \text{ MeV}/c^2$ and $1900 < M_D < 1920 \text{ MeV}/c^2$ mass windows, and included in the fit as a histogram. In order to avoid lower background levels at bins located on the border of the phase space, we divide the background Dalitz by another filled with a flat distribution with a large number of events simulated with Rio+. The

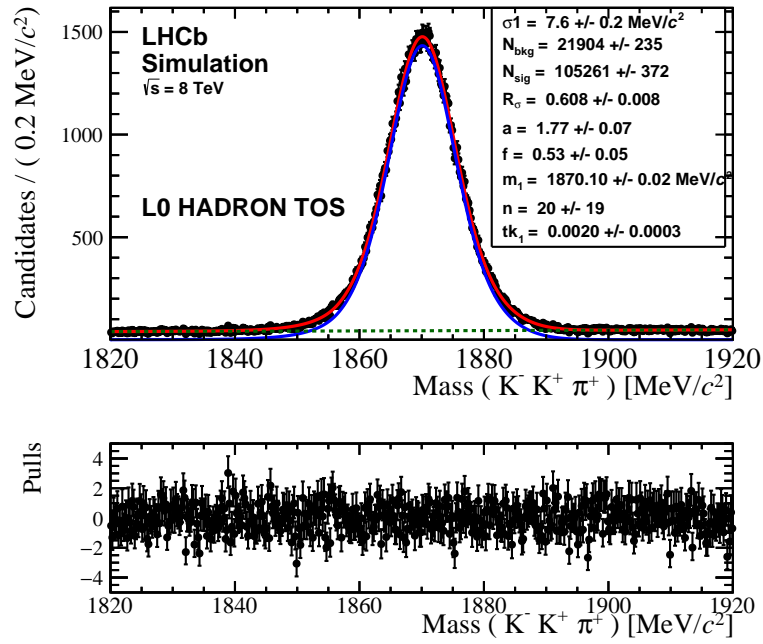


Figure 7.19: $K^-K^+\pi^+$ mass fit of the LHCb MC sample for the $D^+ \rightarrow K^-K^+\pi^+$ decay after all selection criteria requiring TOS with respect to L0 hadron line using both magnet polarities.

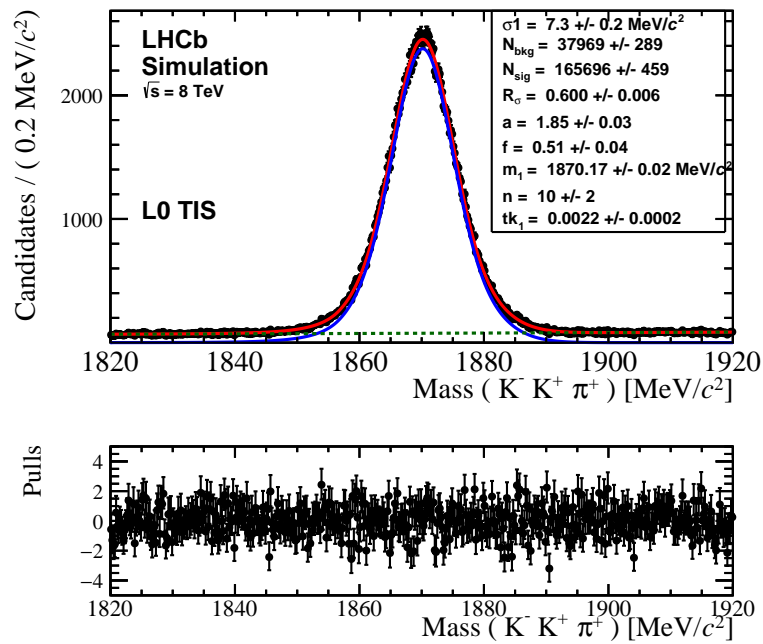


Figure 7.20: $K^-K^+\pi^+$ mass fit of the LHCb MC sample for the $D^+ \rightarrow K^-K^+\pi^+$ decay after all selection criteria requiring TIS with respect to the L0 muon, electron, photon and hadron lines using both magnet polarities.

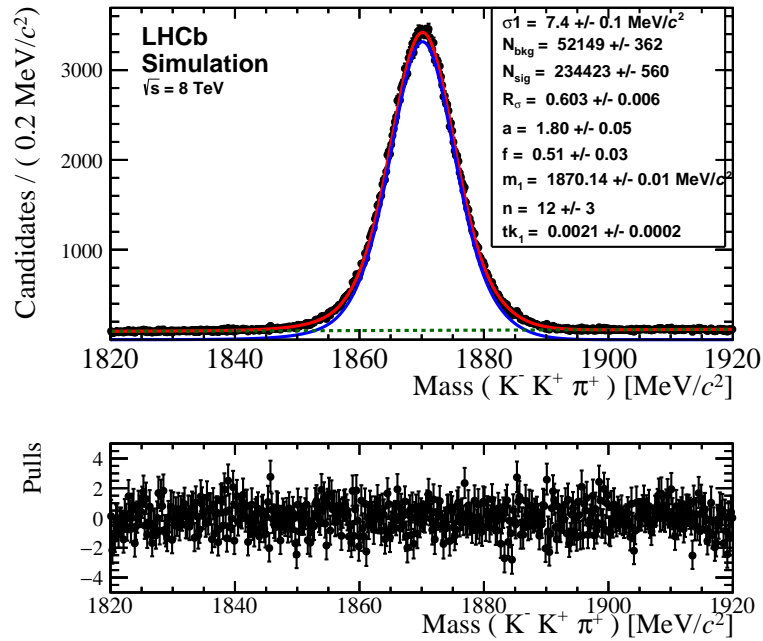


Figure 7.21: $K^-K^+\pi^+$ mass fit of the LHCb MC sample for the $D^+ \rightarrow K^-K^+\pi^+$ decay after all selection criteria, using both magnet polarities.

obtained distribution can be seen in figures 7.22, 7.23 and 7.24 for the left sideband, right sideband and the combination of both, respectively.

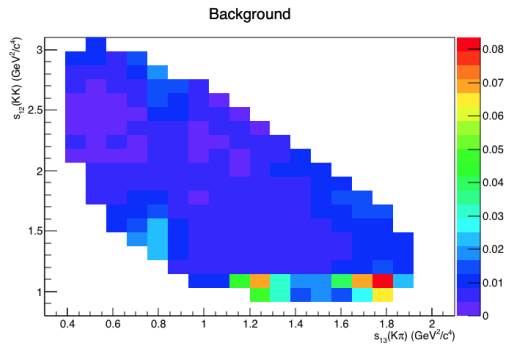


Figure 7.22: Background Dalitz distribution of the left mass sideband ($1820 < M_D < 1840 \text{ MeV}/c^2$).

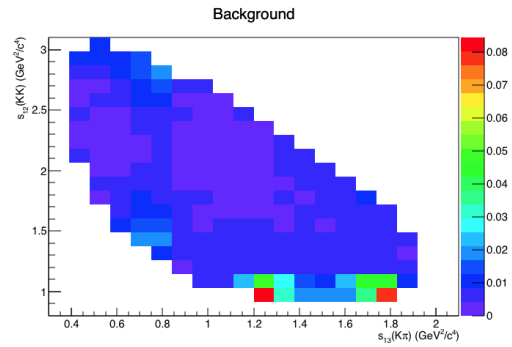


Figure 7.23: Background Dalitz distribution of the right mass sideband ($1900 < M_D < 1920 \text{ MeV}/c^2$).

The background Dalitz plot shows clear signs of angular distributions over the ϕ and $K^*(892)$ regions. Contributions from combinatorial background, or incoherent components composed by $\phi+\pi$, $K^*(892)+K$, etc., are less relevant. We have on both sidebands contributions from the $D_s^+ \rightarrow K^-K^+\pi^+$ radiative tail, as shown in figure 7.11, which is capable of producing the angular distribution pattern, although it has

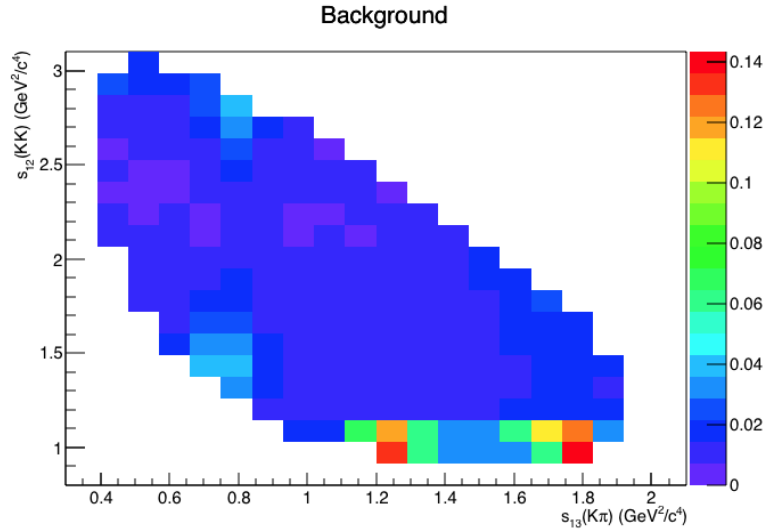


Figure 7.24: Background Dalitz distribution of the combination of both sidebands ($1820 < M_D < 1840 \text{ MeV}/c^2$ and $1900 < M_D < 1920 \text{ MeV}/c^2$)

higher impact on the right sideband. The left sideband contains a contribution of the decay $D_s^+ \rightarrow K^- K^+ \pi^+ \pi^0$, where the π^0 is lost, which can also provide the angular distribution pattern. Appendix C presents the Dalitz distribution in $5 \text{ MeV}/c^2$ windows, showing the presence of contributions with angular distribution even far away from the D^+ mass peak.

The combined distribution is fed into a histogram and smoothed with a 2D cubic spline in, providing a high resolution histogram. The final histogram can be seen at 7.25 and it is included in the fit model as a background component, with fraction defined by the mass fit.

7.6 Signal Dalitz Distribution

The large samples provided by LHCb enable the study of the Dalitz distribution of the $D^+ \rightarrow K^- K^+ \pi^+$ decay in detail. Figure 7.26 shows the Dalitz plot of the TOS data sample, using events within the $1858.3 < M_D < 1883.0 \text{ MeV}/c^2$ range. This is the sample to be used in the fits, since it presents a better behaved efficiency, as will be shown on the next chapter.

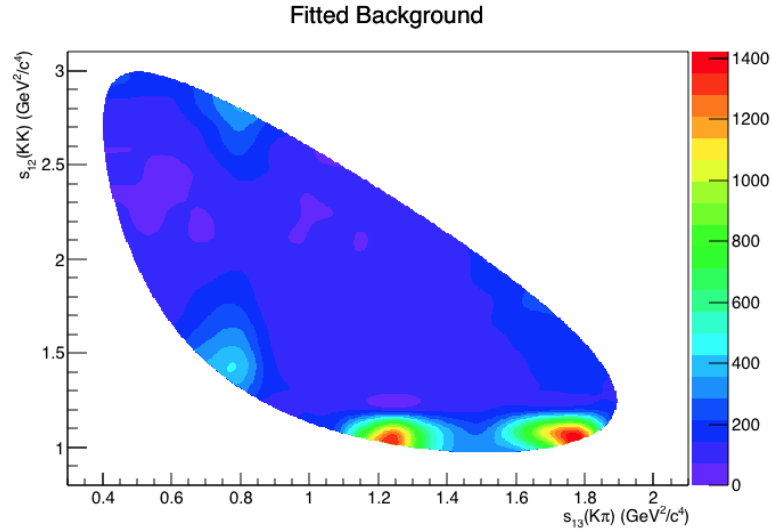


Figure 7.25: High resolution background Dalitz histogram of the combination of both sidebands ($1820 < M_D < 1840 \text{ MeV}/c^2$ and $1900 < M_D < 1920 \text{ MeV}/c^2$), with TOS requirement with respect to the L0 hadron trigger line.

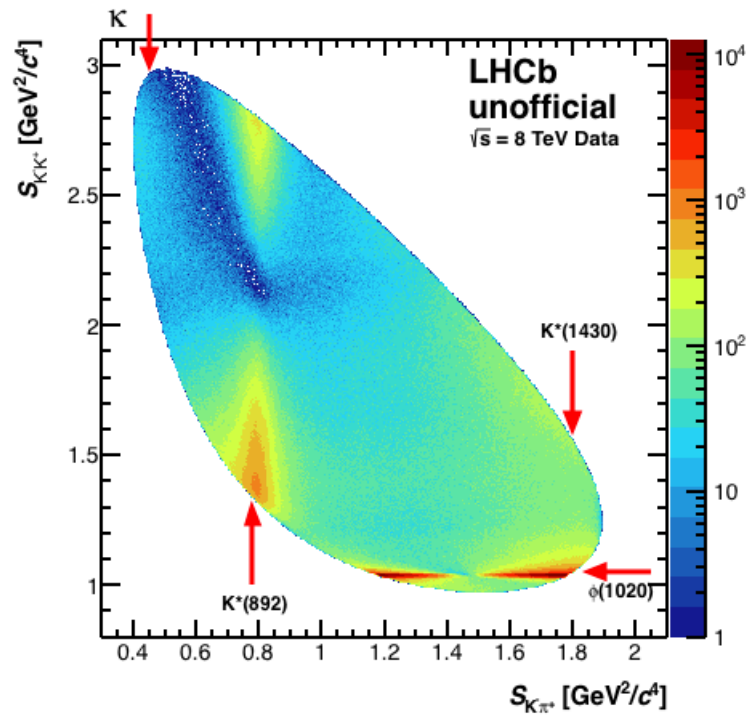


Figure 7.26: Dalitz plot of the $D^+ \rightarrow K^- K^+ \pi^+$ decay with LHCb 2012 TOS sample within the $2 \sigma_{eff}$ mass window.

The Dalitz plot of the $D^+ \rightarrow K^- K^+ \pi^+$ decays contain as main contributions the $\phi(1020)$, the $K^*(892)$ and $K^*(1430)$ resonances. Other contributions are less visible, but a good fit may unveil the complete resonant structure in this decay.

Chapter 8

Efficiency

The selection efficiency variation across the phase space may have a large impact on the Dalitz plot distribution. It is important, for that reason to consider selection criteria as uniform as possible. The efficiency variation function must be taken into account when calculating the model PDF. If the acceptance has intense fluctuations it will be more difficult to describe it and, therefore, stronger systematic effects will be introduced.

The efficiency function is built within a few steps. The efficiency due to the LHCb geometrical acceptance, reconstruction and selection is obtained with a LHCb MC sample, after applying all selection criteria, except the particle identification (PID), because it is not well described in the simulated events. The PID efficiency is extracted from calibration samples to be later included.

Large MC samples are desired in order to obtain the most possible precise description of the efficiency. To minimize the statistical fluctuation, the efficiency acceptance function is fed into a histogram and smoothed with a 2D cubic spline function, The efficiency histogram must be divided by a flat toy MC sample in order to avoid the distribution to be distorted in border bins, which are not fully inside the phase space. The result is used in Rio+ package as described in chapter 6. A single efficiency function is evaluated for the full 2012 sample.

8.1 Geometrical Acceptance, Reconstruction and Selection Efficiencies

In order to evaluate the full efficiency ϵ_0 , with no corrections so far, as a function of the Dalitz plot position (s_{12}, s_{13}) , we use a LHCb MC sample of the $D^+ \rightarrow K^- K^+ \pi^+$ decay, generated flat across the phase space. By simulating data acquisition, reconstruction and applying selection criteria to this sample, it is possible to obtain the combined efficiency for the entire process.

PID cuts are left out of the criteria. The PID selection is not applied at this stage, and its efficiency will be taken into account in the next step, as described in section, as described in section 8.2. The efficiency function $\epsilon_0(s_{12}, s_{13})$ obtained after this process can be seen in figure 8.1.

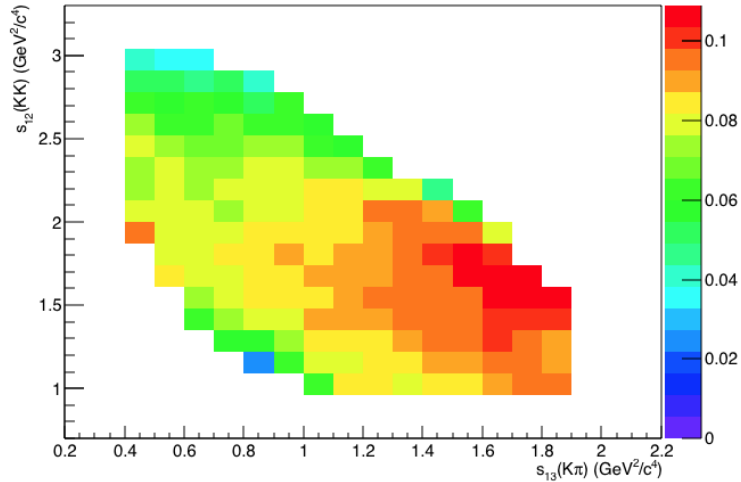


Figure 8.1: Efficiency histogram for our sample, after simulating data acquisition, reconstruction and applying all selection criteria, but without including PID.

The L0 trigger presents non-uniform efficiencies and, in order to evaluate its variation across the Dalitz plot, we must inspect distinct trigger requirements. The efficiencies requiring TOS with respect to the L0 hadron trigger line is shown in figure 8.2, while requiring TIS with respect to the L0 muon, electron, photon and hadron lines can be seen in figure 8.3. Both trigger requirements introduce strong

efficiency effects, but the TOS sample presents a more uniform efficiency. Therefore, we choose the TOS sample to perform the fits, keeping the TIS to study the impact of this choice.

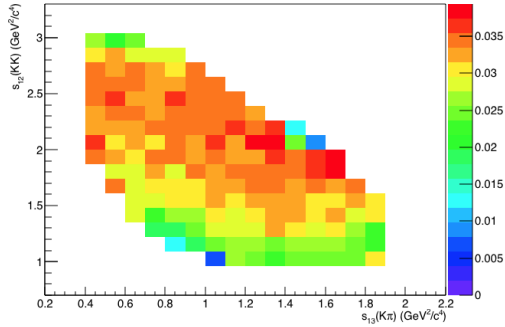


Figure 8.2: Efficiency histogram for our sample, after simulating data acquisition, reconstruction and applying all selection criteria, including the TOS requirement with respect to the L0 hadron trigger line, without including PID efficiency.

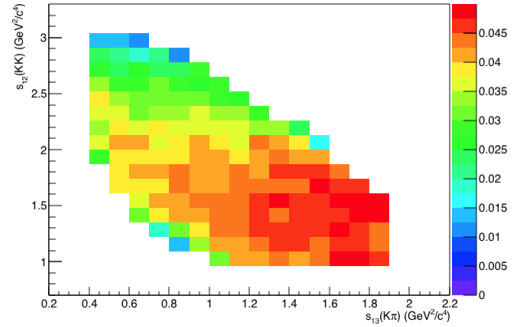


Figure 8.3: Efficiency histogram for our sample, after simulating data acquisition, reconstruction and applying all selection criteria, including the TIS requirement with respect to the L0 muon, electron, photon and hadron trigger lines, without including PID efficiency.

8.2 PID Efficiency

Particle identification efficiencies present different behaviors in data and MC. In order to use the correct efficiencies, the PID cut is left out of the efficiency ϵ_0 . The correct efficiencies are obtained from calibration samples separately for Kaons and pions. This is done using the PIDCalib tool. Efficiencies of tracks of $D^* \rightarrow D^0(K\pi)\pi$ samples are recorded in bins in p , η and track multiplicity.

PIDCalib gives each daughter track a data driven efficiency, considering the momenta of the track, the track multiplicity in the event and the given PID cut value. The event efficiency is given by the product of the efficiency of each of the daughters. The correct PID efficiency can be given in an event-by-event weight when filling ϵ_0 histogram. The efficiency histogram before and after PID corrections, after applying all selection criteria including the TOS requirement with respect to the L0

hadron trigger line, can be seen at figures 8.1 and 8.4, respectively.

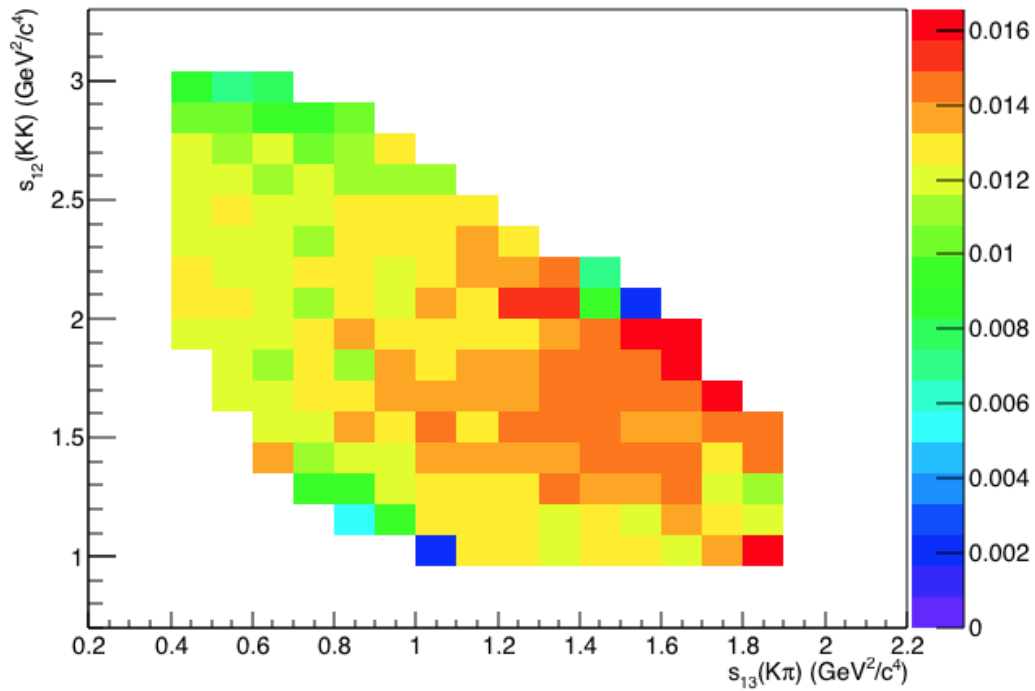


Figure 8.4: Efficiency histogram for our sample, after simulating data acquisition, reconstruction and applying all selection criteria and PID efficiency, including the TOS requirement with respect to the L0 hadron trigger line.

8.3 Final Efficiency

The distribution of the LHCb MC sample after simulating data acquisition, reconstruction, selection and applying all corrections gives our final efficiency. A high resolution histogram is created using a 2D cubic spline smooth on the final efficiency in order to obtain the most precise description of the efficiency possible, to be used in the fit. the final efficiency histogram can be seen at figure 8.5.

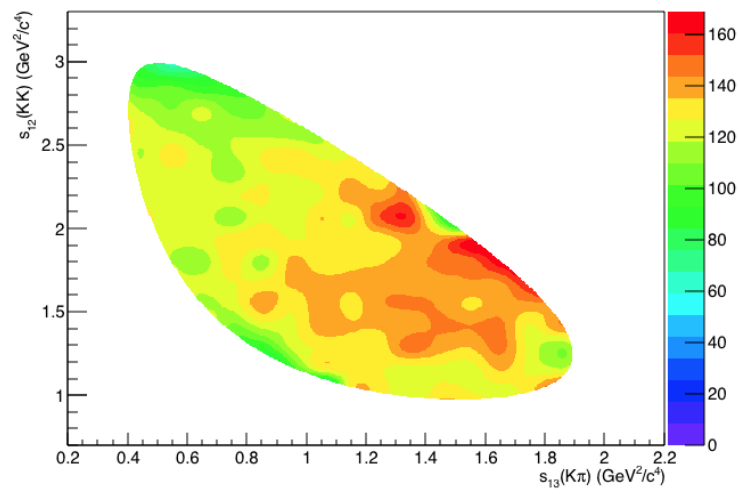


Figure 8.5: High resolution histogram of the efficiency for our channel considering data acquisition, reconstruction and selection effects, with PID correction.

Chapter 9

Fit Model and Results

In order to achieve the best isobar fit possible it is necessary to compare several distinct models. Different resonant contributions and lineshapes can be tested. Parameters, such as the mass and width of each resonance, may also be changed. In this chapter we describe the models used, the strategy used and the results.

9.1 Fit Models

The fit models for our analysis are inspired in the ones obtained in previous analyses, made by CLEO [56] and BaBar [57] collaborations. The models are based on the sum of several resonant contributions, given by the isobar model in eq. 5.15. Most resonant channels are described by the relativistic Breit-Wigner formulation, with exception of the $f_0(980)$, which is described by a Flattée, the κ , which is tested as a pole function or as a Breit-Wigner with constant width, and the non-resonant contribution, defined as a constant. The non-resonant (NR) component is represented as a constant, providing a flat distribution.

The resonant parameters, such as the resonance mass and width, are taken mostly from PDG [38]. The pole mass for κ is taken from reference [56], while g_K , g_π and mass values for $f_0(980)$ are taken from a BES analysis [63]. The $f_0(X)$ is a broad resonant state in the KK system proposed in both BaBar and CLEO models. It

is represented through the standard Breit-Wigner formulation. The nature of this state is not completely clear and it is placed on a region with several other S-wave resonances, mixing up the amplitudes and complicating the measurement of each individual contribution. A summary of resonance parameter values and references can be found at 9.1.

The resulting distribution of each individual resonant channel can be seen at appendix E.

We use as primary model one containing the resonances presented in the CLEO analysis. We run several fits, each adding a distinct resonance, and we pick the one which brings the most significant improvement to the maximum log likelihood. We repeat this procedure until all significant contributions are added. The masses and widths of resonances are fixed to the values shown in table 9.1, unless otherwise stated.

The composition of each presented model is summarized in table 9.2 and the models are labeled from 1 to 4. These are, among all models tested, the ones that bring the most relevant information. The detail and justification of each model is discussed below.

9.2 Fit Results

Several models were tested. In order to evaluate the fit quality and choose the best models we compare the FCN value, defined as $FCN = -2 \log \mathcal{L}$. The lower this value is, the larger the likelihood becomes and, therefore, the better the fit is. In parallel, we fill a histogram with a flat toy MC sample, weighting each entry with the corresponding PDF value. The obtained histogram is a “binned PDF”. We calculate the χ^2 , defined by:

$$\chi_{Tot}^2 = \sum_{i=0}^{i=N_{bins}} \chi_i^2 = \sum_{i=0}^{i=N_{bins}} \frac{(N_{PDF_i} - N_{Data_i})^2}{N_{Data}} \quad (9.1)$$

Resonance	Mass (GeV)	Width (GeV)	Other Parameters	Source
D	1.86962	-	-	PDG [38]
$K^*(892) + K$	0.89581	0.0474	-	PDG [38]
$K^*(1430) + K$	1.425	0.270	-	PDG [38]
$\phi(1020) + \pi$	1.019461	0.004266	-	PDG [38]
$a_0(1450) + \pi$	1.474	0.265	-	PDG [38]
$K_2^*(1430) + K$	1.4324	0.109	-	PDG [38]
$\phi(1680) + \pi$	1.680	0.150	-	PDG [38]
$\kappa(BW) + K$	0.797	0.410	-	E791 [51]
$\kappa(\text{pole}) + K$	-	-	$M_{\text{pole}} = 0.71 - i0.31 \text{ GeV}$	CLEO [56]
$f_0(980) + \pi$	0.965	-	$g_\pi = 0.165 \text{ GeV}, g_K = 0.695 \text{ GeV}$	BES [63]
$f_0(X) + \pi$	1.435	0.135	-	PDG [38]
$f_0(1500) + \pi$	1.504	0.109	-	PDG [38]
$K_1^*(1410) + K$	1.414	0.232	-	PDG [38]
$a_2(1320) + \pi$	1.3183	0.107	-	PDG [38]
$f_2(1270) + \pi$	1.2755	0.1867	-	PDG [38]
$K^*(1680) + K$	1.717	0.322	-	PDG [38]
$f_2'(1525) + \pi$	1.525	0.073	-	PDG [38]
$f_0(1710) + \pi$	1.723	0.139	-	PDG [38]

Table 9.1: Resonant parameters used in the fit.

Resonant Channel	Model 1	Model 2	Model 3	Model 4
$K^*(892) + K$	✓	✓	✓	✓
$K^*(1430) + K$	✓	✓	✓	✓
$\phi(1020) + \pi$	✓	✓	✓	✓
$a_0 + \pi$	✓	✓	✓	-
$K_2^*(1430) + K$	✓	✓	✓	✓
$\phi(1680) + \pi$	✓	✓	✓	✓
$\kappa(BW) + K$	-	✓	✓	✓
$\kappa(pole) + K$	✓	-	-	-
$f_0(980) + \pi$	-	-	✓	✓
$f_0(X) + \pi$	-	-	✓	✓✓
$f_0(1500) + \pi$	-	-	✓	✓
$K_1^*(1410) + K$	-	-	✓	✓
$a_2(1320) + \pi$	-	-	✓	✓
$f_2(1270) + \pi$	-	-	✓	✓
$K^*(1680) + K$	-	-	✓	-
NR	-	-	✓	-
$f_2'(1525) + \pi$	-	-	✓	-
$f_0(1710) + \pi$	-	-	✓	✓

Table 9.2: Summary of model composition. Elements marked with ✓ are included in the corresponding model, with ✓✓ are included with floating mass and width and with - are not included.

where N_{bins} is the number of bins in the histogram, $N_{PDF(Data)_i}$ is the PDF (data) content in the i^{th} bin. For this comparison we use a histogram with 50×50 uniform bins providing around 1150 occupied bins. Defining the Number of Degrees Of Freedom (NDOF) as:

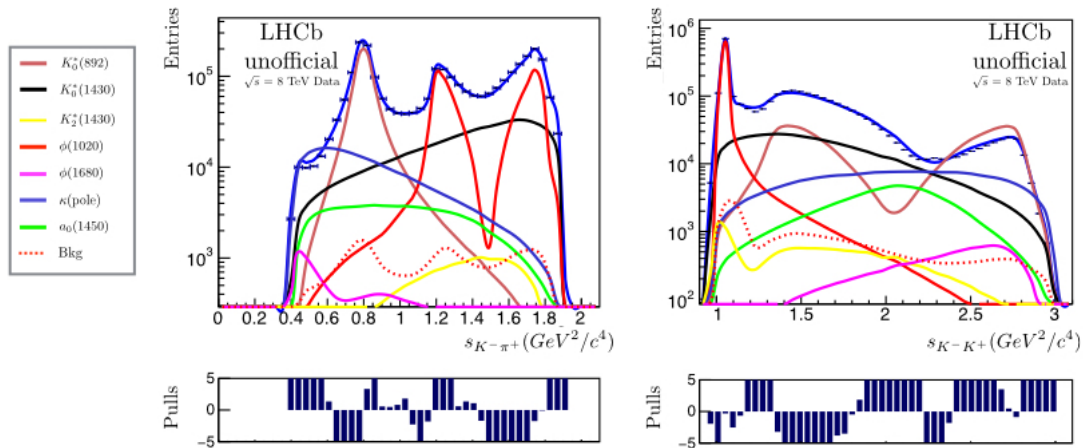
$$NDOF = N_{bins} - N_{pars} - 1$$

where N_{pars} is the number of free parameters in the fit, we can check the fit quality through the $\chi^2/NDOF$ ratio or calculating the corresponding p-value. The χ_i^2 histogram also brings important information of where discrepancies between the model and the data may arise, but is less stable than the FCN value, since it depends on the binning. The pulls, defined as the difference between the PDF and the data distribution, divided by the corresponding error, in each bin of the projections over the s_{K-K^+} , $s_{K-\pi^+}$ and $s_{K+\pi^+}$, also provide information about the fit quality across the phase space.

Resonance	Real	Imag.	Fraction (%)
$K^*(892) + K$	1 ± 0	0 ± 0	23.82 ± 0.07
$K^*(1430) + K$	-0.48 ± 0.04	4.96 ± 0.01	21.9 ± 0.2
$\phi(1020) + \pi$	-1.141 ± 0.002	-0.388 ± 0.004	28.76 ± 0.06
$a_0(1450) + \pi$	-0.487 ± 0.005	1.197 ± 0.006	3.30 ± 0.06
$\kappa(\text{pole}) + K$	-0.42 ± 0.01	-2.72 ± 0.01	9.2 ± 0.2
$K_2^*(1430) + K$	-3.16 ± 0.04	0.98 ± 0.03	0.61 ± 0.03
$\phi(1680) + \pi$	-0.71 ± 0.02	-1.60 ± 0.01	0.42 ± 0.01
Total Fit Fraction			87.98

Table 9.3: Fit results for model 1.

Starting with the resonant channels provided in the CLEO analysis, labeled model 1, we fit the full 2012 LHCb data sample for the $D^+ \rightarrow K^- K^+ \pi^+$ decay, after all selection criteria, requiring TOS with respect to the L0 Hadron line and $1858.3 < M_D < 1883.0$. The fit results are shown in table 9.3 and in figures 9.1 and 9.2.

Figure 9.1: Data distribution, PDF and resonant contributions provided in model 1 projected over the $s_{K-\pi^+}$ axis, on the left, and over the s_{K-K^+} axis on the right.

Although a first look at the projections shows that the fit with the CLEO model makes sense, the fit quality is not good. We obtained $\chi_{Tot}^2/NDOF = 21.14$, with $FCN = -3181000$. Fit fractions are not in agreement with the ones obtained in the CLEO analysis.

As a first modification to the CLEO model, labeled model 2, a Breit-Wigner

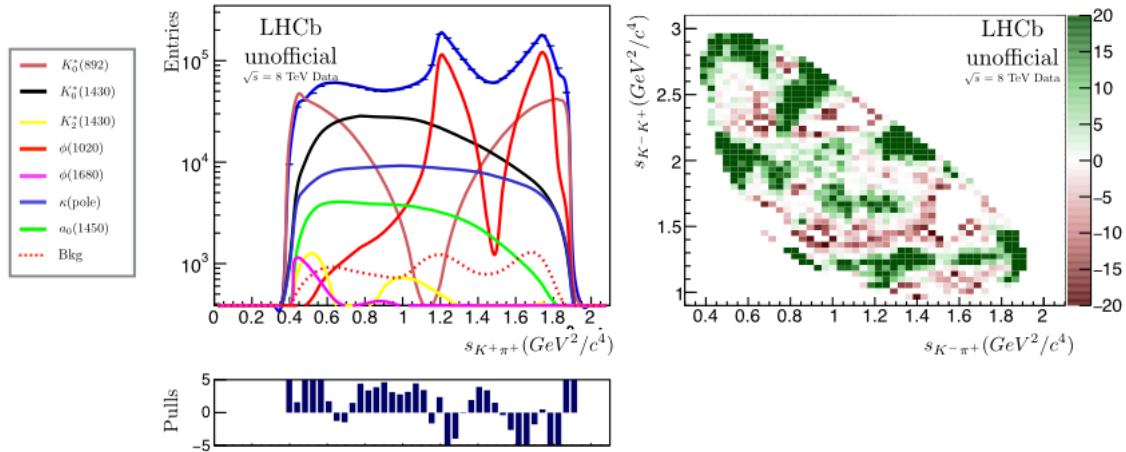


Figure 9.2: Data distribution, PDF and resonant contributions provided in model 1 projected over the $s_{K^+\pi^+}$ axis, on the left, and the corresponding χ^2_i distribution on the right.

formulation with constant width was used for the $\kappa + K$ resonant channel, instead of the pole function, and results are presented in figures 9.3, 9.4 and table 9.4. A small improvement with respect to the fit quality, compared to the previous fit, is seen. We obtained the $\chi^2_{Tot}/NDOF$ ratio of $\chi^2_{Tot}/NDOF = 17.73$, with a variation in the FCN value (ΔFCN) with respect to model 1 of -3807. This lineshape was chosen for the following fits.

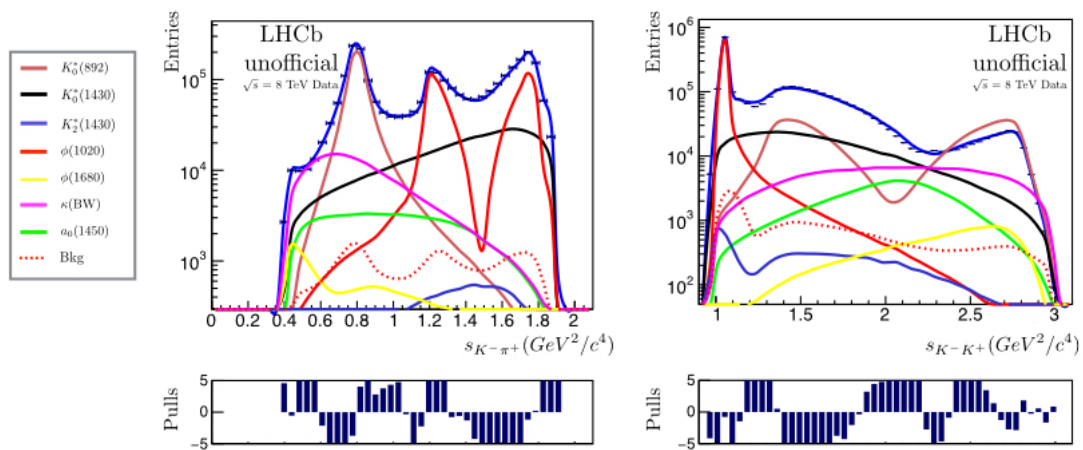


Figure 9.3: Data distribution, PDF and resonant contributions of the fit with model 2, projected over the $s_{K^-\pi^+}$ axis, on the left, and over the $s_{K^-\pi^+}$ axis on the right.

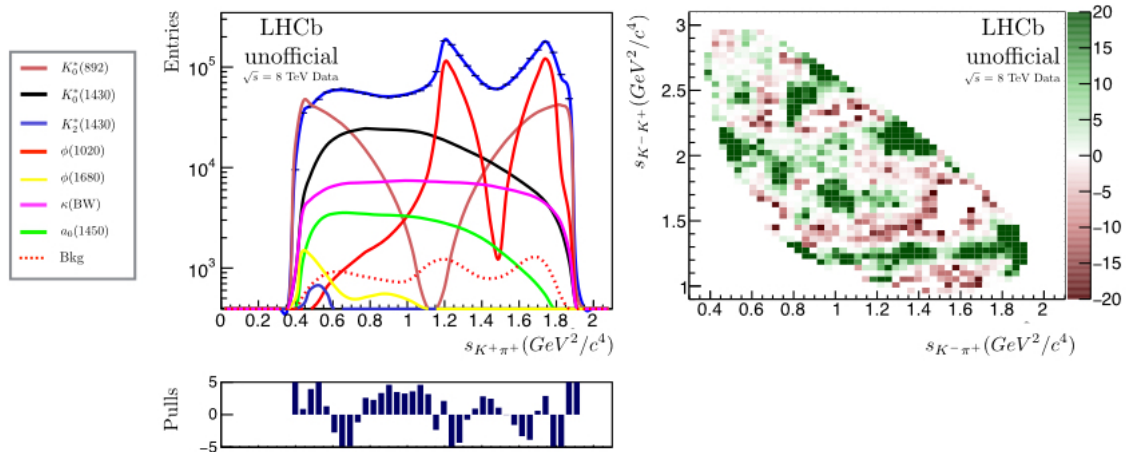


Figure 9.4: Data distribution, PDF and resonant contributions of the fit with model 2 projected over the $s_{K+\pi^+}$ axis, on the left, and the corresponding χ^2_i distribution on the right.

Resonance	Real	Imag.	Fraction (%)
$K^*(892) + K$	1 ± 0	0 ± 0	24.04 ± 0.06
$K^*(1430) + K$	-0.17 ± 0.03	4.596 ± 0.009	18.8 ± 0.1
$\phi(1020) + \pi$	-1.146 ± 0.002	-0.360 ± 0.004	28.85 ± 0.06
$a_0(1450) + \pi$	-0.592 ± 0.004	1.047 ± 0.006	2.89 ± 0.06
$K_2^*(1430) + K$	-2.02 ± 0.05	1.32 ± 0.03	0.33 ± 0.02
$\phi(1680) + \pi$	-0.09 ± 0.02	-1.99 ± 0.01	0.54 ± 0.01
$\kappa(BW) + K$	0.472 ± 0.006	-1.669 ± 0.009	7.8 ± 0.1
Total Fit Fraction			83.23

Table 9.4: Fit results for the CLEO model with model 2.

Next, we tested including all resonances within the BaBar model that were not in the fit yet, individually. Picking the fit which provided the best FCN value, we started another round with all remaining resonances, picking the best alternative. By repeating this process until all resonances were included, reaching what we call model 3, we were able to evaluate the relevance of each contribution and understand better their behavior. The final result, including all resonances, is shown in table 9.5 and in figures 9.5 and 9.6. The seven first resonant channels in table 9.5 are the ones within CLEO model and the remaining follow the order of inclusion in the fit considering the given strategy.

The quality improved significantly including these other contributions. The

Resonance	Real	Imag.	Fraction (%)
$K^*(892) + K$	1 ± 0	0 ± 0	22.0 ± 0.1
$K^*(1430) + K$	-1.18 ± 0.09	4.97 ± 0.07	21.2 ± 1.3
$\phi(1020) + \pi$	-1.11 ± 0.01	-0.57 ± 0.02	28.67 ± 0.08
$a_0(1450) + \pi$	-0.37 ± 0.06	3.51 ± 0.06	22 ± 1
$K_2^* + K$	-0.99 ± 0.09	0.77 ± 0.08	0.08 ± 0.01
$\phi(1680) + \pi$	0.62 ± 0.04	-2.63 ± 0.02	0.92 ± 0.03
$\kappa(BW) + K$	0.53 ± 0.02	-1.04 ± 0.03	3.2 ± 0.3
$f_0(1500) + \pi$	0.09 ± 0.01	-0.57 ± 0.01	1.6 ± 0.2
$f_2(1270) + \pi$	0.36 ± 0.03	0.12 ± 0.02	0.07 ± 0.02
$K_1^*(1410) + K$	-1.91 ± 0.09	0.83 ± 0.06	0.8 ± 0.1
$f_0(980) + \pi$	-0.85 ± 0.07	1.46 ± 0.04	2.63 ± 0.4
$f_0(X) + \pi$	-0.04 ± 0.02	-0.42 ± 0.02	0.8 ± 0.1
$f_0(1710) + \pi$	0.02 ± 0.04	0.38 ± 0.02	0.14 ± 0.03
$a_2(1320) + \pi$	0.24 ± 0.01	0.10 ± 0.01	0.07 ± 0.01
$K^*(1680) + K$	7.0 ± 0.5	5.1 ± 0.3	13 ± 2
NR	1.4 ± 0.3	-1.9 ± 0.1	3.1 ± 0.8
$f_2'(1525) + \pi$	-0.04 ± 0.01	-0.04 ± 0.01	0.001 ± 0.001
Total Fit Fraction			120.645

Table 9.5: Fit results for model 3. The first 7 resonant channels are the contributions given in the CLEO model, while the remaining resonances follow the order of addition to the fit model.

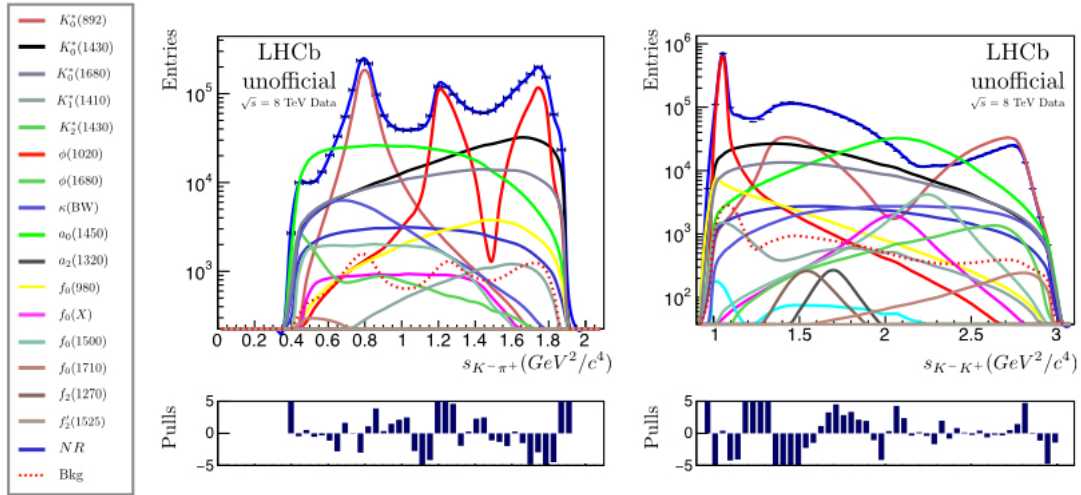


Figure 9.5: Data distribution, PDF and resonant contributions of the fit with model 3 projected over the $s_{K-\pi^+}$ axis, on the left, and over the s_{K-K^+} axis on the right.

ΔFCN variation with respect to model 1 was -17740 and the $\chi_{Tot}^2/NDOF$ ratio was 8.57. On the other hand, the significance of some of these contributions is arguable. Resonant channel $f_2'(1525) + \pi$ has a very small fraction in this fit, when

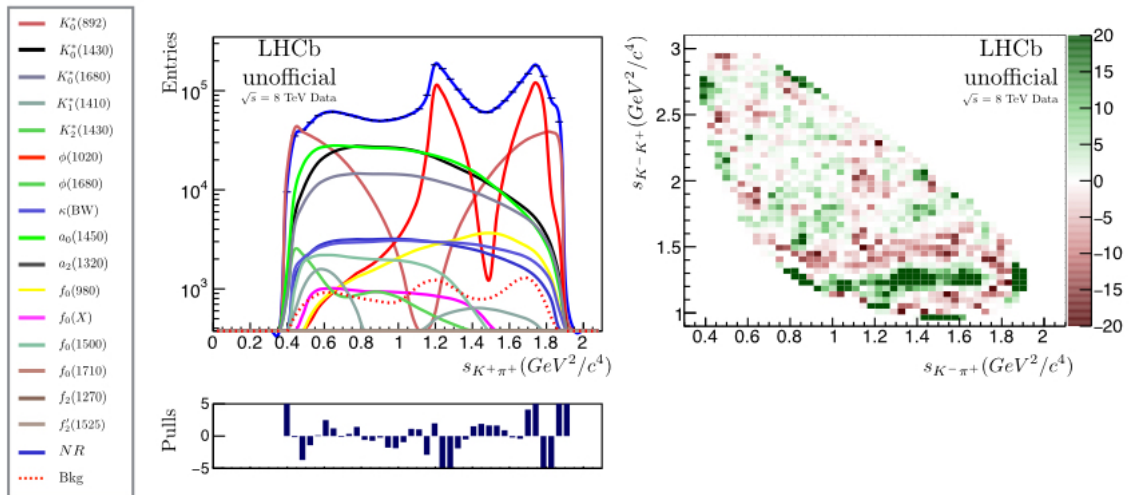


Figure 9.6: Data distribution, PDF and resonant contributions of the fit with model 3 projected over the $s_{K+\pi^+}$ axis, on the left, and the corresponding χ^2_i distribution on the right.

compared to the corresponding error. The $K_0^*(1680) + K$ and NR contributions affect the entire phase space and gain an artificially high fraction through interferences with other resonances, most likely to compensate an imperfection of the model. Finally, the large number of KK S-wave resonances populating the region $1.4 < m_{KK} < 1.8\text{GeV}/c^2$, give the $a_0(1450) + \pi$, which is expected to be a small contribution due to the isospin suppression, an extremely high fraction also through interference effects. The $a_0(1450)$ can be replaced by $f_0(X)$ contribution, with free mass and width. This way we get a better description of the existing resonance in that region, associated with a more plausible contribution.

Finally, we obtain what we call model 4 by removing the contributions with questionable significance. Moreover, we set the mass and width of the $f_0(X) + \pi$ contribution as free parameters in an effort to better describe the KK resonant channels in that region. The fit results show a small loss in fit quality, with $\Delta FCN = -17650$ and $\chi^2_{Tot}/NDOF = 8.60$. The obtained mass and width for the $f_0(X)$ were $1.372 \pm 0.006\text{GeV}/c^2$ and $0.385 \pm 0.005\text{GeV}/c^2$, respectively. The results are shown on table 9.6 and in figures 9.7 and 9.8.

This result presents significant contributions from both $f_0(1500) + \pi$ and $f_0(1710) +$

Resonance	Real	Imag.	Fraction (%)
$K^*(892) + K$	1 ± 0	0 ± 0	22.2 ± 0.1
$K^*(1430) + K$	0.47 ± 0.06	4.46 ± 0.04	16.5 ± 0.6
$\phi(1020) + \pi$	-1.100 ± 0.009	-0.59 ± 0.01	28.7 ± 0.1
$K_2^* + K$	-0.53 ± 0.08	0.6 ± 0.05	0.032 ± 0.008
$\phi(1680) + \pi$	1.39 ± 0.04	-2.85 ± 0.02	1.27 ± 0.04
$\kappa(BW) + K$	0.22 ± 0.01	-1.40 ± 0.02	4.8 ± 0.2
$f_0(1500) + \pi$	-0.056 ± 0.01	-0.144 ± 0.008	0.11 ± 0.02
$f_2(1270) + \pi$	0.51 ± 0.01	0.11 ± 0.02	0.14 ± 0.02
$K_1^*(1410) + K$	-2.28 ± 0.06	0.89 ± 0.04	1.0 ± 0.1
$f_0(980) + \pi$	-0.15 ± 0.07	1.43 ± 0.04	1.9 ± 0.2
$f_0(X) + \pi$	1.77 ± 0.08	1.48 ± 0.12	7.5 ± 0.7
$f_0(1710) + \pi$	0.21 ± 0.02	-0.23 ± 0.03	0.10 ± 0.02
$a_2(1320) + \pi$	0.22 ± 0.01	0.02 ± 0.01	0.049 ± 0.009
Total Fit Fraction			84.284

Table 9.6: Fit results for model 4. The first 6 resonant channels are the contributions given in the CLEO model, with exception of the $a_0(1450)$ that was removed, while the remaining resonances follow the order of addition to the fit model.

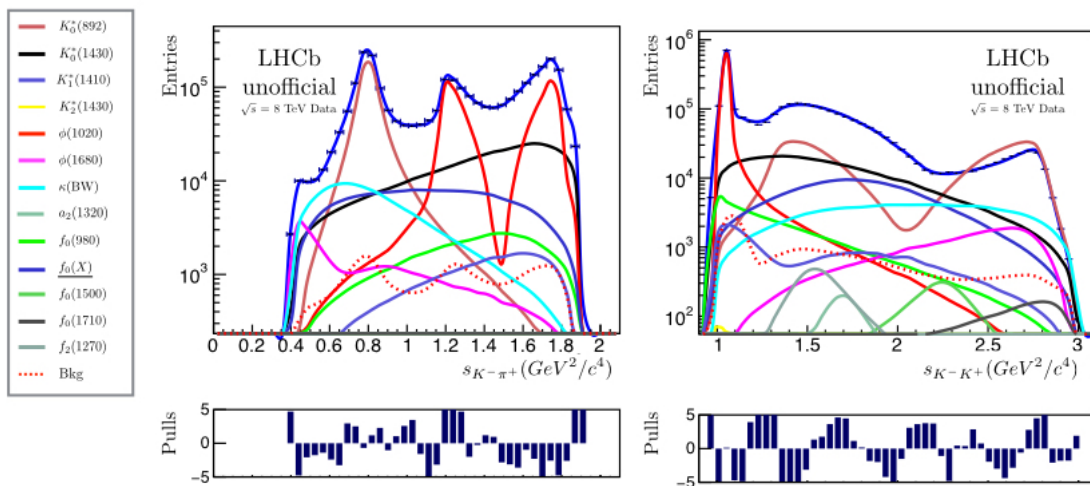


Figure 9.7: Data distribution, PDF and resonant contributions of the fit model 4, where resonant contributions with free mass and widths are underlined in the legends, projected over the $s_{K-\pi^+}$ axis, on the left, and over the s_{K-K^+} axis on the right.

π , pointing towards the scenario with only three contributions to the KK S-wave within the $1.3 < m_{KK} < 1.8\text{GeV}/c^2$ mass range. We end with a stable fit, with conceptually strong contributions and very little gain with any reasonable additional resonant channels. The obtained mass and width for the $f_0(X)$ resonance are at the

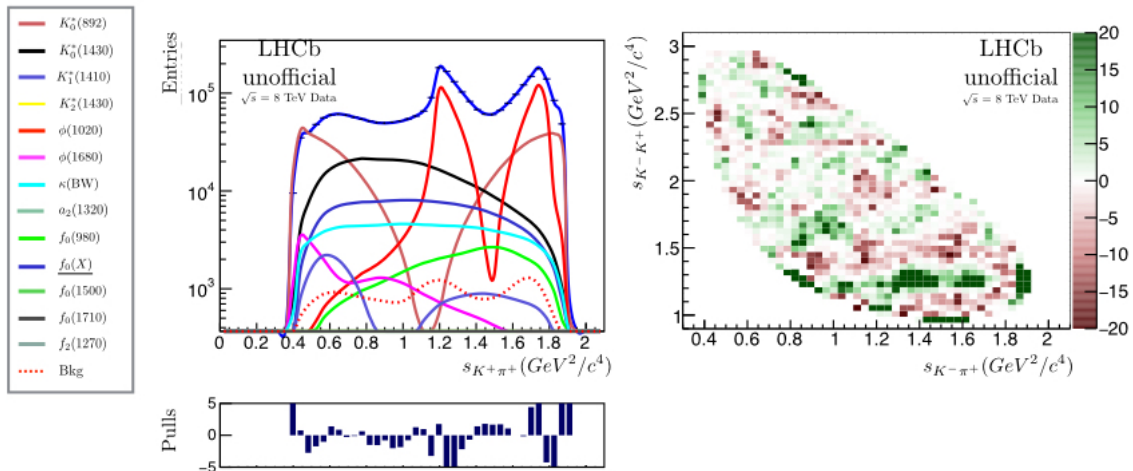


Figure 9.8: Data distribution, PDF and resonant contributions of the fit model 4, where resonant contributions with free mass and widths are underlined in the legends, projected over the $s_{K^+\pi^+}$ axis, on the left, and the corresponding χ^2_i distribution on the right.

same order of magnitude of the ones obtained by the BaBar collaboration for the $a_0(1450)$, indicating one more time that these are the same state. None of the fits provide an acceptable fit quality, the most critical region being around $S_{KK} \approx 1.3$, where the PDF exceeds the data by far. Other improvements could be made testing other formulations which include FSI effects, but the intrinsic limitations of the isobar model are probably the main obstacle to overcome in order to obtain a good description of the data distribution.

In this context, the PWA is an alternative. In this model all decay dynamics, including FSI, are fitted in a single complex function, without making any assumption on the effects in action. On the other hand, even though the fit quality is expected to improve, a physical interpretation of the fit is not immediate and would require further work. We have reached a point where the isobar model limitations are too significant to obtain a good fit by itself, but these results will be used as an input to a PWA and a better description will be obtained.

Chapter 10

Discussion on Systematic Errors

The Dalitz plot analysis involve several steps and systematic effects may be introduced in each one. Systematic uncertainties were not estimated for this thesis, but possible sources are discussed in this chapter. Systematic uncertainties can be separated in two classes: experimental uncertainties, related to the detection, reconstruction, selection and $K^-K^+\pi^+$ mass fits, and the uncertainties on The Dalitz plot fit model, related to the choices of which resonant contributions are included and their corresponding representation.

Experimental systematic errors include uncertainties due to the $K^-K^+\pi^+$ mass fit, to the efficiency variation across the Dalitz plot, to the background description used in the fit and to the 2-body mass resolution. The $K^-K^+\pi^+$ mass fit contain uncertainties on the fit parameters and signal over background ratio. Aiming at the evaluation of the effect introduced by each of these sources, we can perform Dalitz plot fits varying these parameters within their corresponding errors. The variation of fit results define, then, the corresponding systematic error.

Likewise, each bin of the efficiency histogram contain an statistical error associated with it. The choice between TIS or TOS with respect to the L0 hadron trigger line also affects drastically the efficiency function. The systematic errors associated with the uncertainties in the efficiency histogram, including the errors on the PID

efficiency, can be evaluated by varying each bin value within the corresponding error and repeating the fit. The systematic related to the L0 trigger efficiency can be determined by comparing fit results from TOS and TIS-not-TOS independent samples. Likewise, the trigger configurations had small modifications during the data acquisition and making the fits dividing the data in run periods can provide us the corresponding systematic uncertainties.

The background description is taken from the combination of both sidebands, but this choice might not accurately represent the distribution of the background under the D^+ mass peak. Considering the background fraction is around 1% this should be a minor effect, but it can be evaluated repeating the fit without background, taking the distribution only from the left sideband and taking the distribution only from the right sideband. The differences in fit results would then give the systematic effects related to this choice.

Besides that, the 2-body mass resolution is not negligible. We have a resolution of $0.004 \text{ GeV}^2/c^4$ on the s_{K-K^+} axis and $0.003 \text{ GeV}^2/c^4$ on the $s_{K-\pi^+}$ axis. This is particularly relevant on the s_{K-K^+} axis, considering the large contribution of $\phi(1020)$, a very narrow state. One alternative to this problem is numerically calculating the convolution of the PDF with a Gaussian, but this would increase the fit processing time drastically. Another approach might be to analytically convolve the Gaussian with the amplitude functions. This is an ongoing study. If this effect cannot be included in the fit, a systematic error must be associated with it. This can be done by simulating a toy MC sample and smearing it according to the mass resolution. Having a large number of smeared samples, fitting each sample and taking into account the average fluctuation in each parameter will provide the systematic error.

The systematic errors related to the fit model can be evaluated by testing different models. Taking into account fits with different formulations and testing different contributions, specially the less significant ones, and evaluating the fluctuation in

fit parameters, provides us with the systematic uncertainties associated with these effects. Resonance parameters, such as masses, widths and other parameters that are fixed during fits, such as those from the form factors and coupling constants, are also a possible source of systematics and varying those values in the fits can give us the corresponding systematic error.

Chapter 11

Conclusion

This thesis presents a contribution to the VELO upgrade, with the simulation tests of the RF foil, and the Dalitz plot analysis of the $D^+ \rightarrow K^- K^+ \pi^+$ decay, using the isobar model.

The LHCb upgrade is planned to occur during the next LS, in 2018 and 2019, and it is crucial for acquiring data under a higher luminosity regime, expanding the potential and lifetime of the experiment. The VELO upgrade is vital in this context. With a new detector design, the RF foil had to be adapted to attend the upgrade demands.

Taking into consideration all operational requirements of the RF foil, it would be of great benefit improving its performance, since it has the largest material contribution in VELO. This thesis presents simulation studies of the RF foil, where partially thinned foils are tested. This work included a translation of the foil generation algorithm and the simulation of several foil designs, evaluating the corresponding IP resolution for each one. Results show that thinning the foil around the beam ($-1.2 < y < 1.2\text{cm}$) provides basically the same effect of thinning the entire foil. The foil material contribution for the measured tracks reduces in the same proportion as the foil is thinned. Also, enlarging the thinned region has nearly no effect on the material contribution nor the IP resolution. Finally, the thickness of the outer

region also has nearly no effect. This are very promising results which prove that the RF foil would greatly benefit from partial thinning. Partial thinning experimental techniques are still under development and a decision with respect to this feature will be taken next year.

The Dalitz plot analysis of the $D^+ \rightarrow K^- K^+ \pi^+$ decay allows one to study the KK amplitude in S-wave, which is an important measurement in hadron spectroscopy. Moreover, it can bring a light into topic such as the role of the Final State Interaction and its dependence with respect to the initial state. LHCb provides an extremely large sample of $D^+ \rightarrow K^- K^+ \pi^+$ decays, unveiling the Dalitz distribution of this decay in detail, but also posing a big challenge in modeling the decay amplitude.

The analysis involves several steps. The Rio+, which is the software framework for toy MC generation and Dalitz plot fitting used for this and other analyses, is well tested and working properly. The package presents features such as setting the masses and widths of resonances as free parameters and the PWA model fit. By developing our own software we were able to acquire full knowledge and control of the analysis tool, providing us freedom to adapt it according to our needs, such as optimizing the integration precision for our case.

The selection criteria was chosen aiming for high purity sample without adding strong distortions to the efficiency across the Dalitz plot. It was possible to achieve a 98.9% purity sample without introducing significant distortions. We identified the main background contributions and included them in our fit through histograms based on the sidebands distribution.

The detection, reconstruction and selection efficiency across the Dalitz plot was taken into account using the full LHCb MC simulation and PID efficiencies from calibration data. The obtained efficiency is smoothed by a 2D cubic spline and included in the fit as a high resolution histogram. Since the TOS requirement with respect to the L0 hadron line presents a more uniform efficiency, we decide to adopt this requirement to the Dalitz fit.

We perform several fits using distinct models. We verify that, starting with the CLEO model and going to the BaBar model, adding resonances one by one, that the fit quality is significantly improved, but with a few contributions with small significance. Removing these contributions we achieved, in model 4, a stable composition which changes very little with reasonable modifications. In this model S-wave in the high $s_{K^-K^+}$ region is composed by only three resonances, that we associate with the $f_0(X)$, $f_0(1500)$ and $f_0(1710)$ states. The obtained mass and width for the $f_0(X)$ were $1.372 \pm 0.006 \text{ GeV}/c^2$ and $0.385 \pm 0.005 \text{ GeV}/c^2$, respectively.

The next step in the analysis is to perform the fit with PWA. The Rio+ package is tested and ready to make the fits. We have a fairly reasonable isobar model to use as an input. Performing the PWA is the best alternative to achieving a good description of the S-wave in the $D^+ \rightarrow K^- K^+ \pi^+$ decay. This is the next stage in this analysis and we intend to perform it soon, together with a full study of systematic errors.

Bibliography

- [1] LHCb COLLABORATION, A. Augusto Alves Jr. *et al.* The lhcb experiment at the CERN Large Hadron Collider. *JINST*, **3**:S08005, 2008.
- [2] L. Evans, P. Bryant, LHC machine. *JINST*, **3**:S08001, 2008.
- [3] LHCb Collaboration, LHCb Vertex Locator Technical Design Report. **CERN/LHCC/2001-011**.
- [4] LHCb Collaboration, Letter of Intent for the LHCb Upgrade. **CERN-LHCC-2011-001**.
- [5] LHCb Collaboration, Framework TDR for the LHCb Upgrade: Technical Design Report. **CERN-LHCC-2012-007** .
- [6] LHCb Collaboration, LHCb VELO Upgrade Technical Design Report. **CERN-LHCC-2013-021**.
- [7] ALICE COLLABORATION, K. Aamodt *et al.*, The ALICE experiment at the CERN Large Hadron Collider. *JINST*, **3**:S08002, 2008.
- [8] ATLAS COLLABORATION, G. Asd *et al.*, The ATLAS experiment at the CERN Large Hadron Collider. *JINST*, **3**:S08003, 2008.
- [9] CMS COLLABORATION, S. Chatrchyan *et al.*, The CMS experiment at the CERN Large Hadron Collider. *JINST*, **3**:S08004, 2008.

- [10] LHCb Collaboration, LHCb Detector Performance. *Int. J. Mod. Phys. A*, 30, 1530022, 2015.
- [11] LHCb Collaboration, LHCb Magnet Technical Design Report. **CERN-LHCC-2000-007**.
- [12] LHCb Collaboration, Performance of the LHCb Vertex Locator. *JINST*, 9, P02007, 2014.
- [13] LHCb Collaboration. LHCb Inner Tracker Technical Design Report. **CERN-LHCC 2002- 029**.
- [14] LHCb Collaboration. LHCb Outer Tracker Technical Design Report. **CERN-LHCC 2001- 024**.
- [15] LHCb Outer Tracker group, Performance of the LHCb Outer Tracker. *JINST*, 9, P01002, 2014.
- [16] D. van Eijk *et al*, Radiation Hardness of the LHCb Outer Tracker. *Nucl. Instrum. Methods Phys. Res. A*, 685, 62-69, (2012).
- [17] LHCb Collaboration. LHCb RICH Technical Design Report. **CERN-LHCC-2000-037**.
- [18] LHCb RICH Collaboration, Performance of the LHCb RICH detector at the LHC. *Eur. Phys. J. C*, 73:2431, 2013.
- [19] LHCb Collaboration. LHCb Calorimeters Technical Design Report. **CERN-LHCC 2000- 036**.
- [20] LHCb Collaboration. LHCb Muon System Technical Design Report. **CERN-LHCC 2001-029**.
- [21] A.A. Alves Jr *et al*, Performance of the LHCb muon system. *JINST*, 8, P02022, 2013.

- [22] F. Archilli *et al*, Performance of the Muon Identification at LHCb. *JINST*, **8**, P10020, 2013.
- [23] LHCb Collaboration. LHCb Trigger Technical Design Report. **CERN-LHCC-2003-031**.
- [24] arXiv:hep-ph/0603175v2.
- [25] J. Allison et al., *IEEE Transactions on Nuclear Science* **53**:1 2006.
- [26] S. Agostinelli et al., *Nuclear Instruments and Methods* **A**:506 2003
- [27] S. Agostinelli *et al*, Geant4 — a simulation toolkit. *Nuclear Instruments and Methods in Physics Research Section A: Accelerators, Spectrometers, Detectors and Associated Equipment* **506**: 250.
- [28] R. Aaij *et al*, The LHCb trigger and its performance in 2011. *JINST*, **8**, P04022, 2013.
- [29] LHCb Collaboration, LHCb Tracker Upgrade Technical Design Report. **CERN-LHCC-2014-001** .
- [30] LHCb Collaboration, LHCb PID Upgrade Technical Design Report. **CERN-LHCC-2013-022** .
- [31] LHCb Collaboration, LHCb Trigger and Online Upgrade Technical Design Report. **CERN-LHCC-2014-016**.
- [32] O. Francisco, Medida da seção de choque relativa $\sigma_{Z+b}/\sigma_{Z+jato}$ e desenvolvimento de sistema de resfriamento de detectores de pixel para o LHCb . *Instituto de Física, Universidade Federal do Rio de Janeiro*, Thesis, 2015.
- [33] E. Byckling and K. Kajantie, Particle Kinematics, *John Wiley and Sons*, 1971.
- [34] R. H. Dalitz, On the analysis of τ -meson data and the nature of the τ -meson. *Philosophical Magazine*, **33**: 1068, 1953.

- [35] K.A. Olive et al. (Particle Data Group), *Chin. Phys. C*, 38, 090001 (2014) and 2015 update
- [36] A.D. Martin, T. Spearman, Elementary Particle Theory, *North Holland, Amsterdam*, 1970.
- [37] S. Weinberg, The Quantum Theory of Fields, vol. I. *Cambridge University Press*, 1995.
- [38] J. Beringer *et al.* *Particle Data Group*, PR D86, 010001, 2012.
- [39] J. Blatt and V. Weisskopf, Theoretical Nuclear Physics, *John Wiley and Sons*, 1952.
- [40] C. Zemach, Three-Pion Decays of Unstable Particles, *Phys. Rev. B*, **133**: 1201, 1971.
- [41] G. Breit and E. Wigner, Capture of Slow Neutrons. *Physical Review*, **49** (7): 519, 1936.
- [42] S. Flatté, *Phys. Lett. B*, **63B**: 224, 1976.
- [43] G. J. Gounaris and J. J. Sakurai, Finite-Width Corrections to the Vector-Meson-Dominance Prediction for $\rho \rightarrow e^+e^-$, *Phys. Rev. Lett*, **21**: 244, 1968.
- [44] S. U. Chung *et al*, Partial wave analysis in K-matrix formalism, *Annalen der Physik*, **507**: 404-430, 1995.
- [45] D. Aston *et al*, A study of $K^-\pi^+$ scattering in the reaction $K - p \rightarrow K^-\pi^+n$ at 11 GeV/c , *Nucl. Phys. B*, **296**, 493, 1988 .
- [46] W. H. Press *et al*, Numerical Recipes: the Art of Scientific Computing, Third Edition, *Cambridge University Press*, 2007.
- [47] Laura++ Dalitz plot fitting package, University of Warwick.
<https://laura.hepforge.org>

- [48] T. Sekihara and S. Kumano, A constraint on K \bar{K} compositeness of the $a_0(980)$ and $f_0(980)$ resonances from their mixing intensity , *arXiv:1409.2213*, 2014.
- [49] L. Maiani, A. D. Polosa and V. Riquer, Structure of Light Scalar Mesons from D_s and D^0 Non-Leptonic Decays, *arXiv:hep-ph/0703272*, 2014.
- [50] BaBar Collaboration, Dalitz plot analysis of $D_s^+ \rightarrow K^- K^+ \pi^+$, *arXiv:1011.4190 [hep-ex]*. *BABAR-PUB-10/016*. *SLAC-PUB-14266.*, 2011.
- [51] E. M. Aitala et al. (Fermilab E791 Collaboration), Dalitz Plot Analysis of the Decay $D^+ \rightarrow K^- \pi^+ \pi^+$ and Indication of a Low-Mass Scalar $K\pi$ Resonance, **Phys. Rev. Lett.**, 89, 121801, 2002.
- [52] B. Aubert et al., [BaBar collaboration], Dalitz plot analysis of the $D_s^+ \rightarrow \pi^- \pi^+ \pi^+$ decay, *Phys. Rev. D* 79, 032003, 2009.
- [53] B. Hyams et al., $\pi\pi$ phase-shift analysis from 600 to 1900 MeV, *Nucl. Phys. B*, 64, 134 (1973), G. Grayer et al., High statistics study of the reaction $\pi - p \rightarrow \pi^- \pi^+ n$: Apparatus, method of analysis, and general features of results at 17 GeV/c, *Nucl. Phys. B* 75, 189, 1974.
- [54] D. Aston et al., [LASS collaboration], A study of $K^- \pi^+$ scattering in the reaction $K^- \pi^+ \rightarrow K^- \pi^+ n$ at 11 GeV, *Nucl. Phys. B* 296, 493, 1988.
- [55] J. M. Link et al. , [FOCUS collaboration], The $K^- \pi^+$ S-wave from the $D^+ \rightarrow K^- \pi^+ \pi^+$ decay, *Phys. Lett. B* 681, 14, 2009.
- [56] CLEO Collaboration, Search for CP violation in the Dalitz-plot analysis of $D^+ \rightarrow K^- K^+ \pi^+$, *Phys. Rev. D*. **78**: 072003, 2008.
- [57] BaBar Collaboration, Search for direct CP violation in singly Cabibbo-suppressed $D^+ \rightarrow K^- K^+ \pi^+$ decays, *arXiv:1212.1856*. *BABAR-PUB-12-014*. *SLAC-PUB-15077*. 2012.

- [58] A. Martin Sanchez, P. Robbe, and M.-H. Schune, Performances of the LHCb L0 Calorimeter Trigger, Tech. Rep. **LHCb-PUB-2011-026**. **CERN-LHCb-PUB-2011-026**, CERN, Geneva, (2012).
- [59] Puig, Albert, The LHCb trigger in 2011 and 2012, Tech. Rep. **CERN-LHCb-PUB-2014-046**, CERN, Geneva, (2014).
- [60] W. D. Hulsbergen, Decay chain fitting with a Kalman filter, Tech. Rep. **Nucl. Instrum. Meth. A**, 552, 566, (2005), arXiv:physics/0503191.
- [61] T. Skwarnicki, A study of the radiative 153 cascade transitions between the Upsilon-prime and Upsilon resonances, *Ph.D. thesis*, 154 Institute of Nuclear Physics, Krakow, DESY-F31-86-02, (1986).
- [62] M. De Cian et al., Measurement of the track finding efficiency, Tech. Rep. **LHCb-PUB-2011-025**. **CERN-LHCb-PUB-2011-025**, CERN, Geneva, (2012).
- [63] BES Collaboration, Resonances in $J/\psi \rightarrow \phi\pi^+\pi^-$ and ϕK^+K^- . **Physics Letters B**, 607, 243–253, (2005).
- [64] Bird, T. et al, VELO upgrade studies and layout optimisations, **LHCb-INT-2014-044**. **CERN-LHCb-INT-2014-044**, CERN, Geneva, 2014
- [65] Ponce, S. et al, Detector Description Framework in LHCb, **eConf C0303241 (2003) THJT007**, arXiv:physics/0306089, **LHCb-PROC-2003-004**, CERN, 2003.

Appendix A

Simulation Studies of the RF foil for the VELO Upgrade

A.1 Introduction

The LHCb Vertex Locator (VELO) is a high precision detector [3] currently based on silicon strip sensors for measuring particle tracks near the interaction region at LHCb. The left and right halves of the VELO can be retracted to allow injection and acceleration of the LHC beams. The detector halves are separated by two corrugated foils that allow closing of the VELO for full coverage of the azimuthal acceptance around the beams. The VELO foil is used:

- to provide radio frequency (RF) shielding of the VELO detector;
- to conduct the wake field mirror currents around the LHC beams;
- to avoid contamination of the primary beam vacuum by a gas-tight separation from the detector vacuum volume.

This so-called VELO RF foil gives a large contribution to the material budget, specially before the first hit, which introduces a major effect on the Impact Parameter

(IP) resolution. ¹ Therefore, it is required to be as thin as possible, in order to minimise the material traversed by particles close to the beam, keeping in consideration the requirements of electrical continuity, mechanical stability and vacuum properties.

For the VELO Upgrade [6] a new design has been created to match the shape of the hybrid pixel detector. It is composed of two different kinds of shapes, designed mainly to minimise the material before the first and second measured points. At the module positions the foil has a corrugated shape which allows the sensors to be placed closer to the beam and to fully cover the region around the beam. Between corrugations the foil is flat along the Z axis. In the X-Y plane, both the flat parts and the corrugations have a step-like function shape that goes along the edge of the modules. In the nominal design, the upgrade foil is 250 μm thick, 1 m long, 18 cm wide and its smallest distance to the beam is 3.5 mm.

The optimization of the RF foil design for the upgrade is crucial since its material has a large impact on the IP resolution. The foil thickness is an important parameter, but also the slope and depth of the corrugations, which determines the angle by which most particles traverse the foil. The distance of the foil to the beam and different distributions of the sensor positions along the beam direction can also be considered [64]. These are the main parameters that were optimized in Monte Carlo simulations with consideration of the mechanical stability, the electrical conductance, and the vacuum tightness to be left for the final design.

¹The IP is the distance between the track and the vertex and its components are given by:

$$IP_x = x_0 + (z_{PV} - z_0)t_x - x_{PV}$$

$$IP_y = y_0 + (z_{PV} - z_0)t_y - y_{PV}$$

where x_0 and y_0 are the x and y coordinates of the track at a given z -position z_0 , t_x and t_y are the corresponding slopes and x_{PV} , y_{PV} , z_{PV} are the x , y and z coordinates of the primary vertex. The 3D distance is given by:

$$IP_{3D} = \sqrt{\frac{IP_x^2 + IP_y^2}{1 + t_x^2 + t_y^2}}$$

A suitable description of the corrugated RF foil in Monte Carlo simulations and track reconstruction is a unavoidable compromise between accuracy of the description (complexity) and the required memory size and computation time (simplicity) of the tracking through the VELO. As complicated foil shapes can always be approximated by generalized trapezoids available in the xml library of the LHCb framework, it was chosen to approximate the CAD design of a corrugation by a solid packing of such trapezoids, without gaps between them.

In this note, we describe a new python code which can be used to create the foil shape. The code requires as input a few relevant parameters, such as the foil thickness and the closest distance between the foil and the beam, giving as output the XML files to be used with the other detector elements in the LHCb framework [65]. This code was written based on a fortran script that was used to generate the XML description of the RF foil in the VELO Upgrade TDR. Also, we use the code to generate an improved foil shape, thinner at the region around the beam, as it might be possible due to a chemical etching technique in development. Finally, we show the corresponding material scans and IP resolution plots for each tested design.

A.2 RFFoilCreator

The RFFoilcreator.py script purpose is to create the RF foil XML files used in VELO upgrade simulations and it can be found at the SVN (<http://svnweb.cern.ch/world/wsvn/lhcb/obsolete>). The new script is written in python in a straightforward algorithm, with flexibility to easily change parameters and with a new feature: the possibility of defining a region around the beam in which the foil has a different thickness with respect to the outer region.

The representation of the created foil, with the corresponding parameters highlighted, can be seen in the figures A.1, A.2 and A.3. The parameters are:

- SlotDepthX(Y): the depth of the corrugation along the X (Y) axis for the

wings (X parallel segment);

- SlotPiecePosZ: the 10 different z positions where the vertices of the trapezoids are generated for a single foil corrugation;
- FoilDistance: the closest distance of the foil to the beam;
- FoilThickness: initial thickness of the foil defined in the xy plane;
- CorFoilThickThickness and CorFoilThinThickness: the final foil thicknesses with vertex corrections due to the angle of the trapezoid with respect to the beam, for the two distinct foil regions;
- Xedge: the X position of the tip of the corrugation on the $y < 0$ side wing;
- Milling radius: is the radius of the inner circle in the xy plane of the curved foil around the step in x;
- Delta: is the change in x and y for the first corrugation step in z away from the segments parallel to the beam which approximates a curved surface along the z direction;
- FoilSizeY: the size of the foil along the Y direction.

The parameter definitions follow the global LHCb coordinates conventions.

The script starts with the calculation of the corner points (vertices) of the generalized trapezoids on lines f and g, displaced in x and y by an initial foil thickness. The local foil thickness is later corrected for the angle of the trapezoid with respect to the z axis. The lines consist of 17 straight segments in the xy plane of which 5 correspond to the straight foil section and 12 are used to approximate the curved regions around the step in x. The 18 f (g) points are stored in the v1 (v2) list of vertices, together with their corresponding z positions. By combining the same vertices to define neighbouring generalized trapezoids we guarantee a closed foil volume without overlap, which is a necessary requirement for composite volumes in Geant4

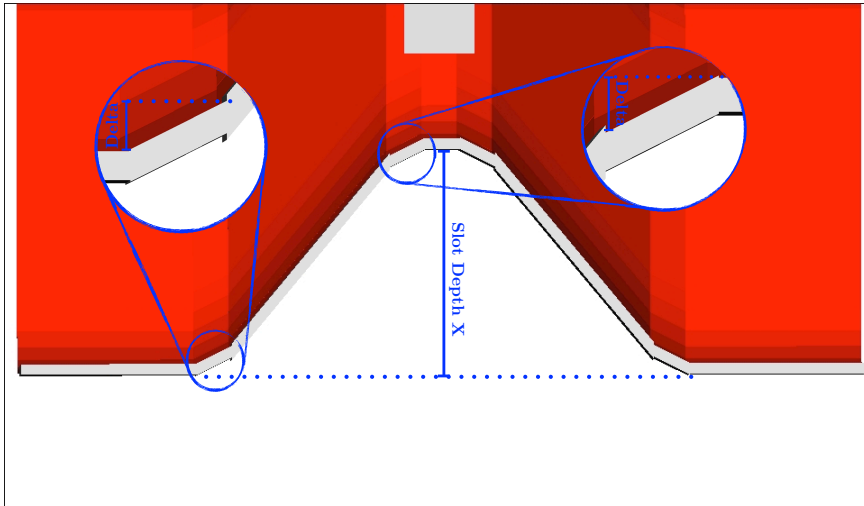


Figure A.1: Foil corrugation viewed from the VELO top perpendicular to the z-x plane. The inserts show the corrected corner positions to obtain the correct 3D foil thickness. The SlotDepthX parameter size is indicated at the sensor position.

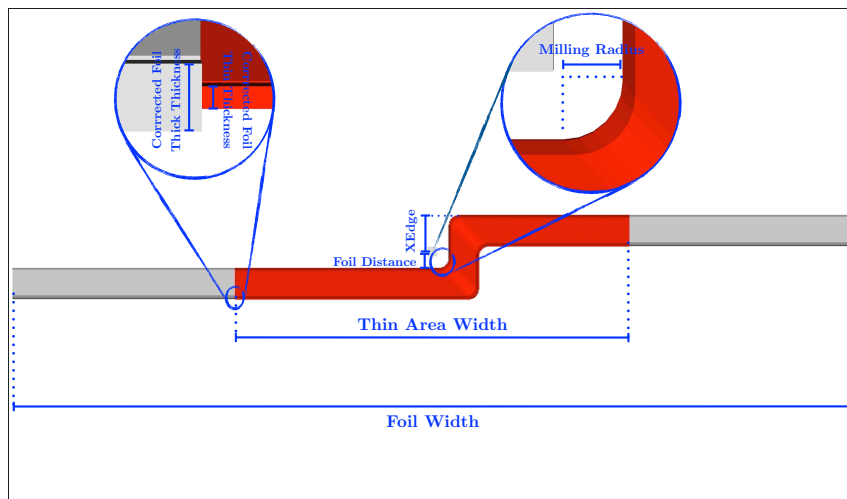


Figure A.2: Foil corrugation viewed in the beam direction perpendicular to the y-x plane. with the thin foil area highlighted in red. Left insert shows the 0.3 mm and the 0.1 mm thick foil cross sections. Right insert shows the size of the MillingRadius parameter.

simulations. This restricted segmentation in z limits the CAD design options for the RF foil and the choice of foil shapes.

After filling the v1 and v2 banks, the script starts a loop to generate the actual parameters of the trapezoids that will be saved in the XML output. Inside the loop, the two parallel faces of the trapezoid are formed. TrapFace1Vertices is the list

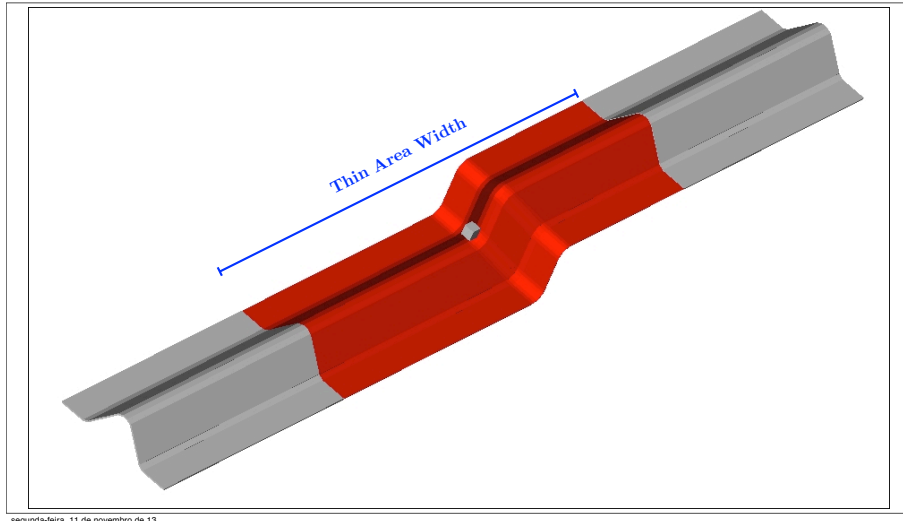


Figure A.3: Single foil corrugation with the thin foil area highlighted in red.

of vertices of the face built on the $v1(f)$ side, by picking two vertices from one of the lines of vertices in $v1$ and two more from the corresponding line on the next Z position. `TrapFace2Vertices` is defined in a similar way, but using vertices stored in $v2$.

Both faces are then submitted to three rotations around the X , Y and Z axis, respectively. After the rotations both faces are parallel to the X - Y plane and the side between the first two vertices in `TrapFac2Vertices` is parallel to the X axis.

Finally, the other XML parameters for trapezoids are calculated. Sides with negative value are corrected with the appropriate rotation. A more detailed description of the meaning of the parameters can be found at [65].

The thickness of the foil is then corrected according to the trapezoid position. If the trapezoid falls inside the y region within half the width of the thin area from the beam ($-ThinAreaWidth/2 < y < ThinAreaWidth/2$) from the beam axis, then its thickness is `CorFoilThinThickness`, otherwise ($|y| > ThinAreaWidth/2$) it is `CorFoilThickThickness`. The change in thickness moves the vertices of the trapezoid along its side planes. Therefore, the composed foil remains closed without overlap by this change.

Flat parts between the corrugated parts are simply described by boxes and segmented tubes; their size in z is defined by the sensor distance minus the size in z of a single foil corrugation.

The output is then stored in two .xml files which can be directly copied to the LHCb XML folders (VP/Geometry/Catalogue/ and VP/Geometry/LogVol/) as RFFoil.xml and may be implemented at the start of a new simulation without further requirements.

A.3 Material scans and IP resolution plots

The RF foil gives a large contribution to the amount of material traversed by particles. By optimizing its shape and reducing its material contribution, we may be able to significantly improve the IP resolution. The RFFoilCreator script may be an important tool within this task, since it can easily produce foils with different shapes.

A few distinct RF foil shapes were generated in order to test the output given by the RFFoilCreator script and to investigate how the new feature, the definition of regions with different thickness, impacts on the IP resolution. With the purpose of accounting for the effect of the inner region thickness, three values were used: 100 μm , 200 μm and 300 μm , with the outer region thickness of 300 μm and the width of the thinner area of 44 mm. With the combination of 100 μm inner and 300 μm outer thickness, five widths were simulated for the thin region: 44 mm, 54 mm, 64 mm, 74 mm and 84 mm. This width can be increased to nearly the full foil width, but it cannot be equal or smaller than 24 mm, due to the more complex geometry within the region around the beam. Finally, in order to evaluate the effect of the outer region, three simulations were done using 100 μm thickness for the inner region and 300 μm , 400 μm and 500 μm for the outer region.

Simulated tracks, with gaussian distribution for the origin z position and constant

distribution for η and ϕ , were used in order to test different shapes, recording the length of material traversed by each one and the radiation length of the material for each volume. The parameters were chosen considering the desired characteristics for the RF foil. The outer region with at least 300 μm would be responsible for giving the mechanical stability, while the thinner region, with 100 μm or more, would still provide enough RF-shielding and a vacuum tight barrier.

In the figures A.4 and A.5, the plots for the integrated fraction of radiation length, x/X_0 , of a RF foil with uniform thickness of 300 μm and of a partially thinned foil with 300 μm thickness on the outer part and 100 μm on the inner part, with 44 mm width, are shown, respectively. It is clear that, as expected, the amount of material traversed by particles is significantly reduced in the later case. The material scans for a foil with 300 μm outer thickness and 100 μm inner thickness, but with 84 mm width, can be seen at figure A.6. There, we see no large differences with respect to the ones shown in figure A.5, specially before the first and the second hits, which means that increasing the width of the thin region does not give a significant effect on the material scan and also, therefore, on the IP resolution.

The direct comparison of the material scans can be seen in projections on the ϕ and η axis in the figures A.7, A.8 and A.9. It is clear that the inner region of the foil gives most of the material contribution. Reducing its thickness improves drastically the amount of material provided by the foil. Also, Figure A.8 shows us that increasing the width of the thin region does not significantly improve the material amount, specially before the first and the second hit. We can conclude that the thick region gets nearly no first or second hits, even when the width of the thin region is as small as 44 mm. Likewise, the thickness of the outer area of the foil does not introduce significant effects before the first and second hits, as shown in figure A.9.

The material reduction given by the partially thinned foil shape greatly improves the IP resolution, as seen in figure A.10. In fact, it is possible to notice that reducing

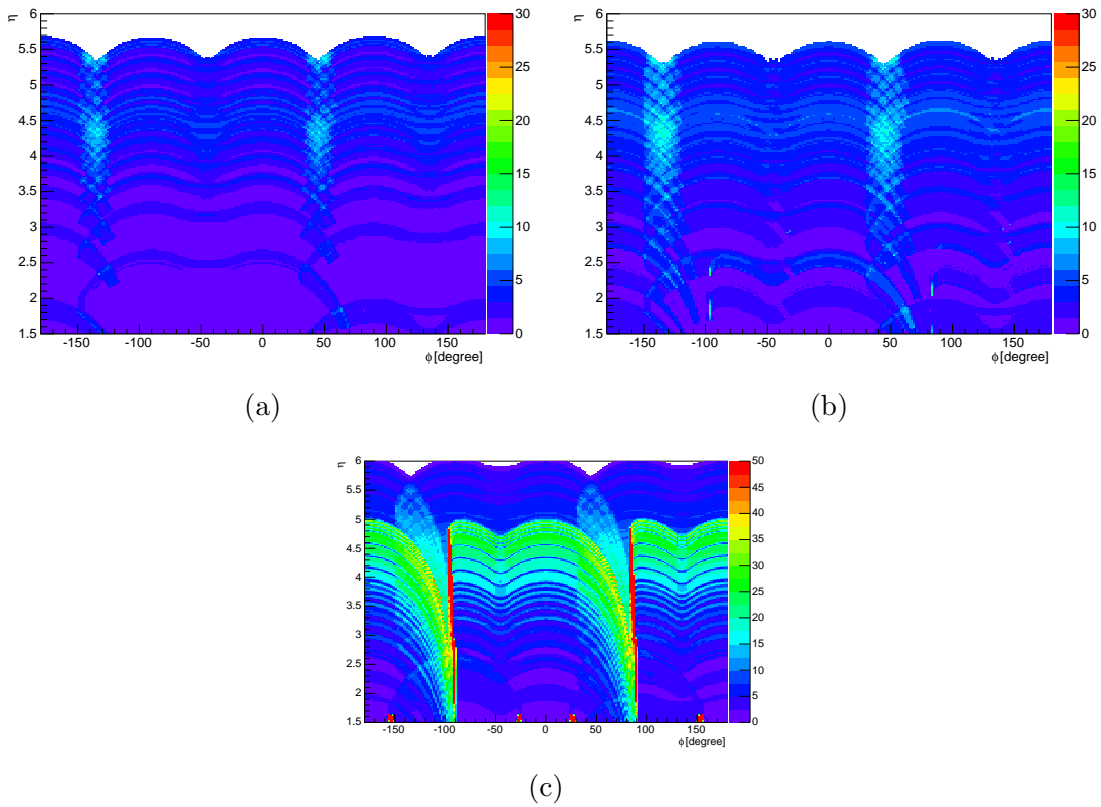


Figure A.4: Material scans of the RF foil with full $300\ \mu\text{m}$ thickness. Plots (a), (b) and (c) show the percentage of radiation length for the foil before the first hit, before the second hit and total, respectively.

the thickness of the inner region of the foil improves significantly the IP resolution, towards the no foil scenario, from which we conclude that reducing the thickness of the foil region around the beam is nearly as effective as thinning the entire foil.

On the other hand, increasing the width of the thin region, as expected from the material scans, does not improve the IP resolution. In figure A.11 we notice that both the options with 44 mm and 84 mm wide thin region present the same IP resolution.

Finally, the foil shapes with different thickness on the outer region also present very similar IP resolutions, as shown in figure A.12. This, together with the previous results, shows us that only the inner region of the foil has a significant material contribution before the first and second hits and, therefore, it is the only part that significantly impacts on the IP resolution.

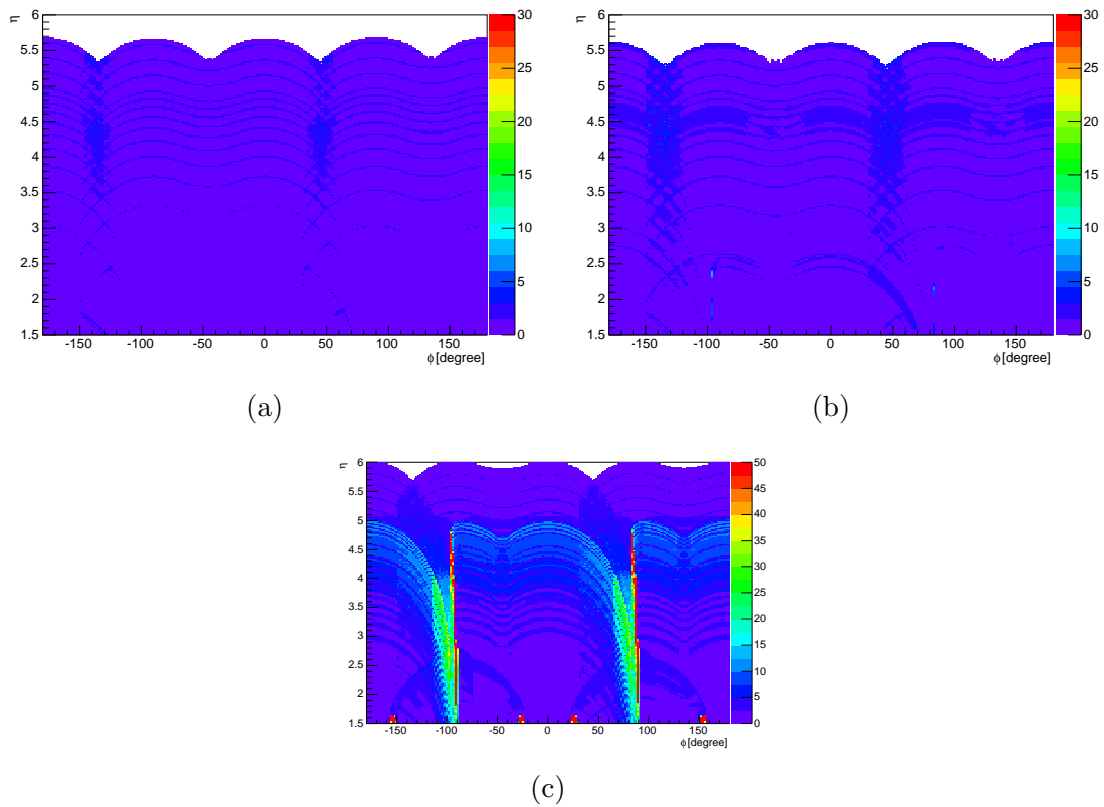


Figure A.5: Material scans of the RF foil with $100 \mu\text{m}$ thickness at the region within $-22\text{mm} < y < 22\text{mm}$ (44 mm width) and $300 \mu\text{m}$ thickness elsewhere. Plots (a), (b) and (c) show the percentage of radiation length for the foil before the first hit, before the second hit and total, respectively.

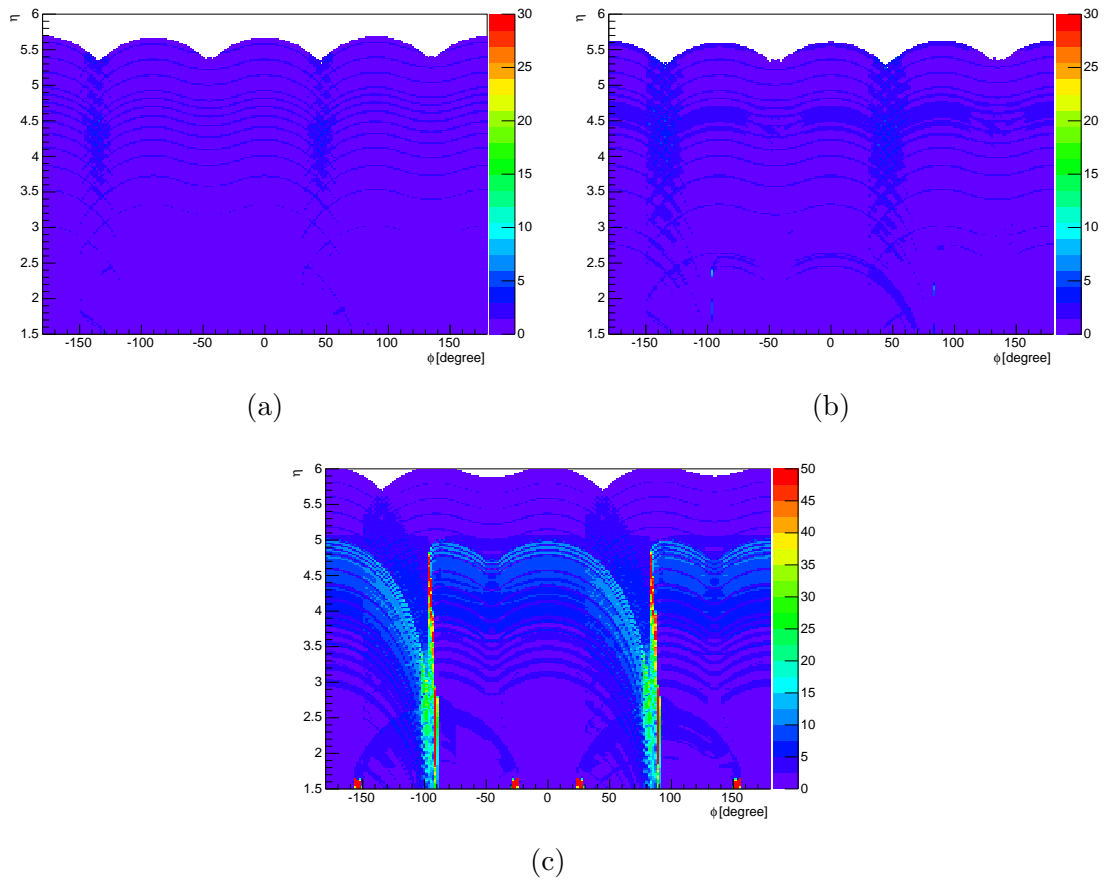


Figure A.6: Material scans of the RF foil with $100\ \mu\text{m}$ thickness at the region within $-42\text{mm} < y < 42\text{mm}$ (84 mm width) and $300\ \mu\text{m}$ thickness elsewhere. Plots (a), (b) and (c) show the percentage of radiation length for the foil before the first hit, before the second hit and total, respectively.

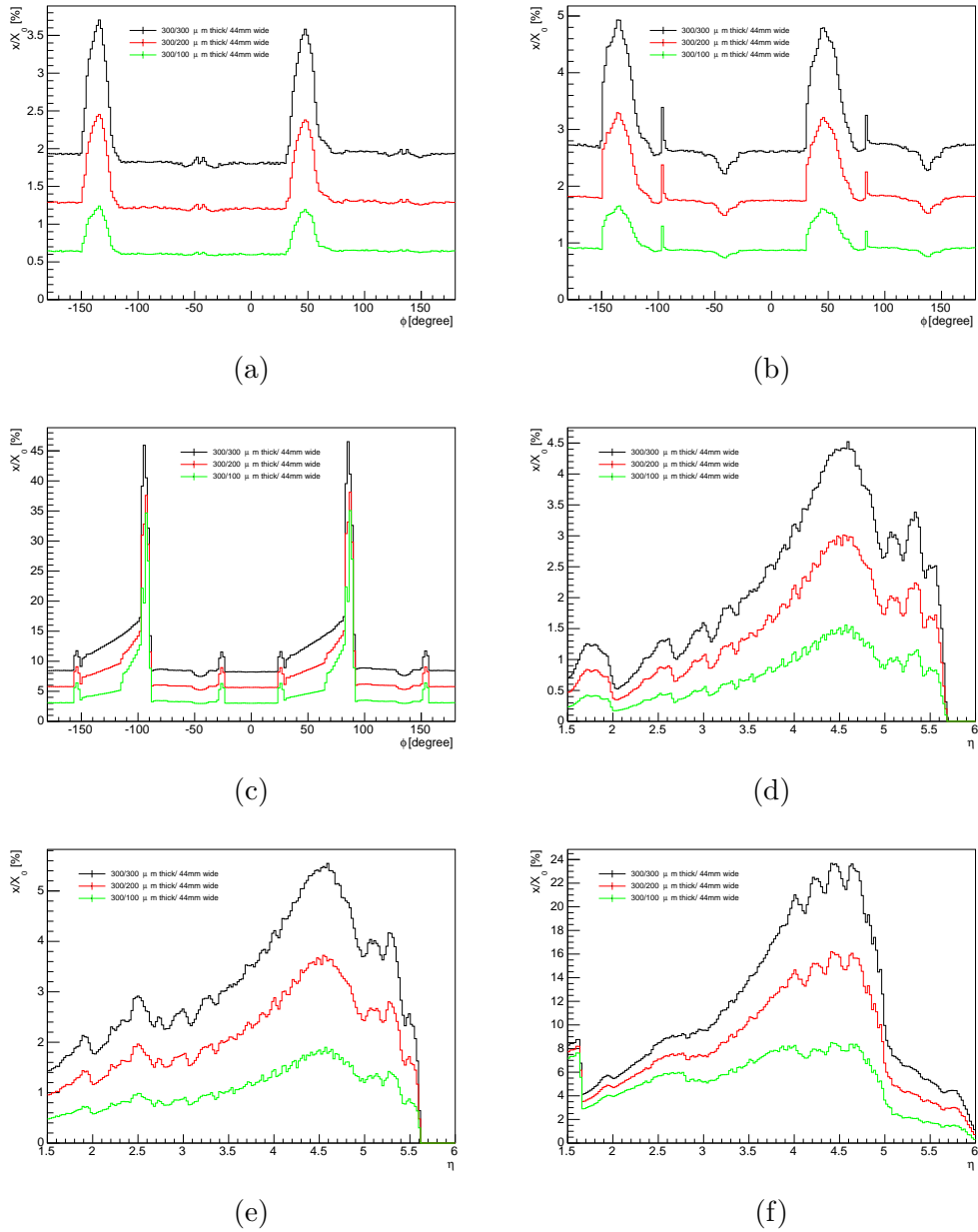


Figure A.7: Projections of the material scans, in ϕ and η coordinates, of the RF foil designs with $300\ \mu\text{m}$ thickness on the outer region of the foil and with a $44\ \text{mm}$ wide inner thickness of $100\ \mu\text{m}$ (green), $200\ \mu\text{m}$ (red) and $300\ \mu\text{m}$ (black). Plots (a), (b) and (c) show the ϕ projections of the scans before the first hit, before the second hit and total, respectively, while (d), (e) and (f) are the η projections of the same scans

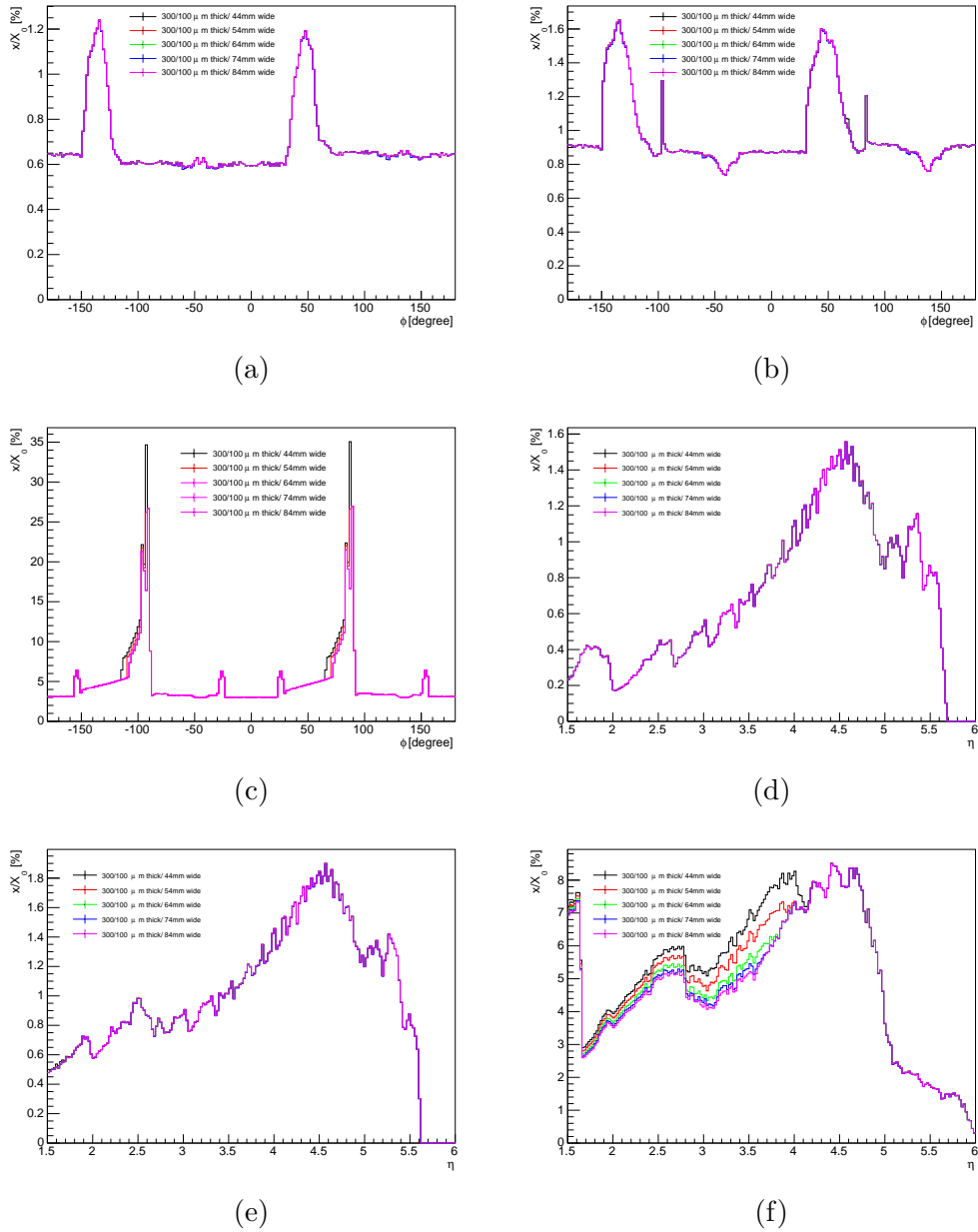


Figure A.8: Projections of the material scans, in ϕ and η coordinates, of the RF foil designs with $300 \mu\text{m}$ thickness on the outer region of the foil and with inner thickness of $100 \mu\text{m}$, but with widths for the thin region that go from 44 mm to 84 mm in 10 mm steps. Plots (a), (b) and (c) show the ϕ projection of the scans before the first hit, before the second hit and total, respectively, while (d), (e) and (f) are the η projections of the same scans

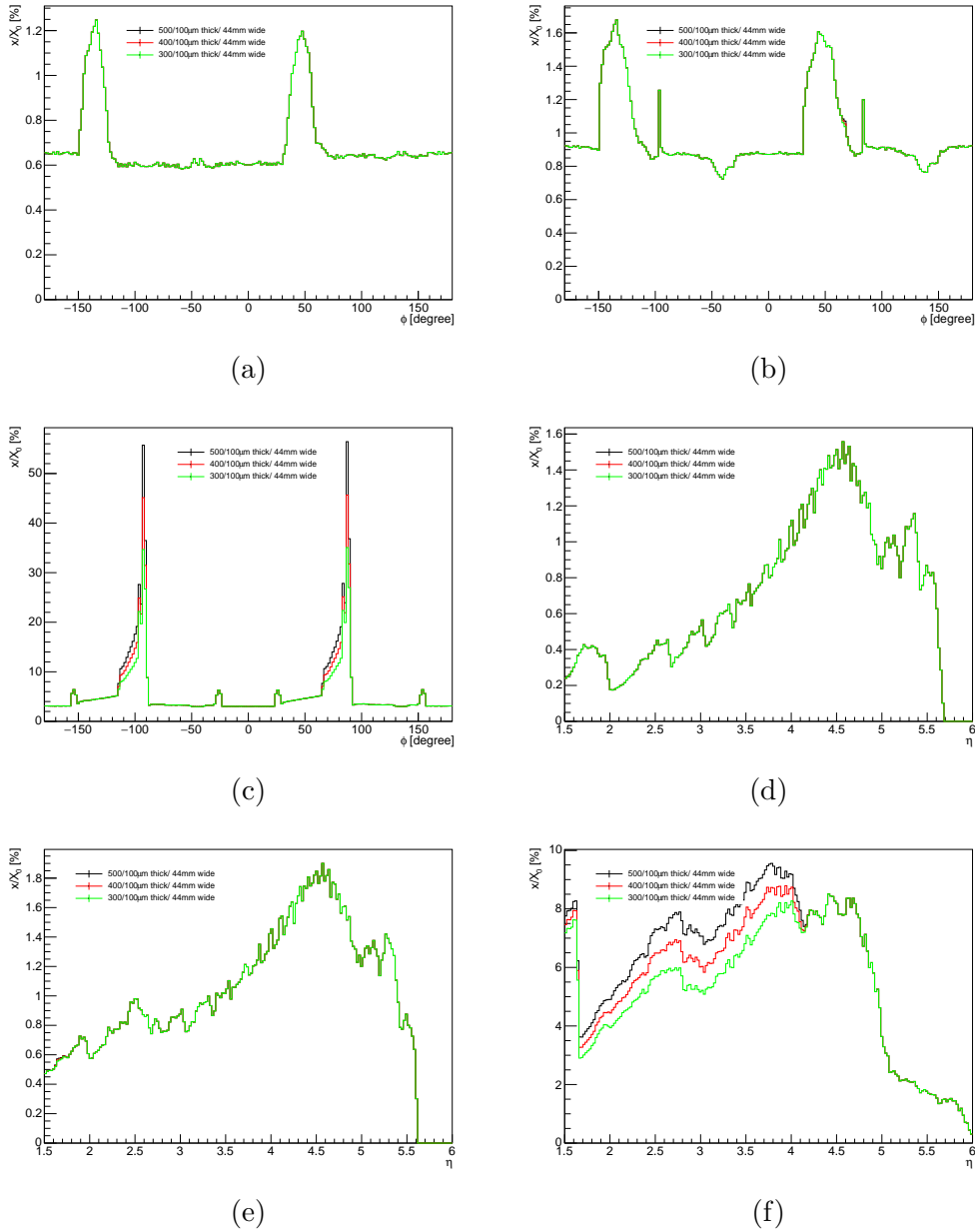


Figure A.9: Projections of the material scans, in ϕ and η coordinates, of the RF foil designs with 300 μm , 400 μm and 500 μm thickness on the outer region of the foil, inner thickness of 100 μm and with width for the thin region of 44 mm. Plots (a), (b) and (c) show the ϕ projection of the scans before the first hit, before the second hit and total, respectively, while (d), (e) and (f) are the η projections of the same scans

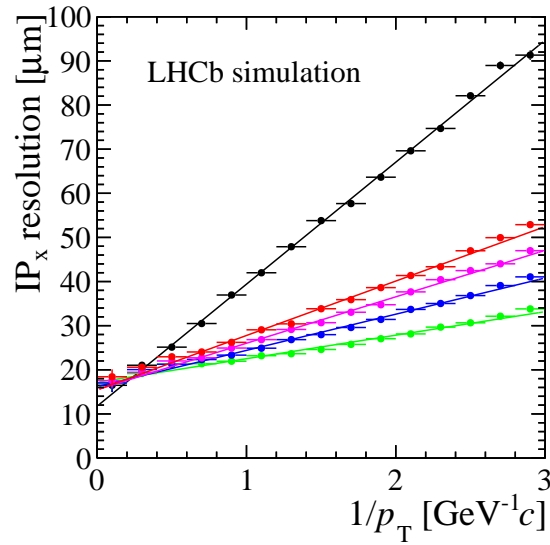


Figure A.10: IP resolution vs. $1/p_t$ of samples generated using distinct RF foil designs. It is possible to see the current VELO in black, the upgrade VELO with full $300\ \mu\text{m}$ thick foil in red, the upgrade VELO with $44\ \text{mm}$ wide $200\ \mu\text{m}$ foil in pink, the upgrade VELO with $44\ \text{mm}$ wide $100\ \mu\text{m}$ foil in blue and the upgrade VELO with no foil in green.

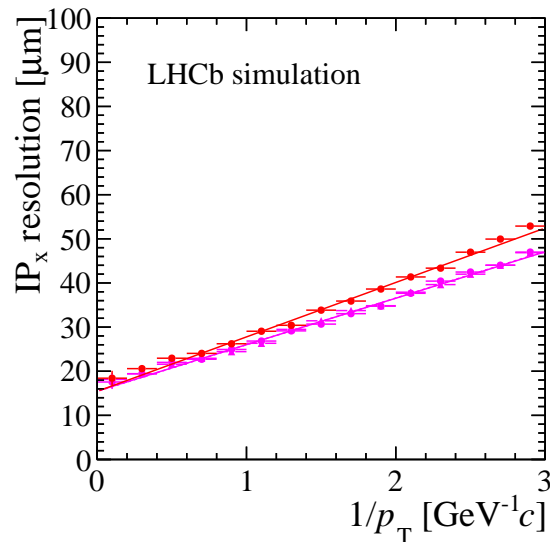


Figure A.11: IP resolution vs. $1/p_t$ of samples generated using upgrade VELO and three different RF foil designs. The $300\ \mu\text{m}$ uniform thickness foil is shown in red, the partially thinned foil with a $44\ \text{mm}$ wide $200\ \mu\text{m}$ thin region is shown in pink, with solid line and circle symbol, and the partially thinned foil with a $84\ \text{mm}$ wide $200\ \mu\text{m}$ thin region is shown in pink, but with dashed line and triangle markers.

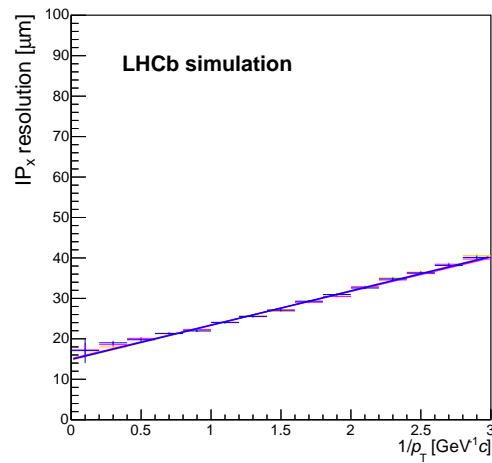


Figure A.12: IP resolution vs. $1/p_t$ of samples generated using upgrade VELO and three different RF foil designs, with $300 \mu\text{m}$ (blue), $400 \mu\text{m}$ (magenta) and $500 \mu\text{m}$ (orange) outer region thickness. All three shapes used a inner region thickness of $100 \mu\text{m}$.

A.4 Conclusion

The RFFoilCreator script provides a practical way to generate the XML files for the RF foil, with easily tunable parameters. In this document, in section A.2, we describe its basic algorithm and the parameters used by it. In particular, a new feature has been added with respect to the previous code, which allows the definition of two different thickness regions, one located closer to the beam ($-ThinAreaWidth/2 < y < ThinAreaWidth/2$), and the other located away from the beam ($|y| > ThinAreaWidth/2$).

The results obtained using the new feature show a significant improvement on the material scans and on the IP resolutions. Reducing the thickness of the inner region of the foil is almost the same as reducing the thickness of the entire foil. Neither increasing the width of the thin region nor changing the thickness of the thick region has a large impact on both the material scans and the IP resolutions. Implementing this feature on the actual foil would be of great interest, since this could be a way of obtaining a better IP measurement performance without losing its other desired features.

Appendix B

List of TCKs used in 2012 Data

The HLT1 and L0 lines used in this analysis are Hlt1TrackAllL0 and L0Hadron. In Table B.1 we show a list of TCKs used in data taken in 2012 with the values of the cuts applied to these lines. It can be seen that they did not vary too much along the year.

			0x00990042	0x008C0040
h^\pm	p	MeV/c	> 3000	> 2000
	p_T	MeV/c	> 300	> 200
	χ_{IP}^2		> 6	> 5
$h^+h^-h^+$ combination	$\sum p_T$	MeV/c	> 2800	> 2500
D^\pm	$\chi_{\text{vtx}}^2/\text{ndf}$		< 15	< 20
	χ_{IP}^2		< 12	< 15
	χ_{VS}^2		> 175	> 150

Table B.1: TCKs used in 2012. The fraction indicates how many data, after the stripping selection, were taken with these TCK. The values of the cuts used in the `Hlt1TrackAllL0` and `L0Hadron` are also shown.

TCK	fraction MagDown	fraction MagUp	L0 Hadron E_T GeV	Hlt1TrackAllL0 $P_T >, P > [\text{GeV}/c], \text{Track } \chi^2/ndf <$
0x007E003A	0.000106	–	3.5	1.7, 10., 2.0
0x007F0040	0.000302	–		
0x008C0040	0.076678	–		
0x008E0040	0.000578	–		
0x0094003D	0.097664	0.155223	3.62	1.7, 10., 1.5
0x0097003D	0.136946	0.110886	3.62	1.7, 10., 1.5
0x0095003D	0.001036	–	3.62	1.7, 10., 2.0
0x00990042	0.197045	0.374671	3.62	1.6, 3., 2.0
0x00990044	0.112760	0.031833	3.68	1.6, 3., 2.0
0x00A30044	0.144220	–	3.68	1.6, 3., 2.0
0x009F0045	–	0.026939	3.74	1.6, 3., 2.0
0x00A10044	–	0.026345	3.74	1.6, 3., 2.0
0x00A10045	–	0.070239	3.74	1.6, 3., 2.0
0x00A30044	–	0.172476	3.74	1.6, 3., 2.0
0x00A30046	0.011292	0.020022	3.74	1.6, 3., 2.0
0x00A90046	0.065193	–	3.74	1.6, 3., 2.0
0x00AB0046	0.051422	–	3.74	1.6, 3., 2.0
0x00AC0046	0.104693	0.008495	3.74	1.6, 3., 2.0
0x00AD0046	0.000063	–	3.74	1.6, 3., 2.0

Appendix C

Dalitz Distribution in $5 \text{ MeV}/c^2$

Windows

This appendix presents the Dalitz distribution for data, after applying all selection criteria, in $5 \text{ MeV}/c^2$ windows, from $M_D = 1800 \text{ MeV}/c^2$ to $M_D = 1920 \text{ MeV}/c^2$. Angular distribution patterns appear in all plots, showing that the background contains structures of this type.

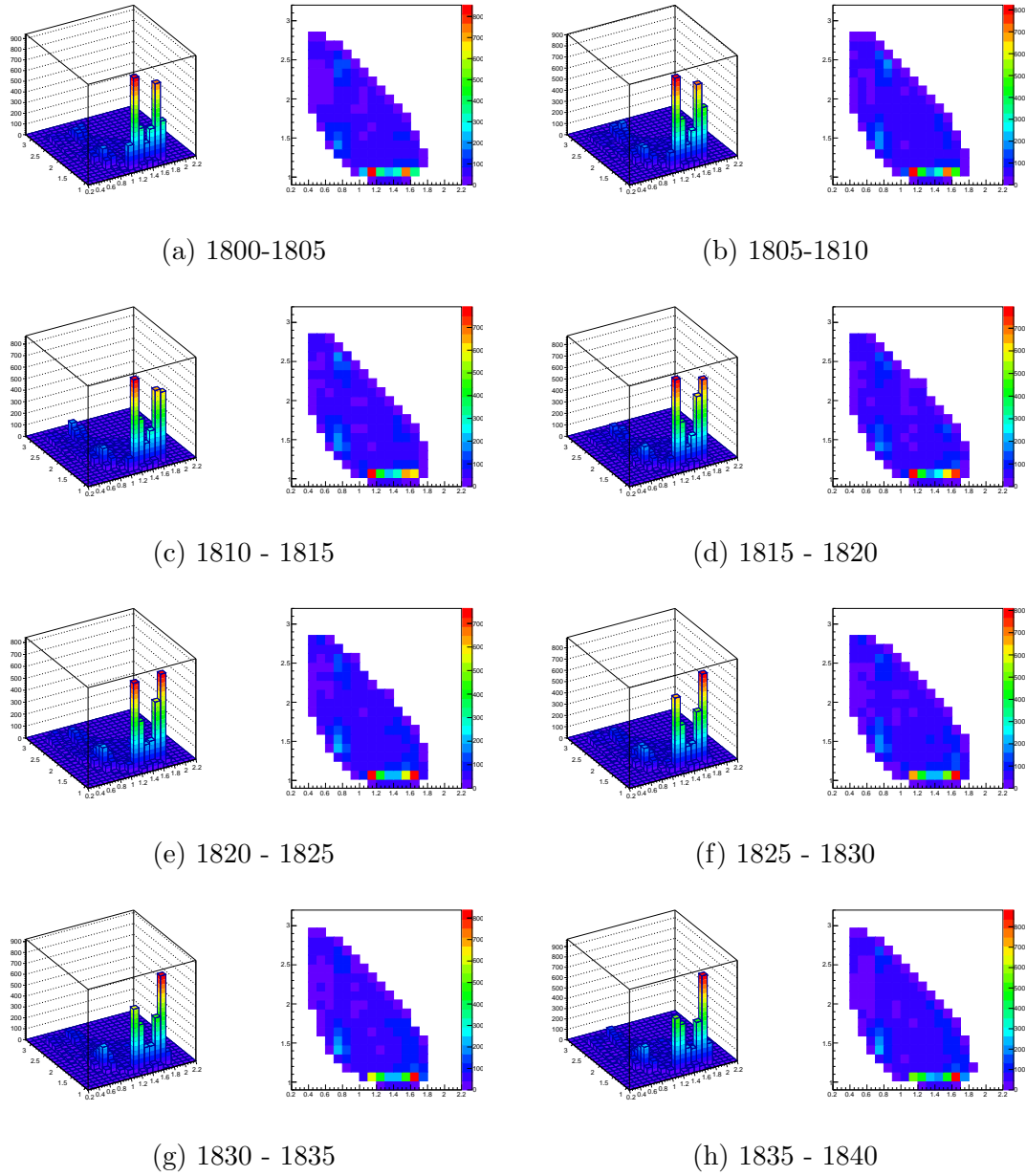


Figure C.1: Dalitz distribution in $5 \text{ MeV}/c^2$ windows. Units in each plot subcaption is also in MeV/c^2 .

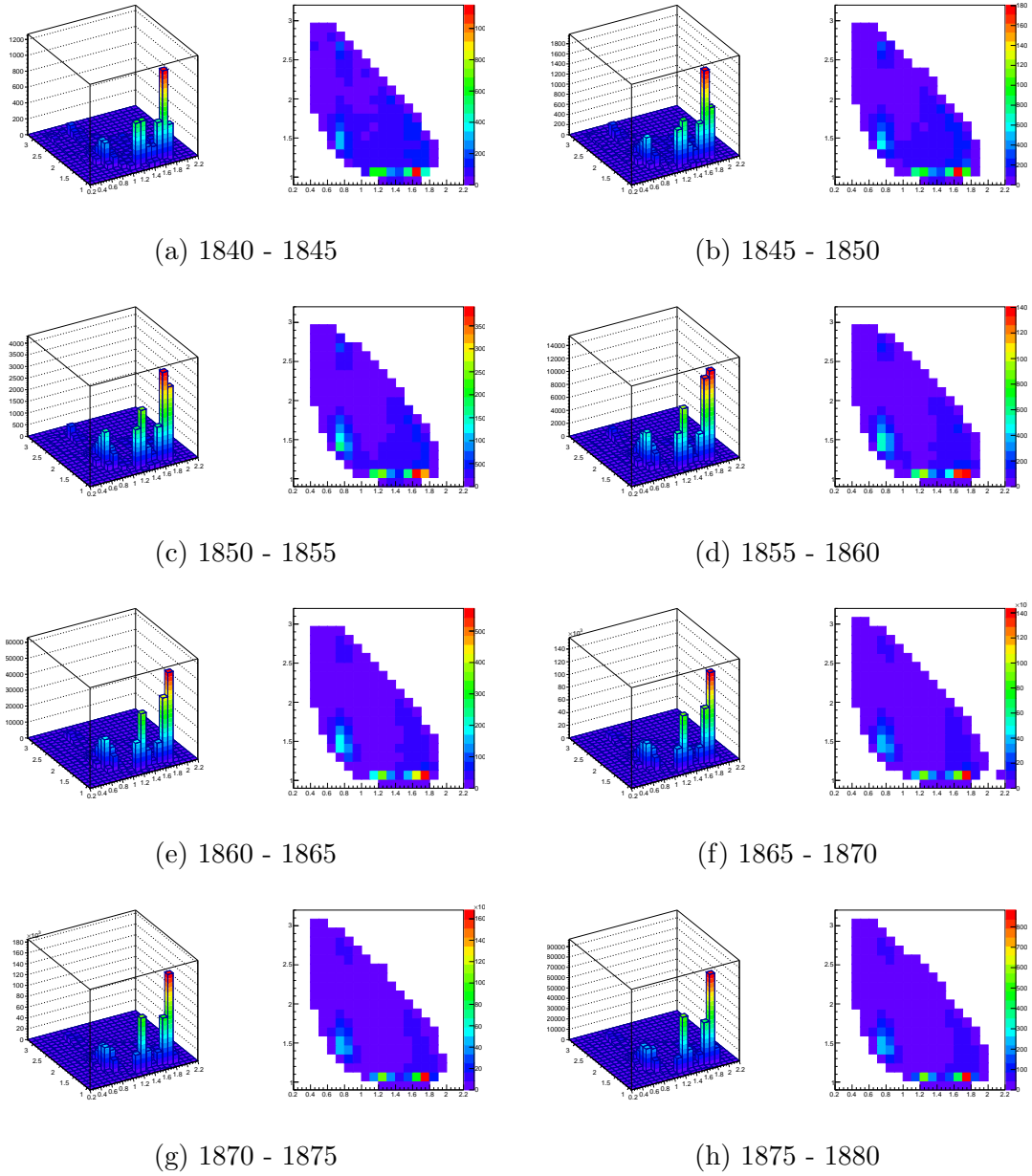


Figure C.2: Dalitz distribution in $5 \text{ MeV}/c^2$ windows. Units in each plot subcaption is also in MeV/c^2 .

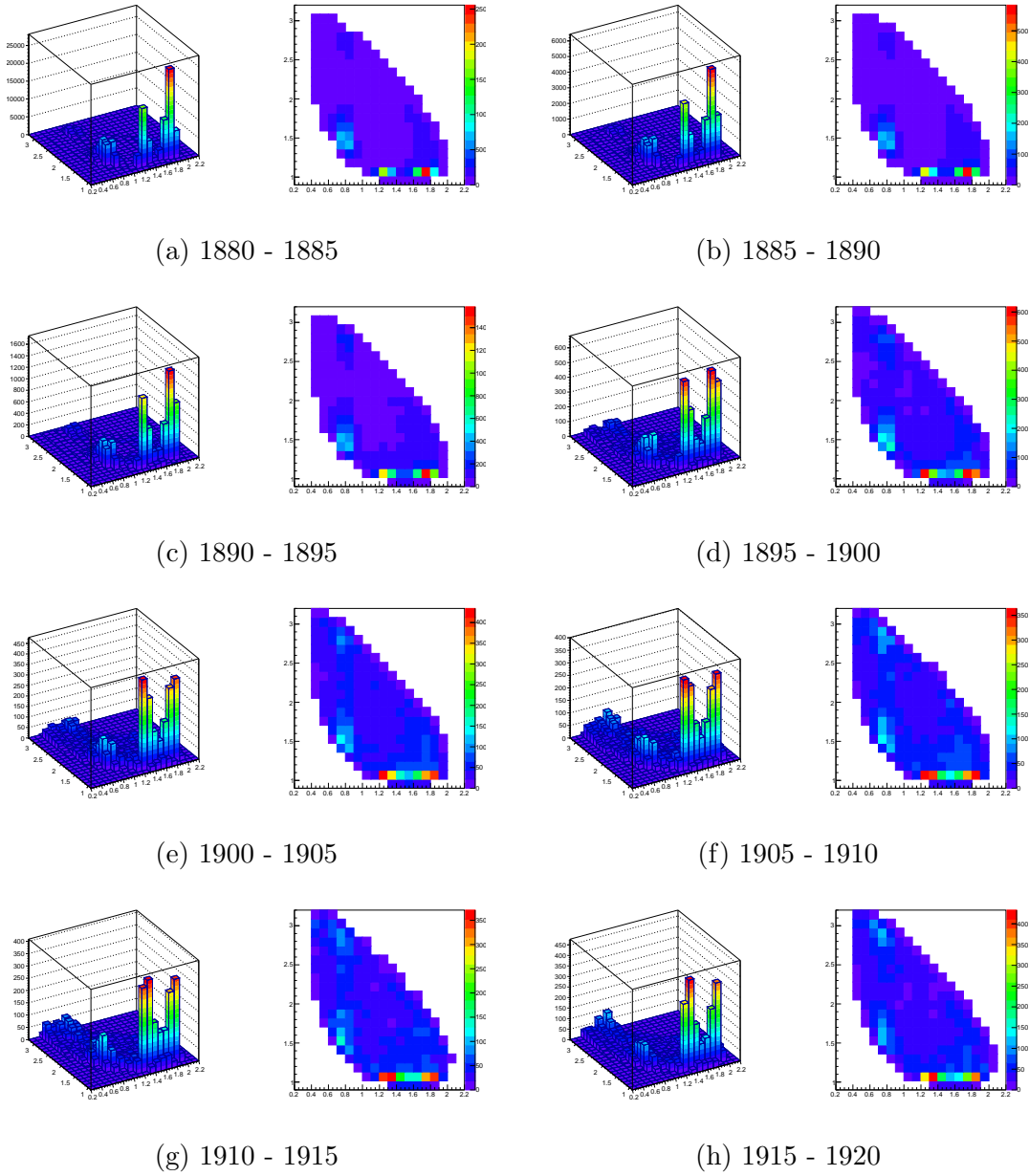


Figure C.3: Dalitz distribution in $5 \text{ MeV}/c^2$ windows. Units in each plot subcaption is also in MeV/c^2 .

Appendix D

Rio+ - Usage

Rio+ was developed aiming for easy usage and manipulation. Even though the three components of the package (ToyMCGenerator, Log Likelihood Fitter and Chi2 Fitter) are independent, they basically contain the same elements. Their use is interfaced by a “.txt” file which is given as input. Rio+ uses ROOT libraries, so it is necessary to have ROOT installed in your computer. This appendix presents the basics for using the Rio+ package.

D.1 ToyMCGenerator

The ToyMCGenerator folder contains the “.C” and “.h” files necessary for simulating $D \rightarrow 3h$ samples with a Dalitz plot distribution according to a given model. The compilation of the package is made through a makefile. Through the input .txt file the user can provide the information for the generation. Each information is given in one line, containing a string to identify what is being passed followed by the corresponding value, string, etc. Comments can be written in the “.txt” file using “#”.

The input .txt file for the generation receives options through the following strings:

- “output_file_name” - Name of the output .root file which contains the generated ntuple. The name must not include “.root” in its name since it will be added later by the package.
- “final_state” - Final state of the decay. Currently the package works with the options 0 for $KK\pi$, 1 for $K\pi\pi$, 2 for $\pi\pi\pi$ and 3 for KKK .
- “number_of_events” - Number of events to be generated for each ntuple.
- “number_of_samples” - Number of samples to be generated.
- “seed” - Seed to be fed into the random number generator. If the given seed is 0, a the random number generator will receive a random seed.
- “is_gaussian” - Defines if the D meson mass will be a Dirac delta function ($is_gaussian = 0$) or if it will have a Gaussian distribution ($is_gaussian = 1$). If a different distribution is necessary, simple modifications in the Generic_Functions.h file are required.
- “Mass_min” - Minimum of the D meson mass spectrum.
- “Mass_max” - Maximum of the D meson mass spectrum.
- “Bkg_par1” - First parameter of the background distribution, for the case of non-delta D meson mass. Currently the background is described by a linear distribution, but different functions can be implemented through simple modifications in the Generic_Functions.h file.
- “Bkg_par2” - Second parameter of the background distribution.
- “real_and_imaginary” - Defines if resonant empirical coefficients will be given as amplitudes and phases ($real_and_imaginary = 0$) or real and imaginary parts ($real_and_imaginary = 1$).

- “resonancename_re” - Real part of the corresponding resonant coefficient. Strings for the names of the resonances can be seen inside the Constants.h file.
- “resonancename_im” - Imaginary part of the corresponding resonant coefficient.
- “resonancename_amp” - Amplitude of the corresponding resonant coefficient.
- “resonancename_phs” - Phase of the corresponding resonant coefficient.
- “bkgcomponentname_fraction” - Fraction of the corresponding background component. Strings for the names of the background components can be seen inside the Constants.h file.
- “UseBackHisto” - Defines if a histogram will be used as a background component.
- “Back_Ntuple_Name” - Name of the “.root” file containing the background histogram
- “Back_Histo_Name” - Name of the background histogram
- “bkg_fraction” - Fraction of background in the generated sample ($B/(S + B)$ ratio).
- “number_of_pwa_bins” - Number of points to be used in the interpolation for the MIPWA analysis
- “pwa_txt_file” - “.txt” file containing the complex amplitude values at each point. The first column of the file is the point in the mass axis, the second is the magnitude or real part of the amplitude, the third is the phase or imaginary part and the last is not used for the generation.
- “UseAcceptance” - Defines if an efficiency histogram will be incorporated in the PDF.

- “Acceptance_Ntuple_Name” - Name of the “.root” file containing the efficiency histogram.
- “Acceptance_Histo_Name” - Name of the efficiency histogram.

An example of an input “.txt” file can be found inside the ToyMCGenerator folder. All options can be omitted and for, each one, a default value will be set. Default values can be seen in “Read_Parameters.h” file.

After writing the input file with all required information, the user can start the generation with the command: “make clean && make && ./ToyMCGenerator Input_Parameters.txt”

which erases the previous compilation, compiles again and runs the package with the information provided inside the “.txt” file.

D.2 Log_Likelihood_Fitter

The Log_Likelihood_Fitter is used with a method similar to the ToyMCGenerator. Several options in the input “.txt” file are identical. Additional information is required to set resonant coefficients as free parameters and to define their range of fluctuation. The fitter reads ROOT ntuples with branches containing the mass of the mother (with default name “M”) and the invariant masses (with default name “s12”, “s23”, “s13”, “s_low” and “s_high”). The names of the branches of the mother mass and the invariant masses of the pairs can be modified in the Log_Likelihood_Fitter.h file.

The input “.txt” file may contain the following information:

- “input_file_name” - Name of the input .root file which contains the ntuple to be fitted. The full name must be given if only one ntuple is going to be fitted. If more than one ntuple is being fitted, the package completes the name of the file with “i.root”, where *i* stands for the ntuple number. since it will be added later by the package.

- “final_state” - Final state of the decay. Currently the package works with the options 0 for $KK\pi$, 1 for $K\pi\pi$, 2 for $\pi\pi\pi$ and 3 for KKK .
- “number_of_samples” - Number of samples to be fitted.
- “is_gaussian” - Defines if the D meson mass will be a Dirac delta function ($is_gaussian = 0$) or if it will have a Gaussian distribution ($is_gaussian = 1$). If a different distribution is necessary, simple modifications in the Generic_Functions.h file are required. In the fitter, the mass limits are obtained from the ntuple directly.
- “Bkg_par1” - First parameter of the background distribution, for the case of non-delta D meson mass. Currently the background is described by a linear distribution, but different functions can be implemented through simple modifications in the Generic_Functions.h file.
- “Bkg_par2” - Second parameter of the background distribution.
- “real_and_imaginary” - Defines if resonant empirical coefficients will be given as amplitudes and phases ($real_and_imaginary = 0$) or real and imaginary parts ($real_and_imaginary = 1$).
- “resonancename_re” - Real part of the corresponding resonant coefficient. Strings for the names of the resonances can be seen inside the Constants.h file.
- “resonancename_re_upper_limit” - Upper limit of the real part of the corresponding resonant coefficient.
- “resonancename_re_lower_limit” - Lower limit of the real part of the corresponding resonant coefficient.
- “resonancename_re_fix” - If the given value is 1, the real part of the corresponding resonant coefficient is fixed. If its value is 0, the real part of the corresponding resonant coefficient is set as a free parameter.

- “resonancename_im” - Imaginary part of the corresponding resonant coefficient.
- “resonancename_im_upper_limit” - Upper limit of the imaginary part of the corresponding resonant coefficient.
- “resonancename_im_lower_limit” - Lower limit of the imaginary part of the corresponding resonant coefficient.
- “resonancename_im_fix” - If the given value is 1, the imaginary part of the corresponding resonant coefficient is fixed. If its value is 0, the imaginary part of the corresponding resonant coefficient is set as a free parameter.
- “resonancename_amp” - Magnitude of the corresponding resonant complex coefficient.
- “resonancename_amp_upper_limit” - Upper limit of the magnitude of the corresponding resonant complex coefficient.
- “resonancename_amp_lower_limit” - Lower limit of the magnitude of the corresponding resonant complex coefficient.
- “resonancename_amp_fix” - If the given value is 1, the magnitude of the corresponding resonant complex coefficient is fixed. If its value is 0, the magnitude of the corresponding resonant coefficient is set as a free parameter.
- “resonancename_phs” - Phase of the corresponding resonant complex coefficient.
- “resonancename_phs_upper_limit” - Upper limit of the phase of the corresponding resonant complex coefficient.
- “resonancename_phs_lower_limit” - Lower limit of the phase of the corresponding resonant complex coefficient.

- “resonancename_phs_fix” - If the given value is 1, the phase of the corresponding resonant complex coefficient is fixed. If its value is 0, the phase of the corresponding resonant coefficient is set as a free parameter.
- “resonancename_extra_par_ i ” - Extra resonant parameter, useful for amplitudes with more than just complex coefficients, mass and width, such as the Flatte, which contains two coupling parameters. i stands for the number of the extra parameter, which can go from 1 to 4.
- “resonancename_extra_par_ i _upper_limit” - Upper limit of extra parameter i .
- “resonancename_extra_par_ i _lower_limit” - Lower limit of extra parameter i .
- “resonancename_extra_par_ i _fix” - If the given value is 1, the extra parameter i is fixed. If its value is 0, the extra parameter i is set as a free parameter.
- “bkgcomponentname_fraction” - Fraction of the corresponding background component. Strings for the names of the background components can be seen inside the Constants.h file.
- “bkgcomponentname_fraction_fix” - If the given value is 1, the fraction of the corresponding background component is fixed. If its value is 0, the fraction of the corresponding background component is set as a free parameter.
- “UseBackHisto” - Defines if a histogram will be used as a background component.
- “Back_Ntuple_Name” - Name of the “.root” file containing the background histogram
- “Back_Histo_Name” - Name of the background histogram
- “bkg_fraction” - Fraction of background in the sample to be fitted ($B/(S + B)$ ratio).

- “number_of_pwa_bins” - Number of points to be used in the interpolation for the MIPWA analysis
- “pwa_txt_file” - “.txt” file containing the complex amplitude values at each point. The first column of the file is the point in the mass axis, the second is the magnitude or real part of the amplitude, the third is the phase or imaginary part and the last defines if the corresponding parameter is fixed or not.
- “UseAcceptance” - Defines if an efficiency histogram will be incorporated in the PDF.
- “Acceptance_Ntuple_Name” - Name of the “.root” file containing the efficiency histogram.
- “Acceptance_Histo_Name” - Name of the efficiency histogram.

An example input “.txt” file can be found inside the Log_Likelihood_Fitter folder.

The compilation and execution of the fit is practically identical to the ntuple generation:

```
“make clean && make && ./Log_Likelihood_Fitter Input_Parameters.txt”
```

D.3 Chi2_Fitter

The Chi2_Fitter usage is basically the same of the Log_Likelihood_Fitter. Additional information is required in the input “.txt” file regarding the binning choice.

The fitter reads the following options from the input “.txt” file:

- “input_file_name” - Name of the input .root file which contains the ntuple to be fitted. The full name must be given if only one ntuple is going to be fitted. If more than one ntuple is being fitted, the package completes the name of the file with “*i*.root”, where *i* stands for the ntuple number. since it will be added later by the package.

- “final_state” - Final state of the decay. Currently the package works with the options 0 for $KK\pi$, 1 for $K\pi\pi$, 2 for $\pi\pi\pi$ and 3 for KKK .
- “number_of_samples” - Number of samples to be fitted.
- “adaptive” - If its value is 1 an adaptive binning will be adopted with bin limits given by a “.txt” file. The “.txt” default file name is “bins#kkpi.txt”, where # stands for the number of bins. If the given value is 0, an uniformly binned histogram will be generated for the fit.
- “number_of_bins” - Number of bins to be used in the fit for the adaptive case.
- “number_of_s12_Bins” - Number of bins along the s12 axis in the case of uniform binning.
- “number_of_s13_Bins” - Number of bins along the s13 axis in the case of uniform binning.
- “s12_lower_limit” - Lower limit of the s12 axis in the case of uniform binning.
- “s12_upper_limit” - Upper limit of the s12 axis in the case of uniform binning.
- “s13_lower_limit” - Lower limit of the s13 axis in the case of uniform binning.
- “s13_upper_limit” - Upper limit of the s13 axis in the case of uniform binning.
- “is_gaussian” - Defines if the D meson mass will be a Dirac delta function ($is_gaussian = 0$) or if it will have a Gaussian distribution ($is_gaussian = 1$).
If a different distribution is necessary, simple modifications in the Generic_Functions.h file are required. In the fitter, the mass limits are obtained from the ntuple directly.
- “Bkg_par1” - First parameter of the background distribution, for the case of non-delta D meson mass. Currently the background is described by a lin-

ear distribution, but different functions can be implemented through simple modifications in the `Generic_Functions.h` file.

- “Bkg_par2” - Second parameter of the background distribution.
- “real_and_imaginary” - Defines if resonant empirical coefficients will be given as amplitudes and phases (*real_and_imaginary* = 0) or real and imaginary parts (*real_and_imaginary* = 1).
- “resonancename_re” - Real part of the corresponding resonant coefficient. Strings for the names of the resonances can be seen inside the `Constants.h` file.
- “resonancename_re_upper_limit” - Upper limit of the real part of the corresponding resonant coefficient.
- “resonancename_re_lower_limit” - Lower limit of the real part of the corresponding resonant coefficient.
- “resonancename_re_fix” - If the given value is 1, the real part of the corresponding resonant coefficient is fixed. If its value is 0, the real part of the corresponding resonant coefficient is set as a free parameter.
- “resonancename_im” - Imaginary part of the corresponding resonant coefficient.
- “resonancename_im_upper_limit” - Upper limit of the imaginary part of the corresponding resonant coefficient.
- “resonancename_im_lower_limit” - Lower limit of the imaginary part of the corresponding resonant coefficient.
- “resonancename_im_fix” - If the given value is 1, the imaginary part of the corresponding resonant coefficient is fixed. If its value is 0, the imaginary part of the corresponding resonant coefficient is set as a free parameter.

- “resonancename_amp” - Magnitude of the corresponding resonant complex coefficient.
- “resonancename_amp_upper_limit” - Upper limit of the magnitude of the corresponding resonant complex coefficient.
- “resonancename_amp_lower_limit” - Lower limit of the magnitude of the corresponding resonant complex coefficient.
- “resonancename_amp_fix” - If the given value is 1, the magnitude of the corresponding resonant complex coefficient is fixed. If its value is 0, the magnitude of the corresponding resonant coefficient is set as a free parameter.
- “resonancename_phs” - Phase of the corresponding resonant complex coefficient.
- “resonancename_phs_upper_limit” - Upper limit of the phase of the corresponding resonant complex coefficient.
- “resonancename_phs_lower_limit” - Lower limit of the phase of the corresponding resonant complex coefficient.
- “resonancename_phs_fix” - If the given value is 1, the phase of the corresponding resonant complex coefficient is fixed. If its value is 0, the phase of the corresponding resonant coefficient is set as a free parameter.
- “resonancename_extra_par_*i*” - Extra resonant parameter, useful for amplitudes with more than just complex coefficients, mass and width, such as the Flatte, which contains two coupling parameters. *i* stands for the number of the extra parameter, which can go from 1 to 4.
- “resonancename_extra_par_*i*_upper_limit” - Upper limit of extra parameter *i*.
- “resonancename_extra_par_*i*_lower_limit” - Lower limit of extra parameter *i*.

- “resonancename_extra_par_i_fix” - If the given value is 1, the extra parameter i is fixed. If its value is 0, the extra parameter i is set as a free parameter.
- “bkgcomponentname_fraction” - Fraction of the corresponding background component. Strings for the names of the background components can be seen inside the Constants.h file.
- “bkgcomponentname_fraction_fix” - If the given value is 1, the fraction of the corresponding background component is fixed. If its value is 0, the fraction of the corresponding background component is set as a free parameter.
- “UseBackHisto” - Defines if a histogram will be used as a background component.
- “Back_Ntuple_Name” - Name of the “.root” file containing the background histogram
- “Back_Histo_Name” - Name of the background histogram
- “bkg_fraction” - Fraction of background in the sample to be fitted ($B/(S + B)$ ratio).
- “number_of_pwa_bins” - Number of points to be used in the interpolation for the MIPWA analysis
- “pwa_txt_file” - “.txt” file containing the complex amplitude values at each point. The first column of the file is the point in the mass axis, the second is the magnitude or real part of the amplitude, the third is the phase or imaginary part and the last defines if the corresponding parameter is fixed or not.
- “UseAcceptance” - Defines if an efficiency histogram will be incorporated in the PDF.
- “Acceptance_Ntuple_Name” - Name of the “.root” file containing the efficiency histogram.

- “Acceptance_Histo_Name” - Name of the efficiency histogram.

An example input “.txt” file can be found inside the Chi2_Fitter folder.

Again, the compilation and execution of the fitter is basically the same as for the previous packages:

```
“make clean && make && ./Chi2_Fitter Input_Parameters.txt”
```

Appendix E

Ressonant Distribution Summary

This appendix contain Dalitz plots of samples generated with a single resonant channel, in order to check and understand the effect introduced to each one. All samples were generated with the Rio+ package.

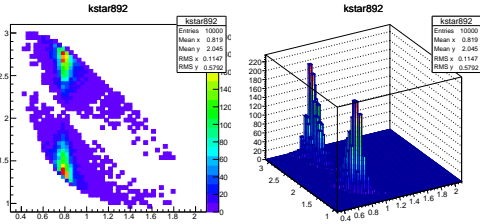


Figure E.1: $K^*(892)$ resonant contribution to the $D^+ \rightarrow K^- K^+ \pi^+$ decay on 2D (left) and 3D (right) plots.

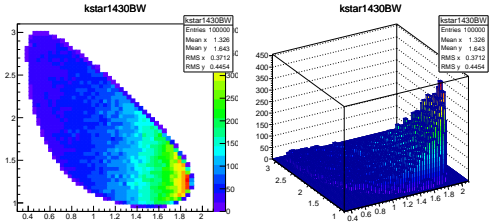


Figure E.2: $K^*(1430)$ resonant contribution, with Breit-Wigner formulation, to the $D^+ \rightarrow K^- K^+ \pi^+$ decay on 2D (left) and 3D (right) plots.

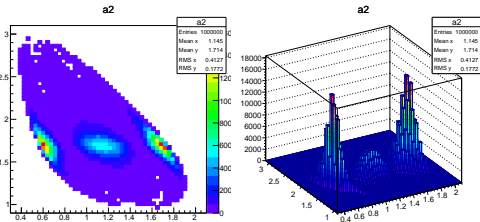


Figure E.3: $a_2(1320)$ resonant contribution to the $D^+ \rightarrow K^- K^+ \pi^+$ decay on 2D (left) and 3D (right) plots.

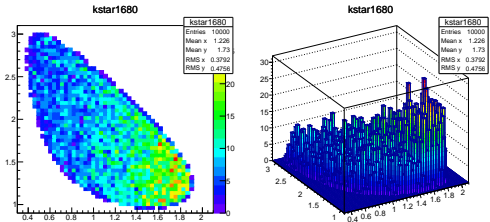


Figure E.4: $K^*(1680)$ resonant contribution to the $D^+ \rightarrow K^- K^+ \pi^+$ decay on 2D (left) and 3D (right) plots.

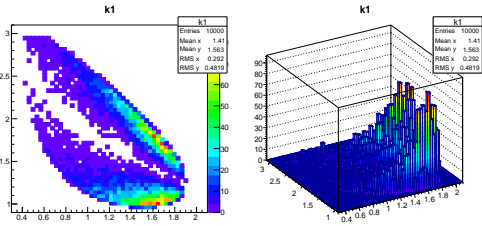


Figure E.5: $K_1^*(1410)$ resonant contribution to the $D^+ \rightarrow K^- K^+ \pi^+$ decay on 2D (left) and 3D (right) plots.

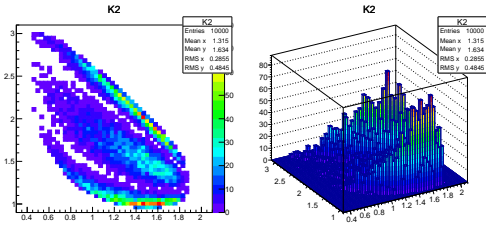


Figure E.6: $K_2^*(1430)$ resonant contribution to the $D^+ \rightarrow K^- K^+ \pi^+$ decay on 2D (left) and 3D (right) plots.

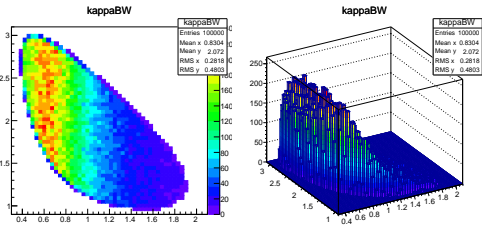


Figure E.7: κ resonant contribution, with a Breit-Wigner formulation with constant width, to the $D^+ \rightarrow K^- K^+ \pi^+$ decay on 2D (left) and 3D (right) plots.

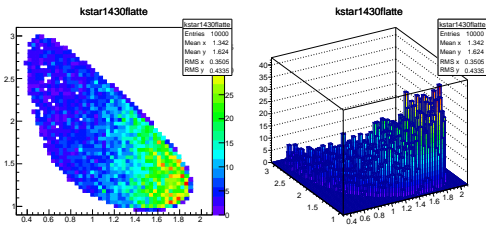


Figure E.8: $K^*(1430)$ resonant contribution, with a Flatté-like formulation, to the $D^+ \rightarrow K^- K^+ \pi^+$ decay on 2D (left) and 3D (right) plots.

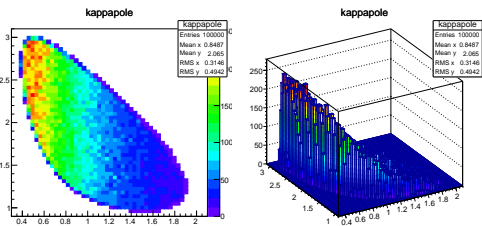


Figure E.9: κ resonant contribution, with a pole function formulation, to the $D^+ \rightarrow K^- K^+ \pi^+$ decay on 2D (left) and 3D (right) plots.

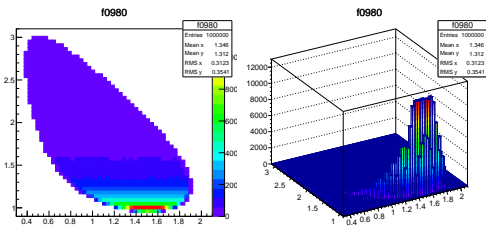


Figure E.10: $f_0(980)$ resonant contribution, with Flatté formulation, to the $D^+ \rightarrow K^- K^+ \pi^+$ decay on 2D (left) and 3D (right) plots.

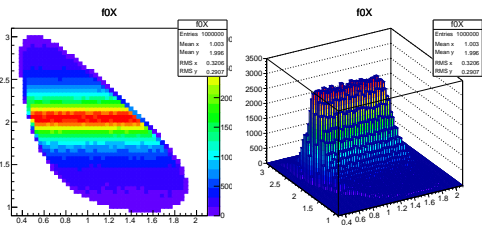


Figure E.11: $f_0(X)$ resonant contribution to the $D^+ \rightarrow K^- K^+ \pi^+$ decay on 2D (left) and 3D (right) plots.

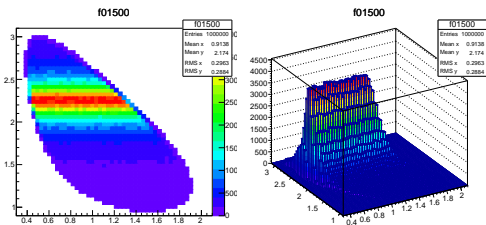


Figure E.12: $f_0(1500)$ resonant contribution to the $D^+ \rightarrow K^- K^+ \pi^+$ decay on 2D (left) and 3D (right) plots.

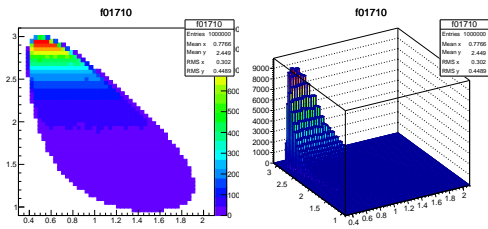


Figure E.13: $f_0(1710)$ resonant contribution to the $D^+ \rightarrow K^- K^+ \pi^+$ decay on 2D (left) and 3D (right) plots.

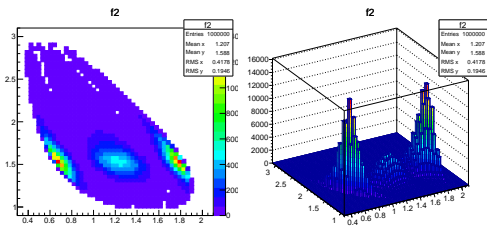


Figure E.14: $f_2(1270)$ resonant contribution to the $D^+ \rightarrow K^- K^+ \pi^+$ decay on 2D (left) and 3D (right) plots.

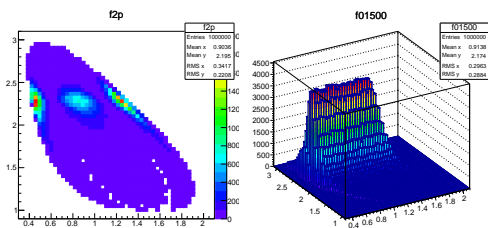


Figure E.15: $f_2'(1525)$ resonant contribution to the $D^+ \rightarrow K^- K^+ \pi^+$ decay on 2D (left) and 3D (right) plots.

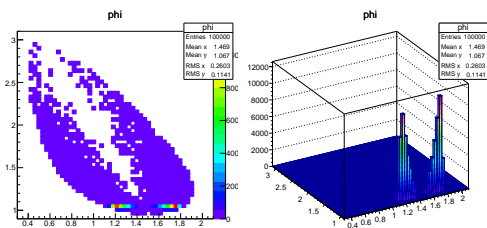


Figure E.16: $\phi(1020)$ resonant contribution to the $D^+ \rightarrow K^- K^+ \pi^+$ decay on 2D (left) and 3D (right) plots.

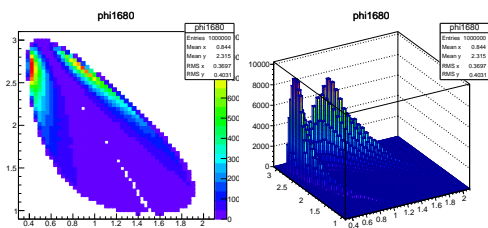


Figure E.17: $\phi(1680)$ resonant contribution to the $D^+ \rightarrow K^- K^+ \pi^+$ decay on 2D (left) and 3D (right) plots.

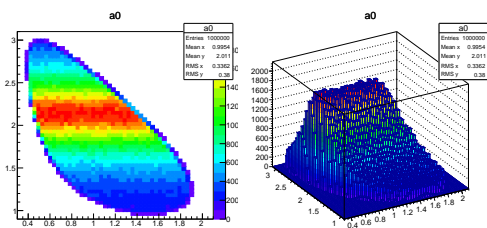


Figure E.18: $a_0(1450)$ resonant contribution to the $D^+ \rightarrow K^- K^+ \pi^+$ decay on 2D (left) and 3D (right) plots.